UNIVERSIDAD DE ANTIOQUIA
1803

Dynamical phase transitions study in a $Co_{1-x}Ru_x$ magnetic system of two-dimensional Ising type.

Juan Marcos Marín Ramírez

A thesis submitted for the degree of

Doctor in Physics

Intituto de Física
Facultad de Ciencias Exactas y Naturales
Universidad de Antioquia

Supervised by:
Dr. Oscar Arnache
Dr. Gloria E. Campillo

2020

Enquanto você se esforça pra ser

Um sujeito normal

E fazer tudo igual

Eu do meu lado aprendendo a ser louco

Um maluco total

Na loucura geral...

Raul Seixas

Abstract

The study of the magnetic properties in new materials has allowed great advances from the technological and industrial point of view. Therefore, the understanding of the physical phenomena that involve magnetism is a challenge that is still in force and that increasingly includes more research. This continuous search has been focused on the development and study of new experimental techniques, analytical and/or theoretical models that can provide the necessary tools to transcend current technological barriers and demands. Hence, the manufacture of nano-structured materials has led to the discovery of new and exciting magnetic properties and devices.

That is why, in the first part of this thesis, we will try to elaborate and develop a methodological procedure that allows the use and adaptation of advanced materials manufacturing tools, which will enable the synthesis of nano-structured magnetic thin films. This thin films have a high reproducibility and also are ferromagnetic at room temperature, a relevant aspect for a technological perspective. Likewise, these ultrathin systems can be structurally manipulated to modify the critical magnetic transition temperature or Curie T_c temperature, an intrinsic property of all ferromagnetic materials.

Furthermore, for the study of these systems it is necessary to develop an understanding of how the magnetization process occurs and its magnetization reversal (change of sign) in systems with a high anisotropy, that is, systems that have an easy axis of magnetization. These materials are currently widely used in magnetic recording processes. Combined with this last fact and the current demands for more information and speed capability of electronic devices by the final consumer, it is essential to understand the dynamic processes of magnetization under the effect of time-dependent magnetic fields. Therefore, in the second part of our work we will find some important peculiarities of the study of

magnetic transitions in low dimensional systems using external excitations with temporal dependence. For this, we will take advantage of the Kerr magneto-optical effect or MOKE, as our main study tool. This phenomenon consists of the change of polarization in an electromagnetic wave when reflected by a magnetized surface, allowing more information about some fundamental magnetic observables even at the limit of monolayers (a few atoms).

Therefore, by employing the Kerr effect in conjunction with a suitable series of test samples, we are able to study the dynamic magnetic behavior in the vicinity of the dynamic phase transition (DPT). Likewise, by changing the intrinsic Curie temperature in our thin film systems, i.e. the reduced temperature T/T_c we can access experimentally to a wider portion of the dynamic phase diagram which has not been addressed before either theoretically or experimentally for dynamic magnetic systems. For this purpose, we have fabricated $Co_{1-x}Ru_x$ $(10\bar{1}0)$ epitaxial thin films with uniaxial in-plane anisotropy by means of sputter deposition in the concentration range $0.0 \leq x \leq 0.26$. All samples are ferromagnetic at room temperature, exhibit an abrupt magnetization reversal along their easy axis, and represent a unique T_c and thus T/T_c-ratio according to their Ru concentration. The dynamic magnetic behavior was measured by using an ultra-sensitive transverse magneto-optical detection method, and the resulting dynamic states were explored as a function of the applied magnetic field amplitude H_0 and period P, as well as an additional bias field H_b, which is the conjugate field of the dynamic order parameter Q. Our experimental results demonstrate that the qualitative behavior of the dynamic phase diagram is independent from the T/T_c-ratio, and that for all T/T_c values, we observe metamagnetic anomalies in the dynamically paramagnetic state. These anomalies are characterized by a rapid rise in the order parameter in a small region of bias field, which are not present in the corresponding thermodynamic phase diagram. However, quantitatively these metamagnetic anomalies are very strongly dependent on the T/T_c-ratio, leading to an about 20-fold increase in magnitude for the metamagnetic fluctuations in the paramagnetic regime as the T/T_c-ratio increases from 0.37 to 0.68. Also, the phase space range, in which these anomalous metamagnetic fluctuations occur, extends closer and closer to the critical point as T/T_c increases.

Resumen

El estudio de las propiedades magnéticas en nuevos materiales ha permitido grandes avances desde el punto de vista tecnológico e industrial. Por ende, el entendimiento de los fenómenos físicos que involucran el magnetismo es un reto aún vigente y que cada vez abarca mayor investigación. Esta continua búsqueda, está enfocada en el desarrollo y estudio de nuevas técnicas experimentales, de modelos analíticos y/o teóricos, que provean las herramientas necesarias para trascender las barreras y demandas tecnológicas actuales. De allí, que la fabricación de materiales nano-estructurados ha dado pie al descubrimiento de nuevas y excitantes propiedades desde el punto de vista magnético.

Es por ello, que en primera instancia esta tesis tratará de elaborar y desarrollar un proceso metodológico que permita la utilización y adaptación de herramientas de fabricación de materiales avanzadas. Esto, permitirá la sintetización de películas delgadas magnéticas nano-estructuradas, con una alta reproducibilidad y además ferromagnéticas a temperatura ambiente. A su vez, estos sistemas pueden ser manipulados estructuralmente para modificar la temperatura crítica de transición magnética o temperatura de Curie T_c, propiedad intrínseca de todos los materiales ferromagnéticos.

Igualmente, para el estudio de estas películas delgadas es necesario desarrollar un entendimiento de cómo se da el proceso de magnetización y su inversión (cambio de signo) en sistemas con alta anisotropía, esto es, que presentan un eje fácil de magnetización. Estos materiales son actualmente ampliamente utilizados en procesos de grabación magnética. Combinado con este último hecho y las demandas actuales de mayor información y rapidez en la velocidad de dispositivos electrónicos por parte de sus consumidores, hace que el entender los procesos dinámicos de la magnetización bajo el efecto de campos magnéticos dependientes del tiempo, sea fundamental. Por ende, en la segunda parte de nuestro

trabajo encontraremos algunas particularidades importantes del estudio de transiciones magnéticas en sistemas de baja dimensionalidad utilizando excitaciones externas con dependencia temporal. Para ello, aprovecharemos el efecto Kerr magneto-óptico o MOKE (por sus siglas en inglés), como herramienta de estudio principal. Este fenómeno, consiste en el cambio de la polarización en una onda electromagnética al ser reflejado por una superficie magnetizada, permitiendo mayor información sobre algunos observables magnéticos fundamentales incluso en el límite de las monocapas (unos pocos átomos).

Por lo tanto, al emplear el efecto Kerr magneto-óptico junto con una serie adecuada de muestras, podemos estudiar el comportamiento magnético dinámico en las proximidades de la transición dinámicas de fase. Del mismo modo, al cambiar la temperatura intrínseca de Curie en nuestras películas delgada, es decir, la temperatura reducida T/T_c, podemos acceder experimentalmente a una porción más amplia del diagrama de fase dinámico que no se ha abordado antes ni teóricamente ni experimentalmente en el estudio de la dinámica de sistemas magnéticos. Es pro esto, que hemos fabricado una serie de películas delgadas epitaxiales de $Co_{1-x}Ru_x$ $(10\bar{1}0)$ utilizando la técnica de Sputtering en un rango de concentración de $0.0 \leq x \leq 0.26$. El dopaje con Rutenio (x) permite modificar la T_c de las películas sin alterar sustancialmente las propiedades estructurales de las películas, en especial aquellas relacionadas con la epitaxialidad del sistema. Luego, todas nuestras muestras son ferromagnéticas a temperatura ambiente y exhiben un cambio abrupto en el sentido de la magnetización (inversión en su signo) a lo largo del eje fácil de magnetización, además representan un valor único de T_c (T/T_c). Debido a estas singulares características, fue posible investigar su comportamiento dinámico usando una magnetómetro Kerr transversal ultrasensible, y los estados dinámicos resultantes se exploraron en función de la amplitud del campo magnético aplicado H_0 y el período P, así como un campo de independiente del tiempo adicional H_b, que es el campo conjugado del parámetro de orden dinámico Q.

Finalmente, nuestros resultados experimentales demuestran que el comportamiento cualitativo del diagrama de fase dinámico es independiente de la relación T/T_c, y que para todos los diferentes valores de T/T_c, observamos anomalías metamagnéticas incremento rápido en el parámetro de orden en un pequeño rango de campos) en el estado dinámicamente paramagnético, que no existen en su correspondiente termodinámico. Sin embargo, cuantitativamente estas anomalías metamagnéticas dependen en gran medida

de la relación T/T_c, lo que lleva a un aumento de aproximadamente 20 veces en los valores de las fluctuaciones metamagnéticas en el régimen paramagnético a medida que la relación T/T_c aumenta de 0.37 a 0.68. Además, el rango comprendido por el espacio de fase, en el que ocurren estas fluctuaciones metamagnéticas anómalas, se extiende cada vez más cerca del punto crítico a medida que aumenta T/T_c.

List of abbreviations

bcc	body-centenred cubic.
DC	Direct Current.
EA	Easy magnetization axis.
DPT	Dynamic phase transition.
TPT	Thermodynamic phase transition.
KIM	Kinetic Ising model.
MOKE	Magneto-optical Kerr effect.
PM	Paramagnetic phase.
FM	Ferromagnetic phase.
HA	Hard magnetization axis.
UHV	Ultra high vacuum.
hcp	Hexagonal-close packed.
HF	Hydrofluoric acid.
RT	Room temperature.
MFA	Mean Field approximation.
RF	Radiofrequency.
MO	Magneto-optical
PPMS	Physical properties measurement system.
VSM	Vibrating sample magnetometer.
T-MOKE	Transversal magneto-optical Kerr effect.
SQUID	Superconducting quantum interference device.
XRD	X-ray diffraction.
XRR	X-ray reflectivity.

Contents

Chapter 1

Introduction

Non-equilibrium phenomena and their dynamic behavior represent a topic of currently growing interest. Particularly, from the theoretical point of view, dynamic phase transitions have been observed in different fields and they have explained the complexity of dynamic responses for a wide variety of systems. Examples of such studies can be found in biological systems [1, 2], statistical processes applied to social human activity [3, 4], time-evolution of magnetic properties in promising materials such as nano-graphene [5], and quantum dynamics [6], among others. Nevertheless, today's understanding of experimental and theoretical aspects of non-equilibrium phenomena is far inferior to the understanding of its equilibrium counterpart [7].

It is important then, to define a commonly treated and interesting subject in the many-body problem, such as the *phase transition*. This event occurs when there is a singularity in the free energy or one of its derivatives, being often visible as a sharp change in the properties of a substance. The transitions from liquid to gas, from a normal conductor to a superconductor, or from paramagnet to ferromagnet are common examples [8]. Our first approach to understand this physical concept is even taught at elementary school, using the empirical knowledge of the water cycle, which has some well-defined transitions between solid (ice), liquid and gas (water vapor) depending on factors such as temperature, pressure and volume. On the other hand, for a magnetic system, we could define a critical temperature (T_c) at which an ordered phase can make a transition to a non-ordered one. Nevertheless, the dynamic aspects of phase transition (DPT) remain as an important problem, that is not close to being accounted for from the experimental and theoretical point of view.

Such a gap, have motivated theoreticians to devote a great deal of effort to devising and studying the simplest sorts of model systems which show any resemblance to those occurring in nature. For our purposes, we shall take into special account the models who are dedicated to acquire a better understanding of phase transitions and critical phenomena in magnetic systems. Although, these models tend to be quite large in number, one of the first and most successful was first formulated by Lenz and then introduced by Ising in 1925 as an attempt to explain the ferromagnetic phase transition for a one-dimensional spin chain [9, 10]. Though, the first true understanding of a phase transition in an interacting system was reached by Onsager in 1944 for the case of the two-dimensional Ising model [11, 12].

To clarify the physical basis of this phenomena, magnetic spin systems can be treated as a problem of strongly interacting particles which has a solid foundation based on the principles of statistical mechanics physics [13–16]. Even though extensive, systems in equilibrium had attracted much of the research attention throughout decades, leading to a well-defined mathematical background [9, 11, 17, 18]. The situation is quite otherwise in dealing with systems which undergo large-scale changes with time (spin dynamics). Thus, the principles of non-equilibrium statistical mechanics remain in largest measure unformulated [19, 20].

A particular realization for non-conservative single-spin-flip dynamics in magnetic systems was first introduced by Glauber in 1963 and it represents a simple way to extend the Ising model to non-equilibrium situations using the kinetic Ising model [19]. This dynamic evolution has a non-deterministic nature, which can be accurately being described by stochastic dynamics. This last one, is capable not only to depict the approach to equilibrium states but also nonequilibrium states and dynamic phase transitions of interacting lattice systems [21, 22].

Magnetic systems in the ferromagnetic phase (below T_c) when subjected to an external time-dependent oscillating field, $H(t)$, exhibit a dynamic phase transition. This fact was evidenced by Tomé and Oliveira in their seminal work on DPT [23], within a mean-field approach for the kinetic Ising model, where the system was described by a stochastic dynamics of the Glauber type and under a sinusoidal $H(t)$. Thus, deepending on the period of $H(t)$ and the relaxation time of the spin (τ), the time-dependent magnetization ($M(t)$) can either follow (paramagnetic regime) or not follow (ferromagnetic regime) the

magnetic field changes, hence resulting in a dynamically ordered phase. Also they identified a tricritical point that separates continuous or second-order phase transitions from discontinuous first-order phase transitions [24].

Given the scientific interest in dynamically ordered phases and related phase transitions, many theoretical studies have been performed, primarily based on the mean-field approach [20, 24–26] and Monte Carlo simulations [27–32]. On the other hand, an early suggestion of DPT's experimental detection was merely based on the hysteresis-loop area collapse while switching the external field amplitude, in hysteresis scaling based studies [33]. Nonetheless, the first quantitative evidence of DPT's was reached by studying $[Co/Pt]_3$ magnetic multilayers with strong perpendicular anisotropy [34]. Their corresponding cycle-averaged magnetization $\langle Q \rangle$ was determined in terms of $H(t)$, by means of the magneto-optical Kerr effect (MOKE). MOKE is a highly sensitive technique to study surface related effects, as the magneto-optical signal is proportional to the induced magnetization along the sample's surface [35, 36]. Thus in this work, experimental measurements of the magnetization time series $M(t)$ were recorded, while applying an external time-dependent magnetic field, along the surfaces normal with an additional small constant magnetic field, H_b. These experimental results were limited to a determined phase space and measured at room temperature ($T = 300$ K) and for a fixed T_c value, which means that the overall T/T_c ratio was kept constant during the measurements. Additional experimental findings at a lower T/T_c ratio, initially suggested that the similarities between DPTs and TPTs seemed to be considerable, due to the presence of transient behavior in uniaxial cobalt thin films while monitoring the dynamic order parameter Q in terms of the conjugate bias field H_b [20]. However, recent DPTs experimental results for the same Co thin films explored a wider $H_b - P$ phase space, led to the observation of anomalous fluctuations in the PM dynamic phase. This behavior occurs for rather larger H_b values in the disordered phase and can be attributed to metamagnetic tendencies, which imply a rather sharp increase in the order parameter Q in a small window of applied fields. These anomalies have a sideband-like appearance in the paramagnetic phase space in the vicinity of the dynamic critical period. In comparison, these metamagnetic fluctuations are non-existent in their thermodynamic equivalent [7, 37]. Thus, the later experimental and theoretical results give further evidence that the generalized assumption of DPTs and TPTs resemblance must be reevaluated.

Nevertheless, the underlying difficulties to produce samples with the qualities required to investigate DPTs, Ising-like systems; as well as, the exceptional experimental conditions required to carry out fast time-resolved measurements with excellent field control, are among the facts which make that the experimental base of reliable data for DPTs, has been limited so far to only a handful of studies where thermal effects have not been fully addressed. In fact, the metamagnetic tendencies were observed for a fixed T/T_c ratio, which is rather low (away from T_c). However, experimental variations of T can be very difficult, especially when precise $H(t)$ control and sensitive measurement of $M(t)$ must be ensured through the process as DPT's measurements demand [20, 34]. Under such experimental restrictions, is more accessible to modify the intrinsic Curie temperature of a magnetic system, while keeping constant the measurement conditions to detect DPTs. Additionally, experimental observations in uniaxial crystalline systems suggest that the presence of doping components can modify the intrinsic critical temperature of the system without introducing any substantial modification in their epitaxial qualities [38, 39].

Consequently, the main purpose of our project is based on the exploration of dynamic phase transitions in low dimensional magnetic system. For that, we have chosen to fabricate a series of $Co_{1-x}Ru_x$ thin films as a suitable sample set to explore and vary T/T_c and its impact onto the DPT and associated phase space behavior. In fact, an earlier work investigated the effect of Ru doping within $Co_{1-x}Ru_x$ alloy thin films onto magnetocrystalline anisotropy and T_c [39, 40], demonstrating that both hcp crystal structure and epitaxial quality of such samples can be maintained and that the in-plane uniaxial nature of its static magnetic state is unaffected [39]. Therefore, such sample series should be suitable to study the DPT and the impact of T/T_c onto the resulting dynamic behavior. For this purpose, we fabricated epitaxial single crystal $Co_{1-x}Ru_x$ $(10\bar{1}0)$ thin film samples in the Ru concentration range of $0 \leq x \leq 0.26$.

Thus, this thesis presents the research work developed during the doctoral program in Physics and its divided in six different sections. In *Chapter 1* a brief introduction towards the phase transition phenomena is discussed, whit special emphasis in dynamic phase transitions in out-of-equilibrium systems. The main motivation and aim of our research is also described.

Chapter 2 aims to expose to the reader some particular concepts about magnetism and its origins, emphasizing the properties of ferromagnetic materials, describing the interac-

tions that occur between spins and how the magnetization process takes place. Likewise, we introduce a description of the magneto-optical Kerr effect, essential to understand the experimental measurements carried out within the framework of this thesis. Towards the end of this chapter, the generalities of the dynamic phase transitions (DPT) are presented, establishing their respective phase diagram. Furthermore, the similarities and differences between this type of transitions with respect to the more well-known thermodynamic phase transitions are shown, which once again gives the main motivation towards our work.

Then, in *Chapter 3* the *Sputtering* technique is discussed as an experimental tool which enables the fabrication of high quality thin films. Then, the experimental characterization techniques (structural and magnetic) used to explore the properties of the thin films used within the context of our thesis are presented and discussed. Being these, X-ray diffraction (XRD), X-ray reflectivity (XRR), vibrating sample magnetometry (VSM), SQUID and MOKE.

Chapter 4 focuses on the methodology to fabricate the epitaxial $Co_{1-x}Ru_x$ $(10\bar{1}0)$ $(0 \leq x \leq 0.26)$ thin films. The epitaxial qualities are verified through DRX's results. Doping with ruthenium (x) does not affect the epitaxiallity of the system but in turn modifies its critical magnetic transition temperature T_c. Likewise, our thin films with different concentrations of Ru have a high magnetic anisotropy and an easy magnetization axis along the sample's surface. Being these characteristics essential to study experimentally dynamic phase transitions.

The study of dynamic phase transitions in materials with different critical temperatures is addressed in *Chapter 5*. Therefore, we first show the peculiarities of the experimental detection set-up for DPT, based on an ultrasensitive transversal Kerr magnetometer with an excellent magnetic field control. Our results show that we have experimentally accessed a larger dynamic phase space, compared to experimental results from previous works. To do this, we performed the exploration of the dynamic phase space studying the dynamic order parameter Q as a function of the period (P) and the amplitude H_0 of the time-dependent field $H(t)$. This field is composed by a time-dependent component H_0 and an independent one H_b (bias field).

So we performed the DPT scan in two different ways. To do this, we first measure the traditional $\langle Q \rangle (P, H_b)$, important to determine fine details close to the DPT point.

However, to analyze a wider dynamic space, $\langle Q \rangle (H_0, H_b)$ phase maps were determined. These maps exhibit the same major qualitative characteristics of DPT, where in a single H_{crit} a transition occurs, separating both ordered (ferromagnetic) from disordered (paramagnetic) dynamic regime. In addition, towards the end of the chapter we carefully study the metamagnetic trends [1] in the disordered regime, done by analyzing the fluctuation behavior of the order parameter $\langle \sigma \rangle_Q = \sqrt{\langle Q^2 \rangle - \langle Q \rangle^2}$. These results show that the fluctuation values increase significantly as we approach T_c. Similarly, we show that metamagnetic fluctuations close to a dynamic phase transition take place regardless of the Curie temperature.

Chapter 6 discusses the mean field theory approach to the dynamic phase transitions phenomena. Using numerical calculations, we determine the behavior of the order parameter Q and its corresponding dynamic susceptibility χ_Q, in terms of the field amplitude H_0 and the bias field H_b for different T/T_c ratios. Overall, these results were comparable to those obtained experimentally. Nevertheless, some minor differences were detected due to the implications of the model.

Finally, in the *conclusions* chapter we present a summary of the most important results found during the development of this research. Perspectives are also shown.

[1] Rapid increase of the dynamic order parameter for small changes in the external field.

Chapter 2

Fundamental concepts

In this chapter we will introduce some fundamental concepts in magnetism which are necessary to understand the main results describe in the following chapters. Thus, we will begin with a brief discussion about the origins of magnetism in matter and the corresponding magnetic ordering, i.e. exchange interaction. The magnetization reversal dynamics in ferromagnets, along the concept of anisotropy in single domain magnetic systems will be later presented. Afterwards, the physical origins of the magneto-optical Kerr effect will be described. Finally, a description of the dynamic phase transition phenomena is presented.

2.1 Origins of magnetism

Magnetism has been studied for nearly three thousand years, from ancient Greece to nowadays, its continuous research has made possible its use in extensive and important technological applications. Magnetism is an intrinsic property of matter, nevertheless, the generation of magnetic fields can be also induced by several means [41, 42]. The nature and generation of these magnetic fields can be described using the Maxwell equations, which correlate the concepts of electricity, magnetism and electromagnetic radiation [43, 44].

2.1.1 Magnetic moment

Let us define a fundamental object in magnetism called the magnetic moment (μ), useful to describe the origins of atomic magnetism in matter [42, 43, 45]. The classical representation proposed by Ampère of a magnet is equivalent to a current (I) which flow through

a closed loop of area (A), then $\mu = IA$. Thus, a general relation between the current density and the induced magnetic moment can be described by equation (2.1), where $\mathbf{j(r)}$ is the current density at a point $\mathbf{r}$ in the space [46], then:

$$\mu = \int d^3r \ \mathbf{r} \times \mathbf{j}(\mathbf{r}). \tag{2.1}$$

Furthermore, magnetic moment of a free atom has three principal sources: the spin with which electrons are endowed; their orbital angular momentum about the nucleus; and the change in the orbital moment induced by an applied magnetic field [47]. Nevertheless, the corresponding nuclear moments are three orders of magnitude smaller than those associated with electrons, because the magnetic moment of a particle scales as 1/mass, therefore we will neglect its effects [41]. Thus, we will focus only on the electronic nature of magnetism, which is related to the total angular momentum of the electron.

The source of the electron's intrinsic magnetic moment is the *spin*. Electron's spin is quantized, and it can have just two possible orientations in the presence of an external magnetic field $\mathbf{H}$, "up" (parallel) and "down" (anti-parallel) [45, 48]. Using the semi-classical atom model proposed by Bohr and considering an electron orbiting around a positive nucleus in a fixed circular orbit such as the Hydrogen atom, we can define a quantity often used to express the magnetic moment magnitude, the Bohr magneton:

$$\mu_B = \frac{e\hbar}{2m_e}. \tag{2.2}$$

where e and m_e are the electron's charge and mass, respectively, $\hbar$ is Dirac's constant. This is a natural unit of magnetic moment, just as the electronic charge e is a natural unit of electric charge. The magnitude of μ_B is equal to 9.27×10^{-27} Am [45].

Magnetic units may be a source of confusion because there are really two systems in common use. SI uses rationalized MKS (meter-kilogram-second); the others come from the CGS–emu (centimeter-gram-second–electromagnetic unit) system. Fig 2.1 presents some magnetic quantities and units used this and the following chapters. This table is useful to obtain the values of the quantities in the SI by multiplying the corresponding CGS values by the conversion factors [46]. In principle we will use the CGS system for all of our magnetic measurements. Likewise, we will refer to the magnetic moment as μ and not m as presented in Fig. 2.1.

Quantity	Symbol	CGS	SI	Conversion factor
Magnetic induction	**B**	G	T	10^{-4}
Magnetic field intensity	**H**	Oe	A m^{-1}	$10^3/4\pi$
Magnetization	**M**	erg G^{-1} cm^{-3} *or* emu cm^{-3}	A m^{-1}	10^3
Magnetic polarization	**J**	–	T	–
Magnetic moment	m	erg/G (≡ emu)	J T^{-1} (≡ A m^2)	10^{-3}
Susceptibility (volume)	χ	–	–	4π
Magnetic permeability	μ	G/Oe	H m^{-1}	$4\pi \times 10^{-7}$
Relative permeability	μ_r	–	–	1
Magnetic constant (vacuum permeability)	μ_0	G/Oe	H m^{-1}	$4\pi \times 10^{-7}$

Figure 2.1: Magnetic quantities and units [46]

2.2 Magnetization and susceptibility

Due to the electronic nature of magnetism in the atom, there is an inherent local magnetization correlated to the magnetic moment [41, 45]. Thus, in general terms the magnetization **M** can be defined as the amount of magnetic moments per volume unit (V):

$$\mathbf{M} = \frac{1}{V}\sum_{i=1}^{N}\mu_i, \tag{2.3}$$

Where μ_i are the magnetic moments. Now, if we consider a magnet that is approached to a thin foil of iron, the applied external field can induce a magnetization, in the iron piece. Thus, external fields induce changes in the magnetic moment, i.e. the system's total angular momentum. Then, we can define a relation in the change of magnetization (**M**) as a response of a change in magnetic field [49]. This quantity is called as the susceptibility (χ).

$$\chi = \frac{d\mathbf{M}}{d\mathbf{H}}. \tag{2.4}$$

According to its susceptibility, some magnetic materials present a linear response with respect to the external magnetic field, i.e. $\mathbf{M} = \chi\mathbf{H}$. Thus, for diamagnetic materials χ has a negative small value ($\chi < 0$), while paramagnetic materials (PM) exhibit a small positive value ($\chi > 0$) [50, 51]. Furthermore, these materials have no net magnetization in the absence of an external field. Ferromagnetic materials (FM) on the other hand, are not linear with **H** and exhibit a spontaneous magnetization. Therefore, they have a permanent magnetic moment in the absence of **H**. This spontaneous magnetization is a

manifestation of a long-range order, as depicted in Fig. 2.2, where the magnetic moments (red arrows) are aligned in the FM phase (grey area). This long-range order implies that the electron's corresponding magnetic moment interact with each other [45, 52]. In fact, for FM, the magnetic moments have a leading tendency to be aligned parallel so that they can add up and $M \neq 0$ (Fig. 2.2).

Nevertheless, the long-range interaction for the magnetic moments in FM regime, is only the leading term when at thermodynamic equilibrium. Once, the temperature in the system increases, it leads to an increment in the magnitude of the atomic thermal vibrations and the magnetic moments can be free to rotate, randomizing the directions of any moments that may be aligned (blue arrows in Fig. 2.2) [42, 53]. Hence, these fluctuations are responsible for the decrease in the net magnetization of the system. At a critical temperature, namely Curie temperature (T_c), the spontaneous magnetization due to the alignment of the atomic magnetic moments (ordered state) falls swiftly to zero ($M = 0$) and the system makes a transition to a disordered state (Fig. 2.2). So, the

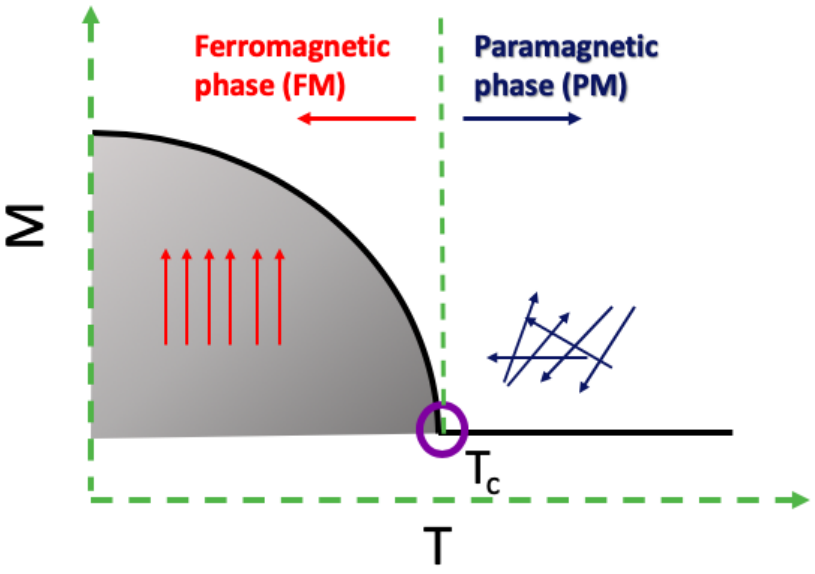

*Figure 2.2: Schematic dependence of magnetization (**M**) against temperature (**T**) for a ferromagnet in the absence of an external magnetic field. The critical temperature T_c is denoted by a violet circle. For $T < T_c$ the magnetic moments are aligned in an ordered regime of Ferromagnetic phase (red parallel arrows), leading to $M \neq 0$. For $T > T_c$ thermal fluctuations lead to a disordered regime or Paramagnetic phase (blue random arrows), thus $M = 0$.*

magnetic moments are randomly arranged, and their spin interactions are no longer the leading energy term. Thus, a thermodynamic phase transition (TPT) takes place at T_c, where the system goes from an ordered state (FM) to a disordered one (PM) [8, 54].

A relation between the material's susceptibility with temperature, was first proposed by Pierre Curie [41, 42]. He found that for diamagnetic materials[1], χ is independent of temperature, whereas for paramagnets[2], varies inversely with the absolute temperature,

$$\chi = \frac{C}{T}. \tag{2.5}$$

This relation is called the Curie law, where C is Curie's constant[3]. A generalization of this law was made by Weiss, introducing the concept of molecular field capable of aligning the neighboring spins parallel to one another in the absence of an applied magnetic field. He considered that a molecular field could be produced at the site of one spin by the interaction of the neighboring spins [55] and shown that the Curie law is only a special case of Eq. 2.6 called Curie-Weiss law.

$$\chi = \frac{C}{T - T_c}. \tag{2.6}$$

2.3 Magnetic interactions and energy

There are different types of magnetic interactions to understand how magnetic moments *feel* each other. As the main interest of this thesis is to work with materials which are in the ferromagnetic state, we will describe the magnetic interactions responsible of the magnetic order in such systems, where magnetism arises because the magnetic moments couple to one another and form magnetically ordered states.

2.3.1 Dipolar interaction

Even though is a very weak form of interaction among the magnetic moments, is the one responsible for the magnetic domain formation[4]. Furthermore, this is a long-range inter-

[1]Materials at which the induced magnetization is opposed to the applied external field

[2]Materials at which the induced magnetization changes linearly to the applied external field

[3]Intrinsic parameter to each material. In general is close to 1 K [41]

[4]Small-volume regions in which there is a mutual alignment in the same direction of all magnetic moments

action which affects the whole system and thus it contributes greatly to the magnetostatic energy [46, 49]. Consider, two adjacent moments μ_1 and μ_2 separated by a distance $\mathbf{r}$, the dipolar coupling energy has the form:

$$\mathcal{H}_{dip} = \frac{\mu_0}{4\pi \mathbf{r}^3}\left(\mu_1 \cdot \mu_2 - \frac{3}{\mathbf{r}^2}(\mu_1 \cdot \mathbf{r})(\mu_2 \cdot \mathbf{r})\right), \tag{2.7}$$

where μ_0 is the magnetic permeability in vacuum. As Eq. (2.7) shows, the pure dipolar interaction energy is a function of r and the relative orientation of the magnetic moments. Furthermore, it falls rapidly in terms of the separation of the magnetic moments. In fact, the energy provided by this interaction is only of a few Kelvins (K) [45]. Consequently, is completely insufficient to provide a quantitative explanation for the high values of T_c for relevant magnetic materials, like Fe, Ni, and Co.

2.3.2 Exchange interaction

We briefly discussed that below T_c, ferromagnetic systems are bound to be in an ordered state with their magnetic moments aligned parallel one to another. Hence, there must be a force or interaction which is responsible for the magnetic order in the system leading to the presence of spontaneous magnetization. In 1928, Heisenberg was the first to study the physical nature of this force [41]; this interaction which is called exchange interaction, has a pure quantum nature with no classical analog, and it's a direct consequence of the electron's indistinguishability [46].

To understand the origins of the exchange interaction, let us recall that the total wave function of a system, i.e. the combined spatial (ϕ) and spin wave function (χ), depends on the nature of the particle. For instance, particles with half integer spin or *Fermions* must have a total antisymmetric wave function, while particles with integer spin or *Bosons* have a total symmetric wave function. Thus, electrons are Fermions with antisymmetric wave function, then we have two possible linear combinations which satisfy these conditions:

$$\phi_A(\mathbf{r}_1, \mathbf{r}_2)\chi_S(\hat{S}_1, \hat{S}_2). \tag{2.8}$$

$$\phi_S(\mathbf{r}_1, \mathbf{r}_2)\chi_A(\hat{S}_1, \hat{S}_2). \tag{2.9}$$

The corresponding symmetric and antisymmetric spin wave function solutions are referred in literature as the triplet state and singlet state. For instance, in ferromagnets

we have that the ground state is reached when the spin function is antisymmetric, so the total wave function has the form of Eq (2.9). Therefore, If two atoms i and j have spin angular momentum $\hbar\,\mathbf{S}_{i,j} = \hat{\mathbf{S}}_{i,j}$ and, then the exchange energy between them is given by the Hamiltonian of the electronic interaction [45], which can be written as a function of the relative orientation of the spins, as:

$$\mathcal{H}_{ex} = -2\mathcal{J}\sum_{i<j}^{N} \hat{\mathbf{S}}_i \cdot \hat{\mathbf{S}}_j. \tag{2.10}$$

The last equation is known as the Heisenberg hamiltonian, where $\hat{\mathbf{S}}_i$ and $\hat{\mathbf{S}}_j$ are dimensionless spin operators and $\mathcal{J}$ is the exchange constant which has units of energy. For ferromagnets, $\mathcal{J} > 0$ and thus the spins have a tendency to be parallel.

In highly anisotropic system, i.e. where the spins have a preferential orientation (z-axis), Eq. (2.10) can be reduced to the Ising Hamiltonian, Eq. (2.11). This model is widely used to describe accurately the magnetic behavior of a large number of physical systems [10, 12, 56].

$$\mathcal{H}_{ex} = -2\mathcal{J}\sum_{i<j}^{N} \hat{S}_i^z \hat{S}_j^z. \tag{2.11}$$

In general, the exchange interaction only applies for the first neighbors, because its effects reduce significantly with distance.

2.3.3 Zeeman energy

So far, the magnetic moments can be aligned within the material by means of the dipolar interaction or by the spin exchange interaction. But, once a magnetic system is subjected to an external field, $\mathbf{H}$, the spins tend to orient in its direction to minimize the Zeeman energy [41].

$$\mathcal{H}_{Ze} = \mathbf{H}\sum_{i=i}^{N} \hat{S}_i. \tag{2.12}$$

As the Eq. (2.12) presents, this is a collective interaction and does involve all the spins in the system.

2.3.4 Magnetocrystalline energy

We have supposed that the magnetization process is isotropic, without any dependence in the direction at which the magnetic properties are measured. Nevertheless, this is not true as the crystal structure plays a fundamental role in the organization of the magnetic moments within the cell. Materials can exhibit either an easy or hard magnetization axis, this is called magnetic anisotropy. Along the easy axis, it is easier to reach the magnetization saturation[5] whereas for the hard axis is more difficult. Then, the magnetocrystalline anisotropy (MCA) is related to the orientation at which the magnetic moments tend to be aligned to minimize its energy along a preferred crystallographic axis [45, 50].

As the exchange energy is isotropic, it cannot be responsible for this anisotropic behavior. Thus, the MCA has its origins in the atom spin-orbit coupling with the *crystalline field* [6] [55]. For hexagonal systems like cobalt, the easy axis lies along the c-axis and the MCA energy is a function of the relative angle θ, between the magnetization vector and the hexagonal axis. Therefore, the Hamiltonian can be written as:

$$\mathcal{H}_K = \frac{1}{N}\sum_{i=1}^{N}\left(K_0 + K_1\sin^2\theta_i + K_2\sin^4\theta_i + \mathcal{O}\sin^6\theta_i\right). \tag{2.13}$$

Where K_0, K_1 and K_2 are the anisotropy constants and have energy units. K_0 is often neglected in anistropy calculation. When K_1 and K_2 are both positive, $\mathcal{H}_K$ is minimum for $\theta = 0$, and the c-axis is an axis of easy magnetization. A crystal with a single magnetization easy axis (EA), along which the magnetization can point either up or down, is referred to as a uniaxial crystal [42]. Then, the Eq. (2.13) can be simplified to Eq. (2.14) . This equation has minimum values, for $\theta_i = n\pi$ $(n = 0, 1, 2, \cdots)$ when $K_1 > 0$, which correspond to the EA . In contrast, for $\theta_i = m\frac{\pi}{2}$ $(m = 1, 2, 3, \cdots)$ we have the hard magnetization axis (HA).

$$\mathcal{H}_K = \frac{1}{N}\sum_{i=1}^{N} K_1\sin\theta_i. \tag{2.14}$$

The magnitude of the crystal anisotropy generally decreases with temperature more rapidly than the magnetization and vanishes at T_c.

[5] Nearly or full-alignment of the magnetic moments towards the direction of **H**

[6] Incomplete electronic sub-shells in transition metal have an orbital moment different from zero ($L \neq 0$), and therefore no spherical symmetry. Thus, when an atom from a transition metal interacts with the crystalline cell charges it produces a field, the crystalline field.

2.4 Magnetization reversal process

2.4.1 Hysteresis loop

When in the presence of **H**, a ferromagnet tends to orientate and rearrange its magnetic domains in the direction of the field. Once the alignment is maximum (almost complete in the direction of the **H**), the system reaches its maximum magnetization, called the magnetic saturation, $\mathbf{M}_s$. However, once **H** is removed, the system does not go back to its original state and retains a memory of the previous one (reminiscence). Hence, at $\mathbf{H} = 0$ the system has a remanent magnetization, $\mathbf{M}_r$. To reach a completed demagnetize material ($\mathbf{M} = 0$) it is necessary, to continuously decrease the field upon reaching the coercive field, $\mathbf{H}_c$. Depending on the values of $\mathbf{H}_c$, the material can be either soft or hard. For soft materials, the demagnetized field strength is low whereas for hard materials is rather strong [50].

By decreasing the field strength towards negative values, **M(H)** might change discontinuously to achieve a single value again. This field is called the switching field, $\mathbf{H}_{sw}$. For some FM materials, this $\mathbf{H}_{sw}$ can be equal to $\mathbf{H}_c$ or the discontinuity in the **M(H)**

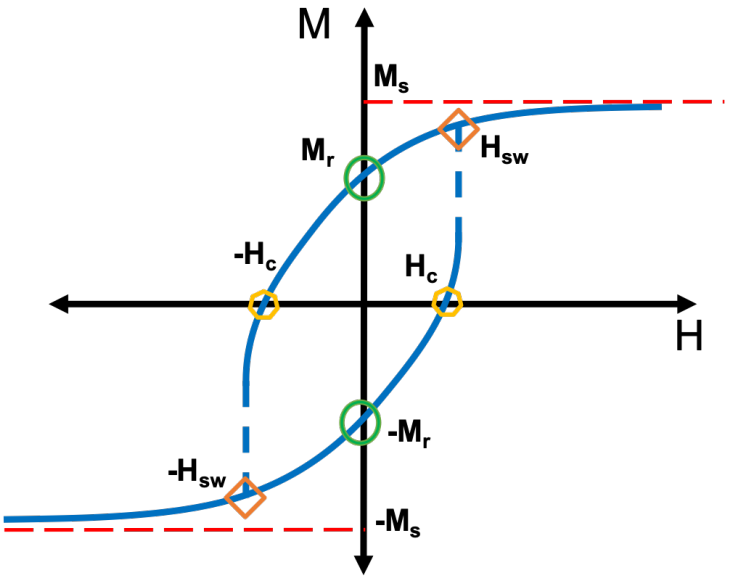

*Figure 2.3: Schematic hysteresis curve for a ferromagnet as function of **M** and **H**. The red line represents the saturation magnetization $\pm\boldsymbol{M}_s$, the green circles are the remanent magnetization $\pm\boldsymbol{M}_r$, the yellow hexagons represent the coercive field $\boldsymbol{H}_c$ and the orange squares the switching field $\boldsymbol{H}_{sw}$.*

might not happen at all. Thus, the relationship in between the behavior of M vs. H for a FM is a particular one, and the hysteretic process repeats itself by sweeping the field in between positive and negative values, as depicted by the characteristic hysteresis loop of pollycristalline systems shown in Fig. (2.3). This hysteresis loop is a manifestation of the nucleation, growth and rotation of the magnetic domains, which changes the energy landscape of the system [45, 55]. The area of the hysteresis loop characterizes the energy losses within the material; for example, the magnetic materials used in transformers cores have a reduced hysteresis loop area.

2.4.2 Stoner–Wohlfarth model

A useful model to study the magnetization reversal for single domain particles or thin films with a strong uniaxial anisotropy, is the Stoner-Wohlfarth or macrospin model [57]. This model treats the system as single domain and therefore only coherent domain rotation is allowed. Let us consider the particle in Fig. (2.4 (a)), which has a vertical *EA* and a horizontal *HA*. If we apply **H** with an angle α with respect to anisotropy *EA* and the magnetization of the particle lies at an angle of θ to *EA*, the Hamiltonian of the system

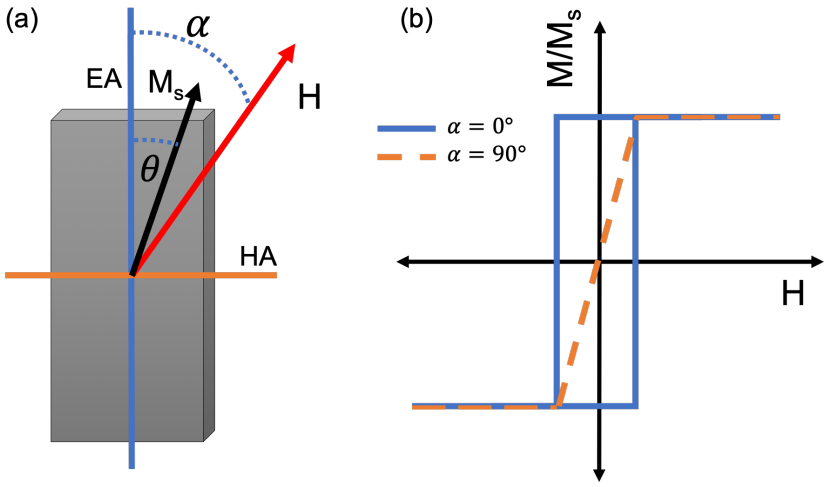

Figure 2.4: (a) Schematic of a single domain particle as described by the Stoner-Wohlfarth model (Eq. 2.16). (b) ***M(H)*** *curve for the magnetic field applied along the easy magnetization axis (blue line) with hysteretic behavior; and* ***M(H)*** *curve for the hard magnetization axis (orange dotted line).*

is equal to:

$$\mathcal{H}_{Tot} = \mathcal{H}_{ex} + \mathcal{H}_K + \mathcal{H}_{Ze} \tag{2.15}$$

$$\mathcal{H}_{Tot} = K_1 \sin^2\theta - \mathbf{HM}_s \cos(\alpha - \theta) \tag{2.16}$$

The exchange interaction term is not included in equation (2.15), as we are assuming that it does not have any angular dependence as the magnetization vector has an uniform length. Then, the minimum energy state can be obtained by finding the equilibrium position of M_s, which corresponds to $d\mathcal{H}_{Tot}/d\theta = 0$, and the corresponding component of magnetization in the field direction has the form, $\mathbf{M} = \mathbf{M}_s \cos(\alpha - \theta)$. In the absence of any external magnetic field, the magnetization lies along the EA. But, if we consider that the applied field is applied along the *HA* direction ($\alpha = 90°$), the normalized magnetization $m = M/M_s$ is linear with H, as Eq. (2.17) shows. Therefore, no hysteresis behavior is present, as the magnetization rotates from *EA* towards the *HA*. This is depicted in Fig. (2.4(b)), as the orange dotted line in the graphic and denotes a total reversible magnetization behavior. Then, the saturation for *HA* is achieved at $H = 2K_1/M_s$, which is called the Anisotropy field [41, 42].

$$m = H\frac{M_s}{2K_1} \tag{2.17}$$

Now, let us assume the case at which the magnetic positive field lies along *EA* ($\alpha = 0°$) and its aligned with the magnetization at $\theta = 0°$. As the external field decreases and changes its sign ($\theta = 180°$), for a relative high field value the magnetization then becomes unstable and it will flip towards $\alpha = 180$. Therefore, the energy landscape has two minima values which lead to a perfect hysteresis loop, as shown by the blue line in Fig. (2.4). Therefore, for $\alpha = 0$, the coercive field is equal to that of the anisotropy field.

2.5 Introduction to magneto-optical effects

In the area of light-matter interaction; magneto-optical (MO) effects refers to the change in the polarization plane of an electromagnetic wave propagating through matter, when is rotated under the influence of a magnetic field or the magnetization of the medium. This is called the Faraday effect. Furthermore, the Kerr effect is the Faraday for reflected light, due to the difference between right and left circular polarizations when the electromagnetic wave is reflected in the surface of a magnetic material [58].

Michael Faraday discovered the first magneto-optic effect in 1845, when working with polarized light which passed through a piece of glass subjected to a magnetic field. He found that, there is a change in polarization proportional to **H** as the beam was transmitted through the sample. John Kerr in 1877 observed a similar effect when examining the polarization of light reflected from a polished electromagnet pole [36], he noticed that its plane of polarization was rotated after the reflection in presence of **H**. Faraday and Kerr effects can also be interpreted as circular birefringence [7] and are described by the same physical laws [59–61]. If only first order effects are considered, both are linear with respect to the magnetization of the system and therefore we will focus only on this aspect of the MO techniques. In fact, another important MO effect such as the Voigt effect, which is quadratic with the magnetization [62] are not considered in this thesis.

2.5.1 Magneto-optical Kerr effect

The physical origin of the magneto-optical Kerr effect (MOKE) is the magnetic circular dichroism, which is characterized by the exchange and spin-orbit coupling in a magnetic material subjected to an external magnetic field [63]. Linear polarized light[8] interacting with a magnetic medium, changes its polarization, as a result there is a difference between the refraction index for left and right circularly polarized light. This birefringence is caused due to the materials magnetization interaction with the incoming electromagnetic wave. As a result, linearly polarized light is turned into elliptically polarized light with ellipticity ϵ_K and its major axis rotated by the Kerr angle Θ_K, relative to the polarization axis of the incident beam [64]. In the first order approximation, both quantities are linearly related to the spin polarization of the material or the components of its magnetization. Thus, we can analyze the polarization state of the reflected light as function of the external field, to correlate it with the magnetization within the sample.

Both first- and second-order magneto-optical effects can be quantitatively described in terms of the solutions of the Maxwell's equations in a magnetic medium, characterized by the dielectric tensor ($\tilde{\epsilon}$), which can be divided into symmetric and antisymmetric components. If we assume an optically isotropic material while making the correct denationalization of the tensor, the symmetrical part does not contribute to the MO effect

[7] birefringence of circularly polarized light

[8] Superposition of left and right circular polarized light of equal intensity.

and we only have left the antisymmetric one [45], that has the form:

$$\tilde{\epsilon'} = \epsilon \begin{pmatrix} \epsilon_{xx} & \epsilon_{xy} & \epsilon_{xz} \\ \epsilon_{yx} & \epsilon_{yy} & \epsilon_{yz} \\ \epsilon_{zx} & \epsilon_{zy} & \epsilon_{zz} \end{pmatrix} \tag{2.18}$$

Where ϵ is the conventional dielectric constant. Eq. 2.19 shows an alternative notation for the $\tilde{\epsilon}'$, using the so-called Voigt vector $Q_v = (Q_x, Q_y, Q_z)$ which is aligned with the magnetic field and has a magnitude which depends on the material and the normalized magnetization has the form $\mathbf{m} = (m_x, m_y, m_z)$ [45].

$$\tilde{\epsilon'} = \epsilon \begin{pmatrix} 1 & iQ_v m_z & -iQ_v m_y \\ -iQ_v m_z & 1 & -iQ_v m_x \\ iQ_v m_y & -iQ_v m_x & 1 \end{pmatrix} \tag{2.19}$$

Therefore, the antisymmetric tensor $\tilde{\epsilon'}$ (containing the components of the magnetization vector) connects the electrical vector $\mathbf{E}$ of an illuminating plane light wave with an induced displacement vector $\mathbf{D}$ in the regime of optical frequencies, namely

$$\mathbf{D} = \tilde{\epsilon}\,\mathbf{E}. \tag{2.20}$$

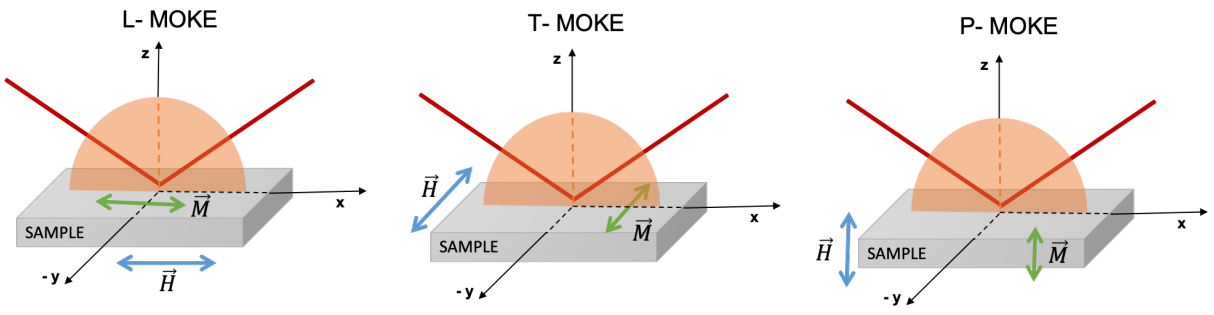

*Figure 2.5: Schematic description of the L-, T- and P-MOKE configurations. The red line represents the incoming electromagnetic wave, while the orange semicircle describes its corresponding incidence plane. Field **H** (blue line) and magnetization **M** (green line) vectors are shown in reference to the sample's surface.*

Depending upon the relative orientation of the magnetic field $\mathbf{H}$ and the plane of incidence of the probe light, MOKE is studied in three configurations: longitudinal (L-MOKE), transversal (T-MOKE), and polar (P-MOKE) as shown in Fig. 2.5 [65]. For the L-MOKE, if $\mathbf{H}$ is applied longitudinal to the incidence plane of the electromagnetic

wave (orange semicircle) with wave vector $\hat{k}$, thus $\mathbf{m} = (m_x, 0, 0)$. For the T-MOKE, $\mathbf{H}$ is perpendicular to $\hat{k}$ and to the incidence plane, so $\mathbf{m} = (0, m_y, 0)$. Finally, in P-MOKE the magnetization is perpendicular to the sample's surface but still lies inside the incidence plane, then $\mathbf{m} = (0, 0, m_z)$. Thus, the corresponding assymetrical dielectric tensor for each configuration, L-, T- and P-MOKE, can be reduced to:

$$\tilde{\epsilon'}_L = \epsilon \begin{pmatrix} 1 & 0 & 0 \\ 0 & 1 & iQ_v \\ 0 & -iQ_v & 1 \end{pmatrix}, \quad \tilde{\epsilon'}_T = \epsilon \begin{pmatrix} 1 & 0 & -iQ_v \\ 0 & 1 & 0 \\ iQ_v & 0 & 1 \end{pmatrix}, \quad \tilde{\epsilon'}_P = \epsilon \begin{pmatrix} 1 & iQ_v & 0 \\ -iQ_v & 1 & 0 \\ 0 & 0 & 1 \end{pmatrix} \tag{2.21}$$

MOKE is a very versatile technique that in its early stages, was employed broadly to study solid materials [66]. As the penetration depth of light is restricted to the order of few nanometers (for visible light), Kerr effect is an optimal technique to study surface magnetism in ultra-thin films. This was first introduced by Moog and Bader in 1985 [67]. Nowadays, MOKE allows to study the magnetic effects in the nanoscale limit [67], the magnetization dynamics in the femtosecond time scale [68, 69], magnetoplasmonics [70–73] and spintronics [68, 74, 75]. Hence, MOKE has significant importance to study the magnetism dynamics in low dimensional magnetic systems.

2.6 Dynamic phase transitions

We already discussed that for ferromagnetic systems at equilibrium, they can undergo thermodynamic phase transitions (TPTs), as seen in Fig. 2.2. At a TPT (red dot in Fig. 2.6(a)) the system's magnetization changes in an abrupt manner as a function of temperature or external magnetic field, to which the system is subjected [13, 76]. Thus, the magnetic system is characterized by an intrinsic critical temperature (T_c), at which the corresponding M changes drastically from nonzero values to zero. Therefore, T_c separates two different regimes, the ordered state or ferromagnetic (FM) phase ($T < T_c$) and the disordered or paramagnetic (PM) phase ($T > T_c$) [8, 54]. From Fig. 2.7(a) it is noticeable that in the FM, there is a field-dependent first-order phase transition as shown by the black solid line. Likewise, when under the influence of a time-dependent oscillating external field $H(t)$, certain bistable magnetic systems in their ferromagnetic phase can undergo a qualitative change in their dynamic magnetic response. Then, from

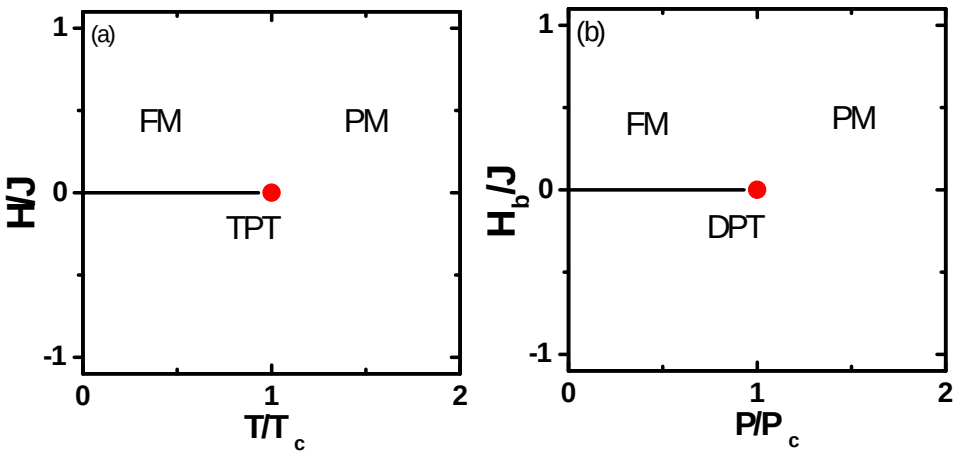

Figure 2.6: (a) TPT's and (b) DPT's phase diagrams, respectively. In both diagrams, the (red) dot represents the critical point, either T/T_c or P/P_c which separates the ferromagnetic (FM) and paramagnetic (PM) phases. The horizontal (black) line stands for a first-order phase transition within the FM phase.

Fig. 2.6(b), we can see that these variations lead to a dynamic phase transition (DPT), which is characterized by a particular critical period (P_c), which separates the ordered FM and disordered PM phases [7, 77–79].

A simplistic but powerful attempt to understand DPT's physical nature was first introduced by Tomé and De Oliveira [23]. Within a mean-field approach, they used the kinetic Ising model (KIM) [80–83] evolving with Glauber stochastic transition probabilities [19]. In this approach, the magnetic system with the corresponding time-dependent Hamiltonian, can be written in the form:

$$\mathcal{H} = -\mathcal{J}\sum_{[i,j]}^{N}\mathbf{S}_i\mathbf{S}_j - H(t)\sum_{i}^{N}\mathbf{S}_i\,. \tag{2.22}$$

The first term is related to the exchange energy with $\mathcal{J} > 0$, i.e. ferromagnetic coupling and $\mathbf{S}_{(i,j)}$ stands for the Ising spin, which can take only two possible values, ± 1. $\sum_{[i,j]}^{N}$ runs over all nearest neighbors' sites. The second term, corresponds to the Zeeman energy associated with the effect of the external magnetic field at all spins sites (i), and it is this energy term that drives dynamic changes by means of a time-dependent field H(t). $H(t)$ can be assumed to have a sinusoidal form, i.e.

$$H(t) = H_0 \sin\left(\frac{2\pi}{P}t\right) + H_b. \tag{2.23}$$

Here, H_0 is the field's amplitude, while P is the oscillation period of the external field ($P = \frac{2\pi}{\omega}$). As the period of $H(t)$ changes, so does the magnetization response in terms of the time-dependent field $M(t)$. The overall dynamic behavior can be described by using the time-averaged magnetization of the system (Q) [84–88],

$$Q = \frac{1}{P}\int_0^P M(t)dt \tag{2.24}$$

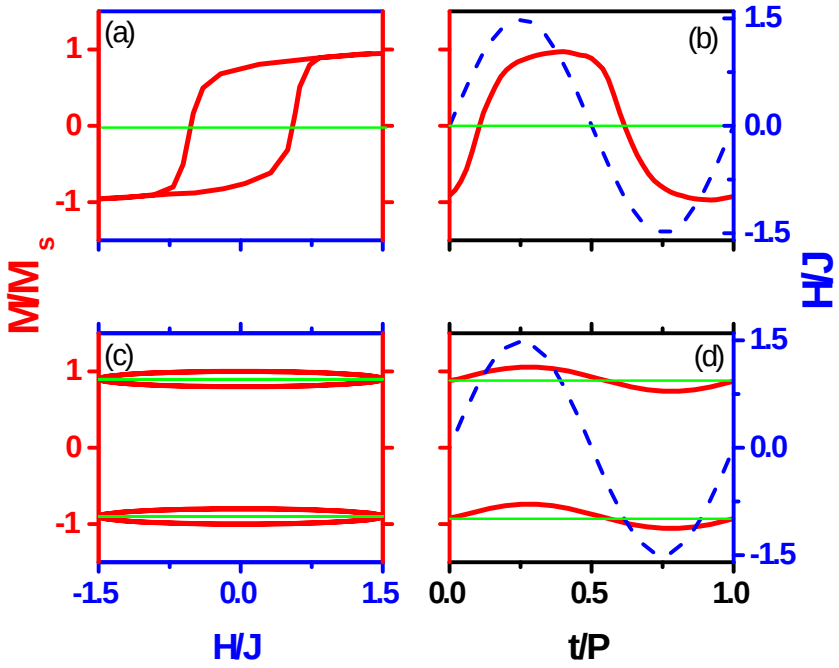

Figure 2.7: (a) and (b) Schematic illustrations of M/M_s vs. H hysteresis loops (red line) for two different field periods representing the PM phase (left) and FM phase (right). In (b) and (d) the red line represents the $M(t)$ response in comparison to the time-dependent field (blue dashed line). All solid green lines indicate the respective time-averaged magnetization value of the order parameter Q.

Thus, when P is slow enough and larger compare to the critical period P_c, $M(t)$ can be almost fully inverted (Fig. 2.7(a)), so that the net magnetization averaged over one cycle is zero, i.e. $Q = 0$ (solid green line) from Eq. (2.24). Thus, as indicated in Fig. 2.6(b) for $P > P_c$, the time-dependent magnetization (red line) within the system can follow the external excitation $H(t)$ (blue dotted line) with a slight delay. As soon as the external field period becomes smaller, the oscillating field becomes even faster and the magnetization response cannot follow the external excitation yielding to a spontaneous symmetry breaking of the hysteresis loop for $P < P_c$, which has a non-zero centered

value, as experimentally observed in Fig 2.7(c). Then, the net magnetization averaged over cycle becomes different from zero, as indicated in Fig. 2.7(d). So, this symmetry breaking introduces two possible dynamically stable states indicated by the green solid lines, for which $Q \neq 0$.

Consequently, as the time-averaged magnetization value, Q or the so-called dynamic order parameter changes from zero to a non-zero value continuously at a distinctive period $P = P_c$, a second-order dynamic phase transition (DPT) takes place [88]. While for $P < P_c$ the system is at the so-called dynamically ordered state or ferromagnetic phase (FM) with $Q \neq 0$, for $P > P_c$ there is a transition to a dynamically disordered state or paramagnetic phase (PM) where $Q = 0$ [88, 89]. The presence of a small time-independent bias field (H_b), additional to the oscillatory field is the conjugate field associated with the order parameter Q; in the same manner, as the external applied field $\mathbf{H}$ is the conjugate field for $\mathbf{M}$ in TPTs [20, 34]. DPT's phase diagram (Fig. 2.6(b)) shows that as H_b changes its sign, it induces a first-order phase transition (black horizontal line) between different dynamically ordered stable states while in the FM phase ($P < P_c$). This was experimentally observed for the first time, including the hysteretic nature of Q vs. H_b by reference [20], before any prior theoretical study. Theoretically within a Mean Field Approximation (MFA), we have that as H_b approaches zero at $P = P_c$, Q satisfies a power-law (Eq. 2.25) equivalent to their thermodynamic expression (Eq. 2.26). Here δ_D (dynamic critical exponent) is equal to the thermodynamic one, $\delta = \delta_D$[24, 26, 89].

$$Q(H_b \to 0) = H_b^{\delta_D} \tag{2.25}$$

$$M(H \to 0) = H^{\delta} \tag{2.26}$$

Further similarities between DPTs and TPTs can be drawn from the fact that theoretical results using Ising type models have shown that both phenomena exhibit the same set of critical exponents [26, 29, 90, 91]. For example, the dynamic order parameter changes from nonzero to zero continuously when P is increased towards P_c following a power-law behavior which has the form,

$$Q(P \to P_c) \propto (P_c - P)^{\beta_D} \tag{2.27}$$

where, β_D is a dynamic critical exponent. This expression recalls that for TPTs, where the magnetization (order parameter) changes as function of the temperature, by a nonzero value to zero at $T = T_c$ obeying a similar power-law,

$$M(T \to T_c) \propto (T - T_c)^{\beta} \tag{2.28}$$

Therefore, the dynamic order parameter Q mimics the behavior of M within TPTs in ferromagnets at thermal equilibrium. Hence, DPTs and TPTs were found to belong to the same universality class [77, 84, 91–93].

Nevertheless, when surfaces are introduced some contradictions arise due to the system's lattice symmetry breaking [25]. Then, the surface phase diagram of the equilibrium three-dimensional Ising model in a cubic lattice is established via mean-field approximation and Monte Carlo simulation analysis. It depends not only on the values of the coupling constants for bulk ($\mathcal{J}_b$) and surface ($\mathcal{J}_s$) or the temperature; but also on the external field [88]. Two important regimes can be perceived, according to the the ratio $r = \mathcal{J}_s/\mathcal{J}_b$. If r is sufficiently small, the system undergoes at the bulk critical temperature T_c an ordinary transition, with the bulk and surface ordering occurring at the same temperature. Beyond a special point ($r > r_{sp}$) the surface orders at the so-called surface transition at a temperature $T_s > T_c$, followed by the extraordinary transition of the bulk at T_c, hence both "systems" order at different temperatures.

More recently DPT's experimental evidence, led to the observation of anomalous fluctuations in the PM dynamic phase, for Co thin films in the $H_b - P$ phase space. This behavior occurs for larger H_b values in the disordered phase and can be attributed to *metamagnetic tendencies*, which imply a rather sharp increase in the order parameter Q in a small window of applied fields. In fact, this metamagnetic character is not present at a TPTs [37]. This significant anomalies in the vicinity of dynamic phase transitions severely limit the generally accepted broad similarities between DPT's and thermodynamic phase transitions. Hence, key characteristics associated with the DPT are qualitatively different from conventional thermodynamic phase transitions, which underlines the need for a substantial reevaluation of our understanding of dynamic phase transitions and dynamic order phenomena, in a wider temperature range. No previous theoretical and/or analytical work predicted this behavior for DPTs. As a result, the impact of T/T_c near DPT's has not been systematically explored.

The dynamic phase exploration for DPTs can be done using two different approaches, where either P or H_0 can be modified as function of H_b to obtain the corresponding dynamic phase parameter. Fig. 2.8 shows the dependence of the critical period P_c as

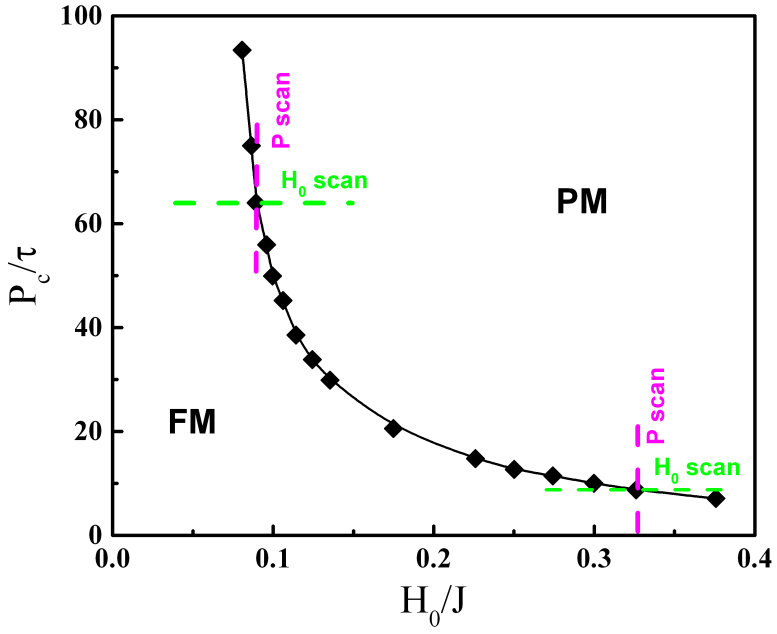

Figure 2.8: Critical period P_c as function of the applied time-dependent amplitude H_0 adapted from reference [7]. The green and magenta dashed lines represent the H_0- or P-scans that can be utilized to explore the corresponding dynamic phase space.

function of the time-dependent field amplitude, H_0. As it can be seen, there is a strong correlation between H_0 and the corresponding P_c. Thus, as H_0 increases P_c becomes smaller, thus the dynamic phase transition shifts towards lower values. Therefore, we have a fast critical dynamics regime. On the other hand, for slower critical dynamics, i.e. higher P_c values we have smaller field amplitudes H_0. Therefore, one can explore both critical regimes slow and fast using two different approaches. For instance, slower critical dynamics, a H_0-scan (cyan dashed line) allows a wider exploration of the relevant phase space near the DPT phase line, as P_c decreases rapidly as a function of H_0. On the other hand, in the traditional approach based on the faster critical dynamics, a P-scan (magenta dashed line) is a more suitable methodology, given that, in this regime, P_c is not strongly dependent on the H_0 values used to generate the dynamic magnetic state [7, 94].

DPT's experimental findings have been done by means of MOKE. This technique is a highly sensitive to study surface related effects, as the magneto-optical signal is proportional to the induced magnetization along the sample's surface [35, 36, 95–97]. Moreover, DPT's studies have been limited so far to rather low T/T_c ratios (away from T_c); therefore there is no information related to the behavior of DPT's close to a thermodynamic

phase transition or how the metamagnetic fluctuations appear in this extended regime. However, experimental variations of T can be very challenging, especially when precise $H(t)$ control and sensitive measurement of $M(t)$ must be ensured through the process as DPT's measurements request [20, 37]. Under such experimental restrictions, it is more accessible to modify the intrinsic Curie temperature of a magnetic system, while keeping constant their measurement conditions.

Chapter 3

Experimental methods

This chapter presents the different experimental techniques used during this thesis. It is divided in four sections, the first part is focused on the thin film deposition by means of sputtering technique. Then, the structural techniques are present, mainly focusing in X-ray diffraction and X-ray reflectivity. Later, the macroscopic magnetometry techniques used to determine the degree of magnetization, anisotropic properties and Curie temperature of the magnetic thin film samples is explained; using the vibrating sample magnetometry and the superconducting quantum interface device magnetometer techniques. Finally, the discussion is focused on the experimental set-up to study the magneto-optical Kerr technique, which was the main tool used in the development of this thesis.

3.1 Thin film deposition

A thin film is a low dimensional material which consist on the deposition of a few atomic layers[1] of a specific material onto a substrate via different experimental techniques. Since the later part of the 1950's, thin films have been extensively studied in relation to their potential applications in electronic and magnetic devices [98–102].

Furthermore, magnetic thin films have unique properties that are not present in bulk materials due to its reduced symmetry. These properties are sensitive to many local attributes at the surface such as electronic band structure, crystallinity, and film morphology. In particular, these properties are sensitive functions of film thickness and growth conditions [103–105]. Thus, these films are tremendously important technologically, since

[1] Systems below 100 nm are considered thin films, for higher values they behave similar to bulk systems.

most electronic devices that exploit magnetic behaviors use thin-film architectures [106]. Given the efforts towards greater and faster data storage capabilities, thin film magnetism have been an active part of research for several decades and have yield to the discovery of interesting effects [107–110]; among then, giant magnetoresistance (GMR) in magnetic multilayers allowed dramatic improvements in memory density for disk drives [109, 111, 112].

There are plenty of deposition techniques to produce high quality thin films which can relay on chemical or physical processes [105]. The physical process is composed of the physical vapor deposition (PVD) processes, and the chemical processes are composed of the chemical vapor deposition (CVD) process and the chemical solvent deposition process [98, 105]. Among PVD we can find the sputtering technique.

3.1.1 Sputtering deposition

Deposition of films by sputtering was first observed in 1852 by Grove and early used to prepared reflective coatings and other thin film samples. Later, J.S. Chapin in 1974 introduces the planar magnetron sputtering, becoming until today the most important technology for the deposition of thin films [113, 114].

In the basic sputtering process schematized in Fig. 3.1, a target (or cathode) plate is bombarded by energetic ions generated in a glow discharge plasma, situated in front of it. To generate the plasma, pressured gas is introduced into a chamber which is under ultrahigh vacuum (UHV) conditions. Usually, an inert gas such as Ar is used during the sputtering process, which also prevents any chemical reaction that might happen with the target and/or substrate. Thus, when a high voltage is applied between the cathode and anode (gun chamber wall), it ionizes the Ar atoms producing produces Ar^+ and electrons. These Ar^+ ions are attracted by the target (negatively charged) and the bombardment process causes the removal, i.e., *sputtering*, of target atoms. When the energy of the incident ions is high enough, the interaction with the surface of the material (through moment transfer), causes the atoms of the surface to be removed, and go into a vapor phase which may then condense on a substrate as a thin film [113, 115, 116]. Free electrons produced in the discharge might recombined with the Ar^+ ions and due to the law of conservation of energy, once they return their ground state they release photons in the process, which is the reason why the plasma glows (Fig. 3.1).

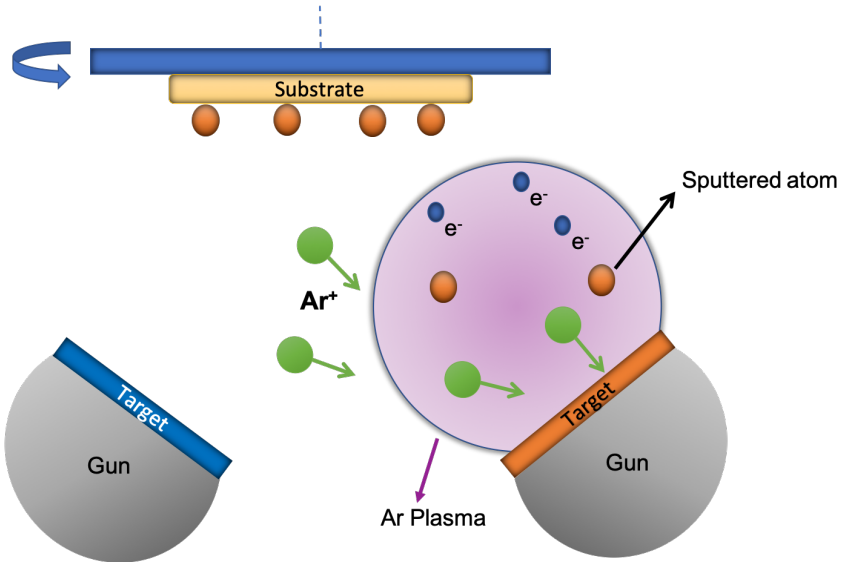

Figure 3.1: Schematic representation of the sputtering process. An electric potential between target (negatively charged) and the gun chamber wall or anode (positively charged) generates Ar^+ (green spheres) and electrons (blue spheres) ions (green dots),which can strike with the target and subsequently eject atoms (orange spheres) that can be deposited onto the substrate. Plasma produced from Ar^+ recombination and decay is shown as the light violet plume.

The sputter yield (i.e., the number of atoms sputtered per incident ion) increases almost linearly with ion energy up to about 500 eV, with typical values of sputter yield of 0.1-3 atoms/ion for ion energies up to 1.000 eV [114]. However, the process is limited by low deposition rates, low ionization efficiencies in the plasma, and high substrate heating effects. Nevertheless, such limitations can be minimized by using magnetic fields induced by an array of permanent magnets (*magnetron*), that are positioned below the target. Lorentzian forces induced by the magnetic field confines the charged particles to a region close to the target's surface, allowing an increase in the deposition rate of the film [117, 118].

DC sputtering is generally used for metallic components [119]. Nevertheless, for insulating materials, DC is not particularly suitable because it leads to the accumulation of positive charge in the target's surface, that eventually will stop the collision of ions by Coulombian repulsion. To overcome this, a radio frequency (RF) power supply is used in the sputtering process. The alternating field, allows to remove the positive charges and neutralizes the target's surface in the positive half cycle, while in the negative one the ionized atoms can sputter the target's atoms [115, 117]. Consequently, RF sputtering deposition rates are lower in comparison to the DC.

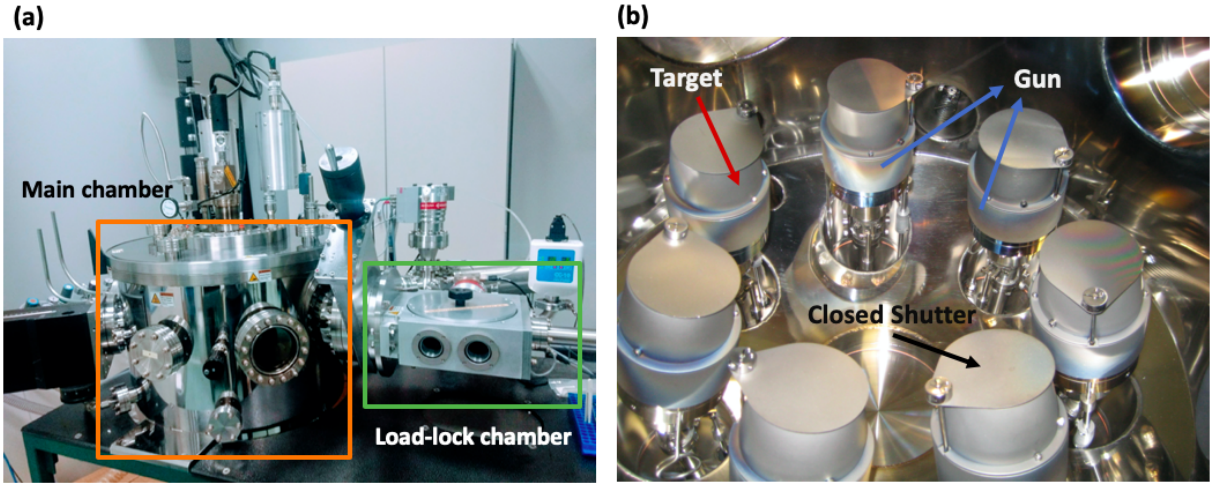

Figure 3.2: (a) ATC series UHV sputtering system from AJA Internacional, at CICnanoGUNE with the main and load-lock chamber. (b) Interior of the main chamber, where the seven sputtering guns with their respective shutters can be seen. The target is accessible when the shutter is in the open position.

In this thesis, an ATC series UHV sputtering system from AJA Internacional, Inc. Company was used for all the thin film sample deposition. Fig. 3.2 presents the sputtering system, which consist of two different chambers, load-lock and main chamber that are equipped with turbo-molecular pumps to reach preassure levels of $\sim 10^{-6}$ Pa. The load-lock chamber allows to introduce the substrate to the main chamber, without breaking the vacuum conditions by using a magnetic arm. Thus, when a new substrate is needed, only the smaller chamber is open. The main chamber has 7 different sputter guns equipped with magnetrons[2] to confine the plasma close to the target's surface.

In front of each sputtering gun a shutter in open or closed position, enables the sequential growth of 7 different multilayered films at controlled conditions, i.e. without breaking vacuum. In total, the system has 6 power supplies (2 RF and 4 to DC) , thus it allows the simultaneous deposition (co-sputtering) of up to six different materials for alloying purposes, as it was done in this thesis for the $Co_{1-x}Ru_x$ thin film samples. We have used Co, Ru, Ag, and SiO_2 targets to grow our thin films into Si(110) substrates, thus the multilayered system was grown at room temperature, pressure of 3 mTorr and using the DC sputtering guns.

Furthermore, the sputtering guns can be tilted towards the substrate position to minimize the deposition waiting time in between targets. Likewise, the substrate can rotate

[2]They can be used in balanced and unbalanced configuration.

at a precise speed, so thickness uniformity can be ensured during the deposition. In this work a rotation speed of 60 rpm was employed.

3.2 Structural characterization

3.2.1 X-Ray diffraction

Atoms can be arranged in a periodic way within the cell, thus conforming the crystalline structure. Thus, as the separation between atoms is around $\approx$ 1Å, certain light can be diffracted when passing through the crystal, where the atoms act as scattering centers for the incoming electromagnetic wave. Thus, X-ray diffraction (XRD) can be regarded as a light with matter interaction [120, 121]. In 1912, German physicist Max von Laue, developed a theory based on the idea of diffracting X-rays by means of crystals. Later in the same year, English physicists, W. H. Bragg and W. L. Bragg, were able to express a mathematical form for the von Laue experiments, to determine the condition necessary for X-Ray diffraction [122].

A schematic representation of the process is shown in Fig. 3.3(a). When monochromatic X-ray radiation with wavelength (λ) strikes a crystalline sample (composed of several planes which are spaced at a specific distance or interplanar distance ,d_{hkl}) at a certain angle (ω), diffraction can take place. Afterwards a detector is placed at angle θ to collect

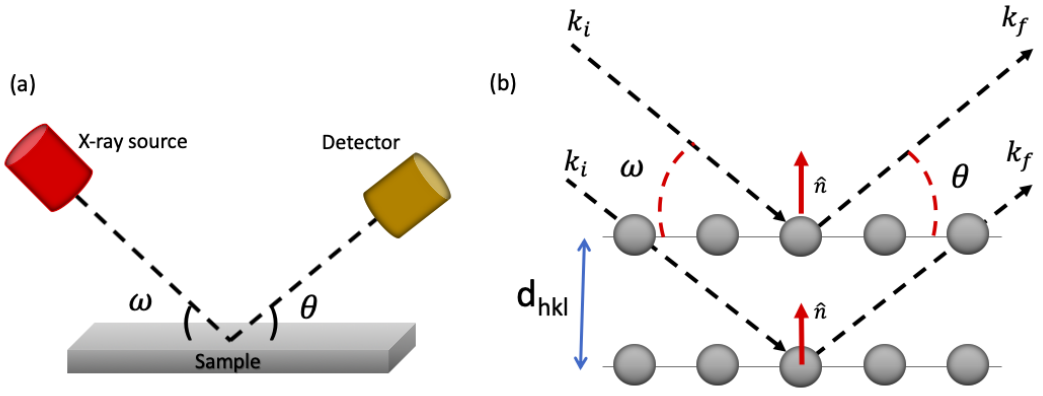

Figure 3.3: (a) Schematic representation for the X-Ray diffraction technique. A X-ray source creates X-rays that strike the sample at a angle ω and the corresponding diffracted intensity is detected at angle θ. (b) Illustration for the X-ray diffraction condition in a crystalline sample, when $\boldsymbol{k}_f$ and $\boldsymbol{k'}_f$ are in phase, there is constructive interference.

the intensity data coming from the interaction. When ω is equal to θ, the measurement is done in a $\theta - 2\theta$ configuration or Bragg-Brentano [121]. This type of measurement was the principal method used to characterize the crystalline quality of our thin film samples.

$$2d_{hkl} \sin\theta = n\lambda. \tag{3.1}$$

A blowup of the sample is schematized in Fig. 3.3(b), where the phase relation between the incoming ($\mathbf{k}_i$) and exiting wave ($\mathbf{k}_f$), which are perpendicular ($\hat{n}$) to the scattering vector $\mathbf{K} = \mathbf{k}_f - \mathbf{k}_i$ determines the condition for diffraction. Hence, destructive interference occurs in most directions of scattering, but in a few directions constructive interference takes place, and diffracted beams are formed. The angles at which constructive interference happens are directly related to the interplanar distance, therefore we have the so-called Bragg equation (Eq. 3.1).

3.2.2 X-ray reflectivity

X-ray reflectometry (XRR) is a non-destructive, highly accurate method used to determine thickness and roughness of thin layers – with thicknesses ranging from a few nanometres to some hundred nanometres – as well as the optical properties of the reflecting interfaces [123]. XRR measures the specular reflection of the incident X-ray beam, which strikes the surface of the sample at varying grazing angles [124].

Interfaces on thin films have different electronic configuration, i.e. refractive index, leading to that the incident X-ray beam can be refracted and reflected by the bottom (substrate) layer, if the incident angle (ω) is greater than the critical θ_c for total reflection at the surface[3], as schematized in Fig. 3.4(a). Then, these partially reflected waves from the top and bottom surface layers interfere and form a pattern know as the Kiessig fringes (see Fig. 3.4(b)), from which the layer thickness can be extracted from. Thus, the thickness (t) is inversely proportional to the separation (d) of two minima (maxima) periodic fringes, m and $m + 1$ (Eq. 3.2).

$$\omega^2 - \theta_c^2 = d^2 \left(\frac{\lambda}{t}\right) \tag{3.2}$$

XRD and XRR measurements for this thesis, were performed in a commercial X'Pert PRO PANalytical X-ray diffractometer equipped with a solid-state PIXcel detector. A

[3]Typical values for θ_c are below 0.5°.

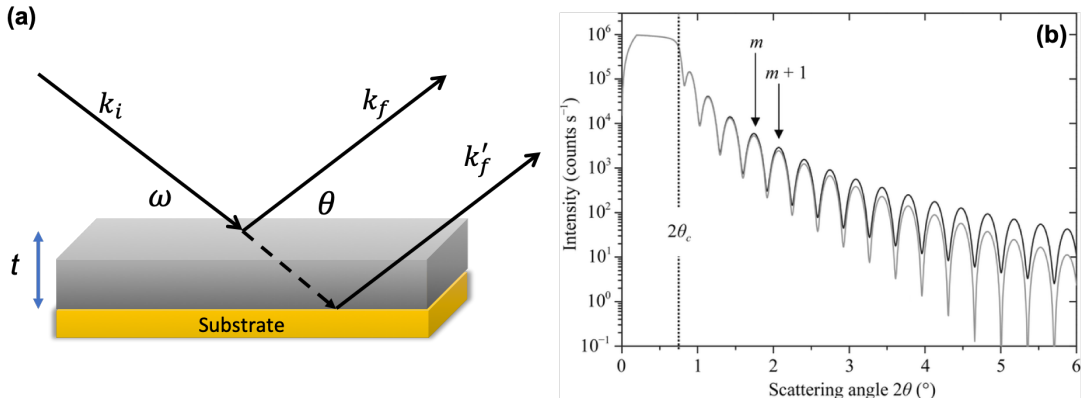

Figure 3.4: (a) Schematic XRR technique, when the incident X-ray beam (black line) hits the sample at an $\omega > \theta_c$, it can penetrate into the material (black dotted line). The interference between the outgoing radiation k_f and k'_f form the Kiessig pattern as seen on (b) (Taken from [125])

Copper's anode was used to generate the X-ray beam using K-α radiation with $\lambda = 0.154$ nm[4]. For all the XRD measurements, we used a 30° - 90° measurement range with an 0.008°/step increase factor in continuous mode.

3.3 Magnetometry based techniques

Magnetometry, in general, refers to measuring the magnetization **M** or the magnetic moment μ of a sample. Since both are vectorial quantities, magnetometry often measures only one component of the magnetization vector as the projection with the external magnetic field **H** [126].

3.3.1 Vibrating sample magnetometer

A quantification of the magnetization, i.e. the magnetic moments within a sample can be reached by different means [42, 45, 127]. One of them is by induction measurements, which involve the observation of an induced voltage by a detection coil. When an external field is applied to a magnetic system which periodically changes its position in the presence of a coil arrange, the magnetic field flux (Φ) changes and can be directly related to the magnetic moment of the sample. In effect, a vibrating sample magnetometer (commonly known as a VSM) uses this principle to measure macroscopic magnetization and it was

[4]K-β radiation was suppressed by means of a hybrid monochromator.

introduced by S. Forner in 1959 [128].

Fig. 3.5(b) illustrates the basic configuration for a VSM. A sample (blue square) placed in between an electromagnet vibrates sinusoidally in a transversal (z) or longitudinal configuration (x) in the presence of a $\mathbf{H}$. Thus, an electrical signal can be induced in a stationary pick-up coil (yellow circles) due to the changing flux induce by the movement of the magnetic moment of the sample. Therefore, based on Faraday's law of induction[5] we can determine the induced voltage in the pick-up coils by using Eq. 3.3, which depends of the number of wire turns in the coil (N), the coil turn area (A), and the angle (θ) between the magnetic field density $\mathbf{B}$ and the direction normal to the coil surface [42, 129]. Thus, the signal is proportional to the magnetic moment (sample's magnetization), as well as to the amplitude and frequency of the vibration [45].

$$V(t) = -\frac{d}{dt}\left(B\,A\cos\theta\right). \tag{3.3}$$

This simple but yet effective technique for characterizing the magnetic properties in materials is widely used in both basic research laboratories and production environments for its good performance, low price, and simplicity of operation [130–132].

A MicroMagTM Model 3900 VSM System from Pricenton Measurements Corporation (Fig. 3.5(a)), was used for in this thesis. Its high sensitivity, allows to measure signals down to 0.5 μemu at 1 s/point. This instrument, is equipped with a linear translation stage (along the three Cartesian axes) that permits the correct positioning of the sample in between the electromagnet poles. Furthermore, the VSM allows the automatic rotation of the sample in an azimuthal (see β in Fig. 3.5) direction, thus the magnetization angular dependence with the field can be also measured. This type of measurements were done in this thesis to study the anisotropic characteristics of our sputtered thin films. All of our VSM measurements were taken a RT, using a maximum applied field amplitude of ± 5 kOe.

[5] $\Phi = \int B \cdot dA$

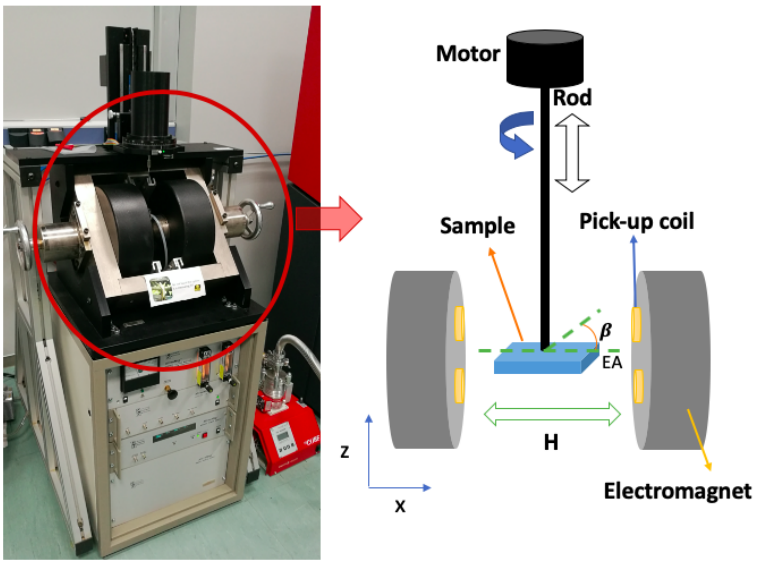

Figure 3.5: (a) Picture of the MicroMagTM Model 3900 VSM System at CIC nanoGUNE and (b)Illustration of a basic VSM, the sample (blue square) sinusoidally vibrates along z axis in the presence of an external field ***H****. The changes in the magnetic flux are detected by the pick-up coils (yellow). β is the angle between* ***H*** *and the easy magnetization axis (EA).*

3.3.2 Superconducting Quantum Interference Device Magnetometer (SQUID)

A highly sensitive way of measuring the flux change through a pick-up coil is with a superconducting quantum interference device (SQUID) [41, 45]. Thus, by combining the SQUID with the VSM technique (SQUID-VSM) we can measure magnetization with a sensitivity down to $\sim 10^{-11}$ emu. Therefore, in the SQUID-VSM configuration, we have superconducting pick-up coils and a SQUID which senses the flux changes and therefore the magnetic moment [126].

A commercial MPSM SQUID VSM EverCool from Quantum Design was used in this thesis. This equipment allows magnetic fields around 7×10^4 Oe and temperature control from 2 K to 350 K. This technique was used in our work to measure hysteresis loops down to 5 K and up to 350 K, and to determine the Curie temperature of our thin films.

3.4 Magneto-optical Kerr effect

In the section 2.5 we introduced some basic concepts to understand the physical principles of the magneto-optical Kerr effect. Now, we are going to focus our discussion around the

experimental detection scheme based on the derivation of the reflection matrix ($\overline{\overline{R}}$), which correlates the Kerr signal with the light intensity detected.

In general, magneto-optics aims to determine the dielectric tensor $\bar{\epsilon}$ in materials [133, 134]. However for thin films composed by different multilayers, it is not an straightforward procedure as each layer will have a distinctive $\bar{\epsilon}$. Furthermore, as MOKE is a reflection experiment we only have information about the reflection matrix which is related to the $\bar{\epsilon}$ of the system [135].

Using the Fresnel equations, which describe the effects of an incoming electromagnetic plane wave falling on the interface between two different dielectric media [136, 137], we can describe $\overline{\overline{R}}$ as Eq. 3.4; where s and p sub-indices indicate the directions with respect to the plane of incidence, i.e. s denotes the perpendicular component while p lies along the plane of incidence.

$$\overline{\overline{R}} = \begin{pmatrix} r_{ss} & r_{sp} \\ r_{ps} & r_{pp} \end{pmatrix}. \tag{3.4}$$

When the media is not under an external field, we have only pure optical contributions, namely r_{ss} and r_{pp}. Then, the mixed off-diagonal components appear when the sample is magnetized, i.e. r_{sp} and r_{ps}. Considering n_0 and n_1 to be the respective refraction indices of the dielectric medium, θ_0 and θ_1 the angles of incidence, and recalling the antisymmetric dielectric tensor expression from Eqs. 2.18 and 2.19; these matrix elements can be written as,

$$r_{ss} = \frac{n_0 \cos\theta_0 - n_1 \cos\theta_1}{n_0 \cos\theta_0 + n_1 \cos\theta_1} \tag{3.5}$$

$$r_{sp} = \frac{-n_0 n_1^{-1} \cos\theta_0 \left(\epsilon_{xy} \cos\theta_1 + \epsilon_{yz} \sin\theta_1\right)}{\left(n_1 \cos\theta_0 + n_0 \cos\theta_1\right)\left(n_0 \cos\theta_0 + n_1 \cos\theta_1\right)\cos\theta_1} \tag{3.6}$$

$$r_{ps} = \frac{-n_0 n_1^{-1} \cos\theta_0 \left(\epsilon_{xy} \cos\theta_1 - \epsilon_{yz} \sin\theta_1\right)}{\left(n_1 \cos\theta_0 + n_0 \cos\theta_1\right)\left(n_0 \cos\theta_0 + n_1 \cos\theta_1\right)\cos\theta_1} \tag{3.7}$$

$$r_{pp} = \frac{n_1 \cos\theta_0 - n_0 \cos\theta_1}{n_1 \cos\theta_0 + n_0 \cos\theta_1} - \frac{2 n_0 n_1^{-1} \cos\theta_0 \sin\theta_1 \epsilon_{xz}}{\left(n_1 \cos\theta_0 + n_0 \cos\theta_1\right)^2} \tag{3.8}$$

These elements are proportional to the magnetization state of the sample; thus $r_{pp} \propto m_y$, $r_{ps} \propto -(m_x + m_z)$ and $r_{sp} \propto (m_x - m_z)$; r_{ss} is a pure optical coefficient. As the polarization rotates as a function of the magnetization in the sample, we can introduce the corresponding expressions for the Kerr angle Θ_K and its ellipticity ϵ_K in terms of the

elements of $\overline{\overline{R}}$ [138], thus

$$\Theta_K = \mathbf{Re}\left(\frac{r_{sp}}{r_{pp}}\right) \tag{3.9}$$

$$\epsilon_K = \mathbf{Im}\left(\frac{r_{sp}}{r_{pp}}\right). \tag{3.10}$$

This expressions are valid for the L-MOKE configuration where $\mathbf{m} = (m_x, 0, 0)$. For the P-MOKE configuration ($\mathbf{m} = (0, 0, m_z)$), we have a similar expression with small changes. Nevertheless, T-MOKE only modifies the pure $p-$ component of the incoming light, then no mixed elements appear in $\overline{\overline{R}}$. Therefore, experimentally P-MOKE and L-MOKE are sensitive to polarization changes in light [70, 139, 140], whereas T-MOKE to its intensity [141, 142].

$$\mathbf{E}^r = \begin{pmatrix} E_s^r \\ E_p^r \end{pmatrix} = \overline{\overline{R}} \begin{pmatrix} E_s^i \\ E_p^i \end{pmatrix} = \begin{pmatrix} r_{ss} & r_{sp} \\ r_{ps} & r_{pp} \end{pmatrix} \begin{pmatrix} E_0 \cos\theta_i \\ E_0 \sin\theta_i \end{pmatrix}. \tag{3.11}$$

Using the Jones matrices formalism to describe the polarization state of an incoming electromagnetic wave $\mathbf{E}^i$ after the reflection $\mathbf{E}^r$ (Eq. 3.11), we can find a relation for the light intensity detected (I_d) after the reflection with the magnetic medium with respect to its Kerr rotation angle (Eq. 3.12).

$$\Theta_K \propto \frac{\Delta I}{I}, \tag{3.12}$$

where $\Delta I = I_d(max) - I_d(min)$, with $I_d(max) = M_{max}$ and $I_d(min) = M_{min}$ are proportional to the maximum and minimum magnetization value, respectively. I is the mean intensity:

$$I = \frac{1}{2}\left[I_d(Max) - I_d(Min)\right]. \tag{3.13}$$

3.4.1 Ultrasensitive T-MOKE

A basic L-MOKE detection set-up is schematized in Fig. 3.6(a). This set-up is widely used for L-MOKE and P-MOKE [138, 140]; being based on the effective detection in the change of polarization for the Kerr signal. Coherent light coming from a laser passes through a first polarizer **P**, so that light comes out linearly polarized. Then, the beam strikes the sample's surface (which is magnetized along x) and the reflected light that is elliptically polarized, passes for a second polarizer (analyzer) **A**. The analyzer is set to

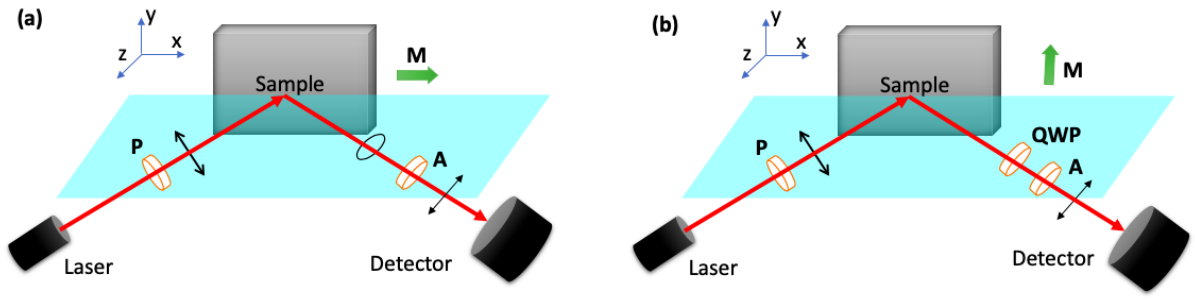

*Figure 3.6: (a) Schematic L-MOKE and (b) Ultrasensitive T-MOKE set-up. Both have a coherent light source (laser), an initial polarizer (**P**), a second polarizer (**A**) and a photodetector. For (b), an additional **QWP** was used in between the sample's reflected light and the analyzer to enhance the sensitivity of the system.*

an small angle away from extinction[6], to maximize the sensitivity for the MOKE-induced rotation. Then, a detector is placed after **A** to detect the light intensity which as we already point out is related to Θ_K.

On the other hand, from the reflection matrix we conclude that T-MOKE merely detects changes in the intensity of p-polarized component. Then, the most basic set-up will consist on p-polarized light which hits a sample magnetized along the y axis and the reflected light intensity changes are detected upon magnetization reversal. Nevertheless, in this thesis we used a different approach to T-MOKE, based on the detection of effective polarization changes. A schematic representation of this experimental tool is depicted in 3.6(b). Incident light coming from the laser passes through a fixed first polarizer (**P**) and then is reflected by the sample, which is positioned inside the gap of an electromagnet. An external field **H**, is applied transversally (y axis) with respect to the laser's incident plane (magenta plane). Then, the reflected beam goes through a rotatable quarter-wave plate retarder (**QWP**) to a second rotatable polarizer (**A**). Lastly, the transmitted light intensity is collected by a photodetector with built-in pre-amplifier. To limit the light level reaching the photodetector, coming from the purely optical reflected light, that does not carry magneto-optical signal information, **QWP** and **A** are rotated iteratively. When the minimum intensity is detected, **A** is rotated 2 degrees away from the extinction position, thus a large relative magneto-optical T-MOKE signal and a sufficient light level

[6]Denotes the angle at which no light passes through the polarizer, i.e. the intensity detected is approximately zero.

can be easily detected with the ultrasensitive set-up. This set-up enables to measure the effective polarization rather than the conventional intensity for T-MOKE measurements, which enhances the sensitivity about 20 times. Further details of this detection approach and its overall performance can be found in reference [143, 144].

To enable the experimental detection of dynamic phase transition, this ultrasensitive T-MOKE set-up was slightly adapted. Fine details of each component of the new system are discussed in Section 5.1 with the overall detection scheme used for our DPTs measurement approach.

Chapter 4

Uniaxial $Co_{1-x}Ru_x$ thin films fabrication

This chapter describes the experimental route used to fabricate the ultrathin film samples for the $Co_{1-x}Ru_x$ system, using the co-sputtering method. In the first part we will discuss the essential consideration before the deposition process, i.e. the thickness calibration measurements combined with the growth sequence to induced the desired stochiometry and epitaxiallity. Then, the co-sputtering process and growth condition are described. Later, we describe a template Ag/Cr bi-layer thicknesses study, to produce epitaxial growth and in-plane easy axis magnetization. Finally, the structural and magnetic characterization of the $Co_{1-x}Ru_x$ $(10\bar{1}0)$ thin films in the range $0 \leq x \leq 0.26$, is presented and analyzed.

4.1 Thin film deposition

Experimental works concerning dynamic phase transition, based on the theoretical and analytical studies, have determined the type of sample needed to successfully detect this phenomenon. In effect, the magnetic bistability of the sample must be enhanced, therefore a system with strong in-plane uniaxial anisotropy and reduced out-of-plane interactions with none or minimal dipolar demagnetization effects must be ensured [20, 25–29, 32, 34, 89–92, 145–148]. Furthermore, uniaxial materials with a defined in-plane easy axis (EA) allow overcoming the relevance of magnetostatic interactions, which can blur or even mask the direct impact of the crystalline orientation onto magnetization reversal [149].

Samples with these characteristics have been fabricated before, with special emphasis on Co-based thin films [20, 33, 34, 38, 149–154].

Based on this fact, we have chosen here to fabricate a series of epitaxial single crystal $Co_{1-x}Ru_x$ $(10\bar{1}0)$thin film samples in the Ru concentration range of $0 \leq x \leq 0.26$, as a suitable sample set to explore DPTs. Actually, in an earlier work the effect of Ru doping within $Co_{1-x}Ru_x$ alloy thin films onto magnetocrystalline anisotropy was investigated, concluding that both *hcp* crystal structure and epitaxial quality of such samples can be maintained and that the in-plane uniaxial nature of its static magnetic state is unaffected [39]. Furthermore, this study also demonstrated that T_c can be modified precisely and reproducibly as function of the doping concentration [39, 40]. Therefore, in this chapter, we will describe the co-sputtering deposition process which lead to the alloyed $Co_{1-x}Ru_x$ thin film samples used to study DPTs in samples with different Curie temperature.

4.1.1 Thickness calibration

The high quality of the thin film samples needed to detect experimentally DPT's, requires that thickness control must be ensured throughout the deposition process. Thus, thickness calibration measurements using XRR were done to determine the sputtering power and deposition time for the different targets (Ag, Cr, Co and Ru), required to a fabricate 20 nm $Co_{1-x}Ru_x$ co-sputtered thin films.

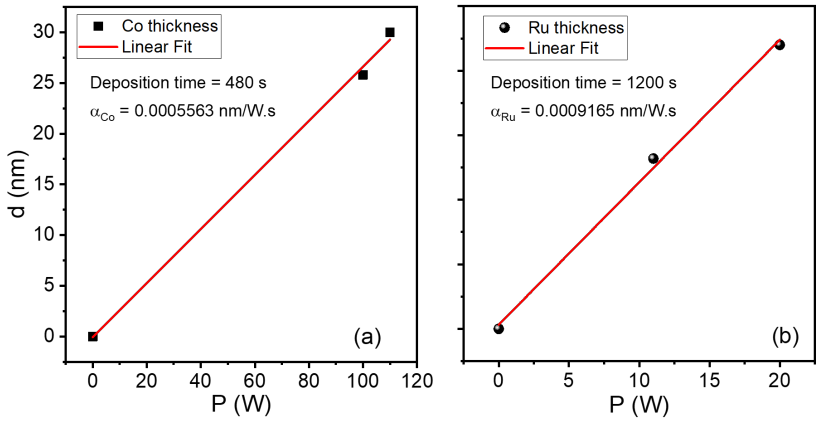

Figure 4.1: Deposition rate in terms of the sputtering power determination, using the thickness calibration results from XRR for (a) Cobalt, $\alpha_{Co} = 0.0005563$ nm/W.s and (b) Ruthenium, $\alpha_{Ru} = 0.0009165$ nm/W.s

Fig. 4.1(a) shows the measured thickness (d black squares) for the Co target using a

different sputtering power (W) and a constant deposition time of $t = 480$ s. Assuming a linear relation between the thickness and power, the corresponding deposition rate as function of the power input α_{Co} [nm/W.s], can be determined by the slope of the curve using a least-square linear fit. Then, $\alpha_{Co} = 0.0005563$ nm/W.s . Likewise, Fig. 4.1(b) presents the data for the different Ru thicknesses (black circles) using a fixed deposition time of $t = 1200$ s, leading to a $\alpha_{Ru} = 0.0009165$ nm/W.s . Similar analysis were done for Ag ($\alpha_{Ag} = 0.00406$ nm/W.s) and Cr ($\alpha_{Cr} = 0.00406$ nm/W.s) targets. Thus, we can ensure a experimental control in thickness of our multilayered system [1].

4.1.2 Growth sequence

So far we have highlighted the importance to induce experimentally an in-plane well-oriented easy magnetization to explore DPTs. Likewise, it is critical that the system exhibits a high magnetization reversal character. This can be achieved by aligning the *c*-axis of the hexagonal close packed (*hcp*) crystal structure along the sample's surface, for the $Co_{1-x}Ru_x$ thin film alloy system. Thus, in order to achieve this particular structural and magnetic behavior in our thin films, it is to deposit a template bilayer of Ag(110) and Cr(211), onto a Si (110) substrate [39, 157]. The overall growth sequence is illustrated in Fig 4.2(a). Thus, we have Si(110)/Ag(110)/Cr(211)/$Co_{1-x}Ru_x(10\bar{1}0)$/SiO_2. The SiO_2 coating is deposited onto the $Co_{1-x}Ru_x$ layer to prevent any contamination and/or oxidation in the thin film's surface. The whole multilayer system is achieved *in-situ*.

The diamond-like cubic structure of the Si in the (110) direction forms a rectangular plane as depicted in Fig. 4.2(b) which has dimensions of 0.768 nm × 0.543 nm. Ag (*fcc* crystal structure) forms a rectangular plane as well in the (110) direction as depicted in Fig. 4.2(c), with dimensions of 0.578 nm × 0.409 nm. Then, a Si(110) supercell of 3×3 can be almost perfectly fitted by a Ag(110) half supercell of 2×4, with a mismatch close to 0.4% [157, 158]. Thus, good epitaxial qualities can be reached by the Ag(110) thin layer film. Furthermore, Cr (*bcc* crystal structure) in the (211) direction forms another rectangular plane (Fig. 4.2(d)) of 0.410 nm × 0.250 nm dimensions, leading to a mismatch of 7% with respect to the Ag(110) cell. Nevertheless, this large mismatch does not affect the epitaxial qualities of the samples as the X-ray diffraction analysis showed (see section

[1] Further details on the thickness calibration analysis and the deposition rates for CoRu thin film samples can be found in references [20, 39, 155, 156]

4.1.4). Finally, Co has a hexagonal closed-packed crystal structure (*hcp*), and in the $(10\bar{1}0)$ forms a rectangle with dimensions 0.407 nm × 0.251 nm (Fig. 4.2(e)), thus it can fit with the Cr(211) cell with a rather low mismatch (0.4%). Furthermore, it can be seen that the *c*-axis for the $Co_{1-x}Ru_x(10\bar{1}0)$ lies along the sample's in-plane axis. Therefore, by employing this growth sequence, we can guarantee the desired epitaxial qualities with the intended EA magnetization axis lying along the Si(110) direction.

Before any film deposition, Si(110) substrate surface was cleaned by using first acetone followed by isopropanol. Then, it was rinsed using deonized water to remove any residual material. Subsequently, hydroflouric acid (HF) at 2%, was employed (during 10 minutes) to eliminate the natural SiO_2 formed in the substrate's surface, and then immediately the substrate was introduced to the sputtering main chamber to reduce the formation of oxides prior the deposition process.

All depositions were performed at room temperature (RT) using a pressure of 0.4 Pa pure Ar atmosphere. The sample holder was rotated during the deposition process at 60 rpm, so high homogeneity can be retrieved. All the targets (Ag, Cr, Co and Ru) were pre-sputtered for 60 s before opening the gun's shutter to ensure plasma stabilization.

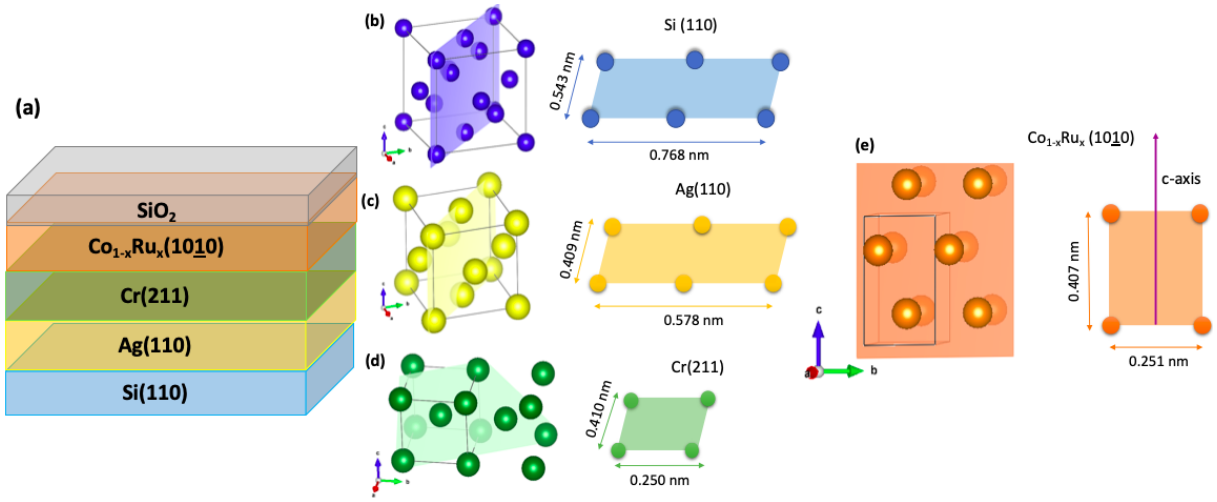

Figure 4.2: (a) Schematic illustration of the growth sequence for the $Co_{1-x}Ru_x(10\bar{1}0)$ thin film samples. (b), (c), (d) and (e) Shows the crystal structures and the crystal planes formed fro Si(110), Ag(110), Cr(211) and $Co_{1-x}Ru_x(10\bar{1}0)$, correspondingly. The lattice dimensions are in reference to the bulk parameters for each system.

4.1.3 Co-sputtering deposition

To deposit the $Co_{1-x}Ru_x$ alloyed thin films it is necessary to establish the experimental conditions to produce the co-sputtering process in the desired regime, i.e. $0 \leq x \leq 0.26$. This is done, by modifying the power potency for the Co and/or Ru target during the sputtering, which in turn adjusts the deposition rate (r). Thus, the deposition rate ratio (ζ) is proportional to the alloyed ratio, as follows:

$$A_{1-x}B_x \Rightarrow \frac{r_A}{r_B} \equiv \zeta = \left(\frac{x}{1-x}\right)\left(\frac{\rho_A}{\rho_B}\right)\left(\frac{m_A}{m_B}\right), \tag{4.1}$$

with ρ_A and ρ_B being the density at room temperature and m_A and m_B being the standard atomic mass. Let us assume a linear deposition rate (r_{target}) in terms of the power output (P_{target}) for both targets, so the deposition rate has the form,

$$r_{Ru} = \alpha_{Ru} \cdot P_{Ru}, \tag{4.2}$$

$$r_{Co} = \alpha_{Co} \cdot P_{Co}. \tag{4.3}$$

Eq. 4.1 showed that there is a relation between the deposition rate ratio ($\zeta = r_{Ru}/r_{Co}$) and the alloying ratio. Thus, combining both Eq. 4.2 and Eq. 4.3 we can determine a relation between the sputtering power at each target, leading to,

$$P_{Ru} = \zeta \left(\frac{\alpha_{Co}}{\alpha_{Ru}}\right) P_{Co}, \tag{4.4}$$

$$P_{Co} = \zeta \left(\frac{\alpha_{Ru}}{\alpha_{Co}}\right) P_{Ru}. \tag{4.5}$$

From the thickness calibration results we know both α_{Ru} and α_{Co}, so we can fix either P_{Co} or P_{Ru}, to determine the co-sputtering power required to alloy the thin film sample at the desired x. In effect, our thin films were done by fixing P_{Ru} to 20 W and the P_{Co} was adjusted accordingly.

$$\tau = \frac{t}{r_{Co}\,(1+\zeta)}. \tag{4.6}$$

Eq. 4.6 shows that the deposition time (τ) is a function of both deposition rate ratio ($\zeta = r_{Ru}/r_{Co}$) and the thin film thickness (t). Thus, by employing Eqs. 4.5 and 4.3 we can determine a relation for the deposition time in terms of the power potency, thickness and deposition rate for the Ru target, that is equal to,

$$\tau = \frac{\zeta\, t}{\alpha_{Ru}(1+\zeta)\, P_{Ru}}. \tag{4.7}$$

Then, for constant thin film thicknesses of 20 nm we can determine the deposition time as function of the alloy ratio, using a fixed value for P_{Ru} while varying the power for the Co one to induce the co-sputtering alloying process.

4.1.4 Thin films with varying bi-layer Ag/Cr template thicknesses

Prior to varying the Ru concentration to modify the intrinsic Curie temperature of the thin film samples, we have to determine the conditions to induce high uniaxial magnetization along the sample's surface combined with epitaxial qualities, which depend on a high degree of the Ag/Cr bi-layer thickness. Thus, following the growth sequence schematized in Fig. 4.2(a), we have fabricated a first set of thin film samples using a fixed $x = 0.24$ Ru concentration in three different Ag/Cr templates: Ag(75 nm)/Cr(10 nm) (Fig. 4.3(a)), Ag(37.5 nm)/Cr(20 nm) (Fig. 4.3(b)) and Ag(37.5 nm)/Cr(10 nm) (Fig. 4.3(c)). Previous experimental results, have demonstrated that for the used Ru concentration the system is ferromagnetic at room temperature, and the different Ag/Cr layer thicknesses can induce epitaxial growth for the $Co_{1-x}Ru_x$.

Target/Parameters	P (W)	t (nm)	τ (s)
Ag	40	37.5	240
		75	480
Cr	100	10	130
		20	260
Co	104	20	250
Ru	20	20	250

Table 4.1: Deposition parameters for the co-sputtered $Co_{1-x}Ru_x$ ($x = 24$) using different template bilayers Ag(75 nm)/Cr(10 nm), Ag(37.5 nm)/Cr(20 nm) and Ag(37.5 nm)/Cr(10 nm) growth onto a Si(110) substrate.

The growth conditions are present in Table 4.1 where the sputter power, thickness and deposition rate for each target are indicated. The parameters were determined based on the results obtained from the XRR analysis for each material. The multilayered thin films were grown at room temperature, pressure of 3 mTorr and using the DC sputtering guns

onto Si(110) substrates. The SiO_2 capping layer was grown by RF magnetron sputtering in the same UHV sputter deposition system using a low plasma power (60 W) to achieve a precise deposition rate which in turn helps to control the layer thickness (10 nm).

Fig. 4.3 shows the X-Ray diffraction scans ($\theta - 2\theta$) for the three different thin film samples with thickness variations for the template bilayer Ag/Cr. The corresponding diffractograms were normalized to the maximum I_{Ag} intensity (I/I_{Ag}) for a better visualization. The XRD results, show that the structural characteristics are similar for all the samples independent of the bilayer template thickness. Furthermore, only diffraction peaks in the intended plane orientations are visible, i.e. Si(110), Ag(220), Cr(211) and $Co_{0.76}Ru_{0.24}$ $(10\bar{1}0)$. The dotted green line show the position for the main diffraction peak corresponding to $Co_{0.76}Ru_{0.24}$ $(10\bar{1}0)$. In effect, the proposed growth sequence is successful to produce epitaxial thin films for the system under study, due to the absence of any diffraction peak corresponding to non-epitaxial orientation, thus confirming the excellent crystallographic properties of our fabricated thin films.

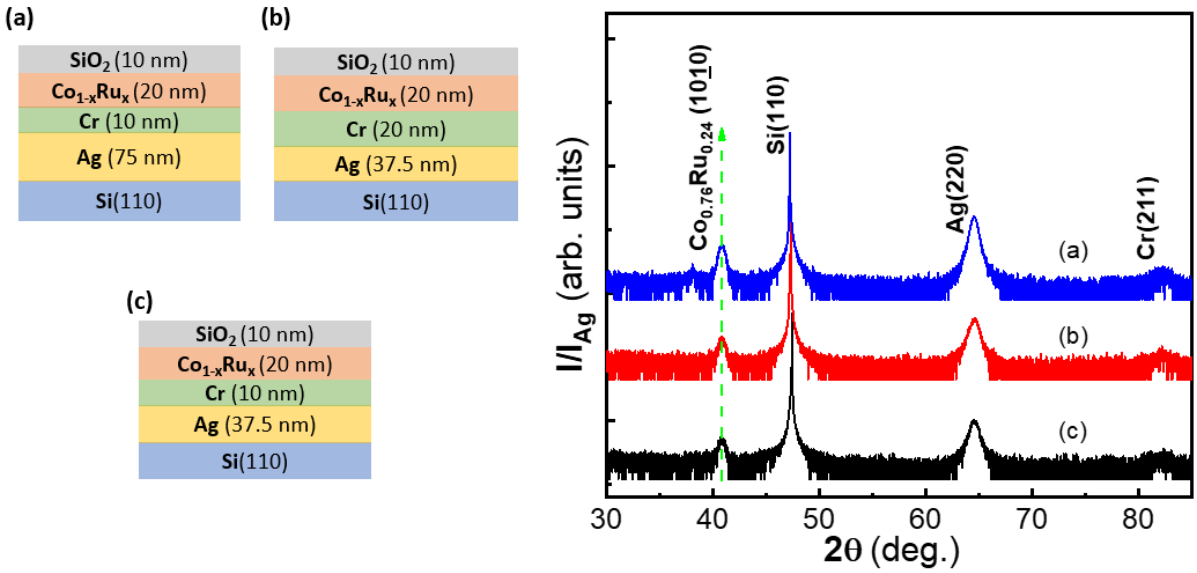

Figure 4.3: (a) Ag(75 nm)/Cr(10 nm) , (b) Ag(37.5 nm)/Cr(20 nm) and (c) Ag(37.5 nm)/Cr(10 nm) template bilayer for the $Co_{76}Ru_{24}$ (20 nm) thin films. Their corresponding X- Ray difractograms are show on the right hand size. Only the peaks related to Si(110), Cr(211), Ag(220) and $Co_{76}Ru_{24}$ $(10\bar{1}0)$ are observed, thus confirming the epitaxial qualities of the thin films.

Nevertheless, from the XRD measurements we can no infer anything about the in-plane orientation of the crystallographic c-axis for the $Co_{1-x}Ru_x$ along the sample's surface or the easy axis magnetization (EA) position. Because the crystal alignment could it be

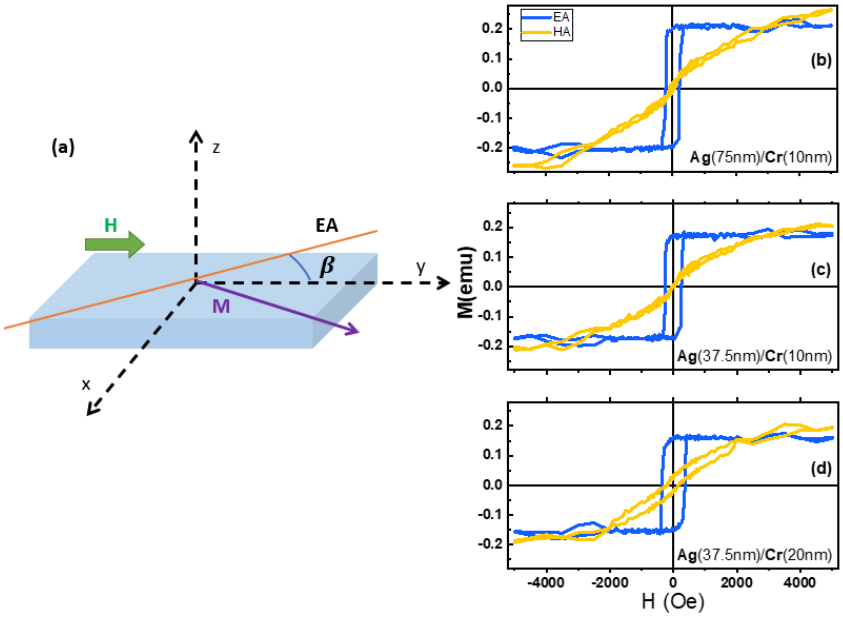

Figure 4.4: (a) Illustration for the VSM measurement used to find the corresponding EA along the sample's surface. H was applied at angle β. β = 0, when both EA and field were aligned. Then, HA was set at β = 90°. M vs. H measurements for the (b) Ag(75 nm)/Cr(10 nm) , (c) Ag(37.5 nm)/Cr(20 nm) and (d) Ag(37.5 nm)/Cr(10 nm) template bilayer are exhibited. EA (blue line) and HA (yellow line) curves showed all the similarities with the macrospin model behavior.

oriented in any random azimuthal direction, as well as the EA. For that purpose, magnetic measurements using the VSM technique, were done for the three different thin films. As a result, the magnetostatic contributions for the out-plane magnetization components, were minimal confirming that the EA lies along the samples surface. Further measurements, were performed to find the EA position as a function of the external field angle β in terms of the sample's orientation. Thus, the main idea is to reduce β to zero, leading to the exact position at which the easy magnetization axis lies. Fig. 4.4(a) shows a schematic geometrical representation for the measurement, where **H** is applied along y-axis while the sample orientation is changed towards aligning the field with EA. Then, when β is equal to zero we have the EA, whereas perpendicular to EA, the hard axis position is met (ϕ=90°). The hysteresis loops for $Co_{1-x}Ru_x$ $(10\bar{1}0)$ thin films with different bilayer thicknesses are presented in Figs.4.4(b), (c) and (d). In general, each sample have a distinctive EA (blue line) and HA (yellow line). Therefore, as expected the samples are in agreement with the Stoner-Wohlfarth [57], as for the EA we have a characteristic hysteresis loop, with

a high magnetization reversal character when in the switching field; while for the HA, the magnetization vector projection gradually rotates with minimal or none hysteretic behavior. Nevertheless, the Ag(75nm)/Cr(10nm) (Fig.4.4(b)) and Ag(37.5nm)/Cr(20nm) (Figs.4.4(d)) show a small coercive field for the HA which is not ideal for our DPT's measurements as we pursue a textbook-like macrospin model character. Hence, we have determined that the thickness condition for our sample's with varying Ru as doping agent will be fabricated using a template bilayer of Ag(37.5nm)/Cr(10nm) as we have a well-establish anisotropic uniaxial behavior combined with the high epitaxial qualities from the XRD measurements.

4.1.5 Set of samples with varying Ru concentration

After determining the corresponding deposition rate for each target, and the correct template bilayer to induce the desired epitaxial characteristics in the thin film samples. We proceeded to fabricate the co-sputtered $Co_{1-x}Ru_x$ with $0 \leq x \leq 0.26$, with an uniaxial anisotropic easy magnetization axis along the sample's surface. The overall growth sequence was as follow: on the etched Si(110) substrate a Ag(110) with 37.5 nm was

Sample / Parameters	**Target**	**P (W)**	**time (s)**
$Co_{86}Ru_{14}$	Co	204	153
	Ru	20	
$Co_{82}Ru_{18}$	Co	151	196
	Ru	20	
$Co_{78}Ru_{22}$	Co	118	240
	Ru	20	
$Co_{76}Ru_{24}$	Co	104	250
	Ru	20	
$Co_{74}Ru_{26}$	Co	94	284
	Ru	20	

Table 4.2: Growth conditions for the co-sputtered thin films $Co_{1-x}Ru_x$. P_Ru was set constant at 20 W while the Co was changed to induce the correct concentration. Likewise the deposition time was modified accordingly. Thickness for all the samples was about 20 nm.

deposited. Then, Cr(211) with a 10 nm thickness was grown followed by the $Co_{1-x}Ru_x$ $(10\bar{1}0)$ of 20 nm. Finally, an SiO_2 overcoat with 10 nm was deposited to prevent oxidation. The, conditions for the co-sputtering depositions varying the Ru content in the thin films, are presented in the Table 4.2. For all the samples independent of x concentration, Ag was deposited using 40 W during 230 s, Cr using 100 W and for 135 s and SiO_2 with a 60 W plasma strike up to 100 W for 900 s.

4.2 X-ray structural characterization

Fig. 4.5 shows the XRD scans in a $\theta - 2\theta$ configuration for an angular range of 30°-85°, for the different Ru concentrations (x) indicated in each graphic. The intensity was normalized to that of the Ag(220) peak (I/I_{Ag}). From the data we observe that all the diffractograms are similar independent of the doping concentration. A single sharp peak related to $Co_{1-x}Ru_x$ alloyed phase in a $(10\bar{1}0)$ preferential orientation is visible in each plot (green dotted line), thus confirming the high oriented nature of the thin films, with an in-plane hcp c-axis which corresponds to the easy magnetization axis. Likewise, as expected only peaks in the epitaxial orientation are visible for Si(110), Ag(220) and Cr(211). As the SiO_2 forms an amorphous compound there is no diffraction related to it.

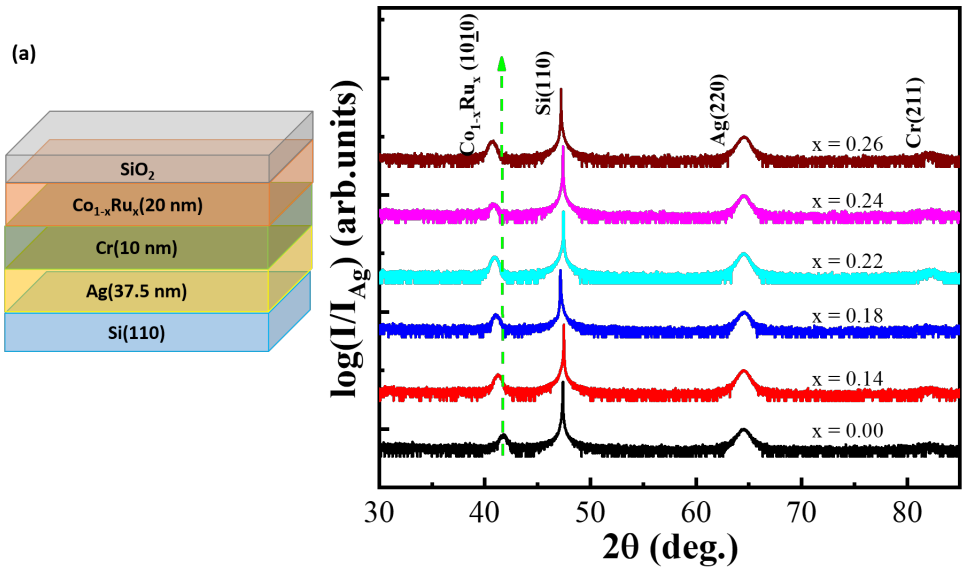

Figure 4.5: (a) $Co_{1-x}Ru_x$ thin film sample schematics indicating the thicknesses for each layer and (b) X-Ray diffraction scans for the co-sputtered thin film samples with $0 \leq x \leq 0.24$. Only epitaxial peaks are visible and the dotted green line shows the main peak

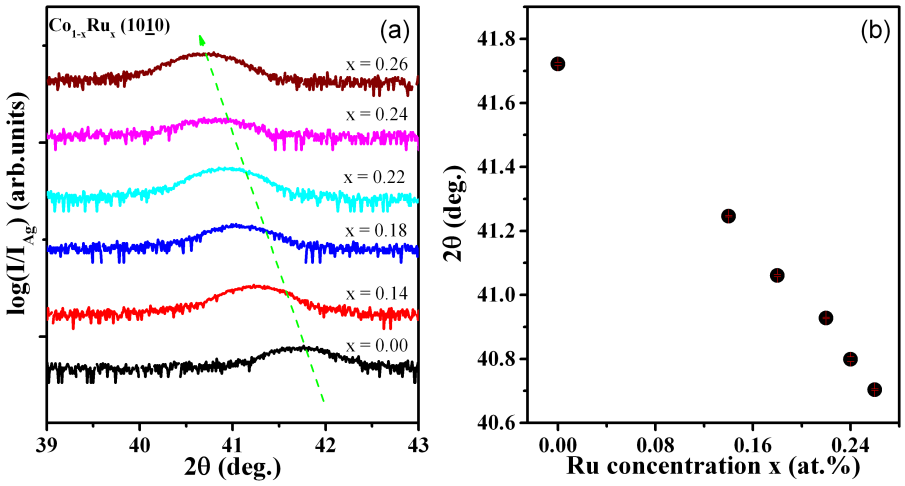

Figure 4.6: (a) XRD main peak for $Co_{1-x}Ru_x$ $(10\bar{1}0)$with their doping concentration is shown. A decrease towards smaller diffraction angles is visible as represented by the green dotted arrow. (b) Shifted $Co_{1-x}Ru_x$ $(10\bar{1}0)$peak position (2θ) as a function of Ru concentration.

A close inspection of this main diffraction peak for $Co_{1-x}Ru_x$ $(10\bar{1}0)$, shows that as the Ru content increases a shift towards smaller diffraction angles appear as shown by the dotted green line in Fig. 4.6(a). The angle values are presented in Fig. 4.6(b) for $0 \leq x \leq 0.26$, and it is in accordance with previous reports for the same kind of thin films [39]. Despite of this behavior, all the samples are epitaxial with an in-plane EA, and their crystallographic properties are similar in relation to the principal diffraction peak height and width. Likewise, as our thin films followed nearly the same growth sequence that the one reported by Idigoras *et. al.* in reference [39] where rocking curve measurements and ϕ-scans did not show any evidence of systematic growth quality variations as a function of Ru content, we can infer that in principle their magnetic properties should be comparable and representative of their different T_c's, and not their inherent crystal quality.

4.3 Magnetic characterization

To confirm the ferromagnetic nature and anisotropic behavior of the samples, magnetic **M** vs. **H** measurements were taken from ± 2 kOe at room temperature (RT) using a VSM. The amplitude of this quasi-static external field is more than enough to fully saturate the samples. Fig. 4.7 shows the normalized magnetization **M** over the maximum measured magnetization $\mathbf{M}_{Max}$ as a function of the external magnetic field **H**, measured along the in-plane EA (blue line) and the HA axis (yellow line) for all the $Co_{1-x}Ru_x$ samples. Ru

concentration is shown in each graph.

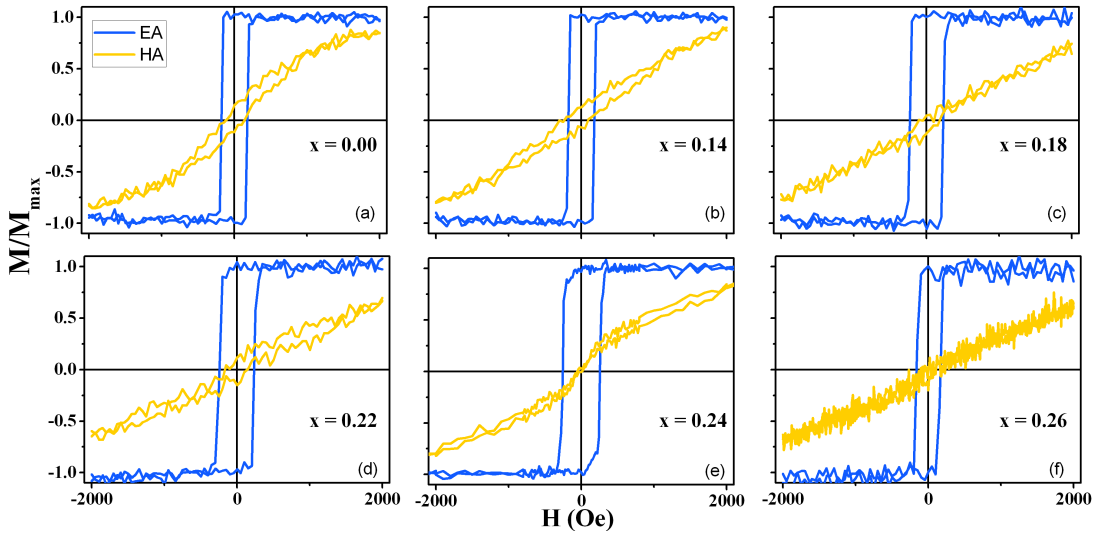

Figure 4.7: Experimental M vs. H curves for $Co_{1-x}Ru_x$ $(10\bar{1}0)$thin film samples measured along the EA (blue line) and HA (yellow line) for different Ru concentrations (a) $x = 0.00$, (b) $x = 0.14$, (c) $x = 0.18$, (d) $x = 0.22$, (e) $x = 0.24$ and (f) $x = 0.26$. The magnetization was normalized to its maximum value and the diamagnetic contribution of the substrate was removed.

It can seen in all of the graphs that for all of our sample set, a square-like loop was retrieved along the EA in plane axis with sharp magnetization reversal at the coercive field which is equal to the switching one. This behavior mimics the bistable nature of an Ising-like model, in which the magnetization switches in between two stable states, i.e., $\pm M_s$ [20, 38, 39]. Such quasi-static hysteresis loops are measured at a period that is orders of magnitude higher than the experimental conditions used for our DPT observations. Correspondingly, nucleated reversal domains actually have sufficient time to propagate through the entire sample in between two subsequent data points, making the hysteresis loop appear very abrupt, and thus suppress the dynamic behavior that defines the physics of dynamic phase transitions.

A rather small increase in the coercive field values as function of x doping is noticeable in Fig. 4.7. This effect can be related to a modification in the magnetocrystalline energy due to the increasing Ru concentration. This observed x-dependence of H_c is fairly minor, an about 15% effect. Therefore, more energy is necessary to invert the magnetization state, because the ferromagnetic quality of the sample diminishes as x increases. This is an important fact that must be taken into account when we approach the $H_0 - H_b$ dynamic phase space (section 5.3).

Furthermore, when the field was applied along the HA the samples shown a rotational behavior of the magnetization vector with none or minimal hysteresis, thus confirming that in fact there is a induced anisotropy within the sample's surface. No saturation was reached for the HA because the external field was not high enough to produce the saturation of the magnetic moments, as a simple comparison with Fig. 4.4 exhibit where $H = \pm 5$ kOe. This does not affect the DPTs measurements, as they are done along EA and at fields larger than the switching field.

A deeper exploration of the uniaxial in-plane anisotropy in our samples was examined using the set-up illustrated in Fig. 4.4(a). The thin film was placed in a strong external field to fully saturate the sample and then as **H** was removed its remanent magnetization was measured (M_r) as function of an arbitrary angle β. β denotes the angle at which the external field was applied within the surface's plane in reference to the easy axis. The normalized remanent magnetization (M_r/M_s) is shown in Fig. 4.8 (black dots) for three different samples $x = 0.0$, 0.14 and 0.22. It is evident that for $\beta = 0$ and $\beta = 180°$, $M_r M_s$ is very close to 1, while for $\beta = 90°$and $\beta = 270°$ M_r nearly vanishes. Consequently, we have a 180°periodicity in the samples, which denotes that $M_r M_s$ is maximum when the external field **H** is applied along the EA direction, whereas this ratio is close to zero when

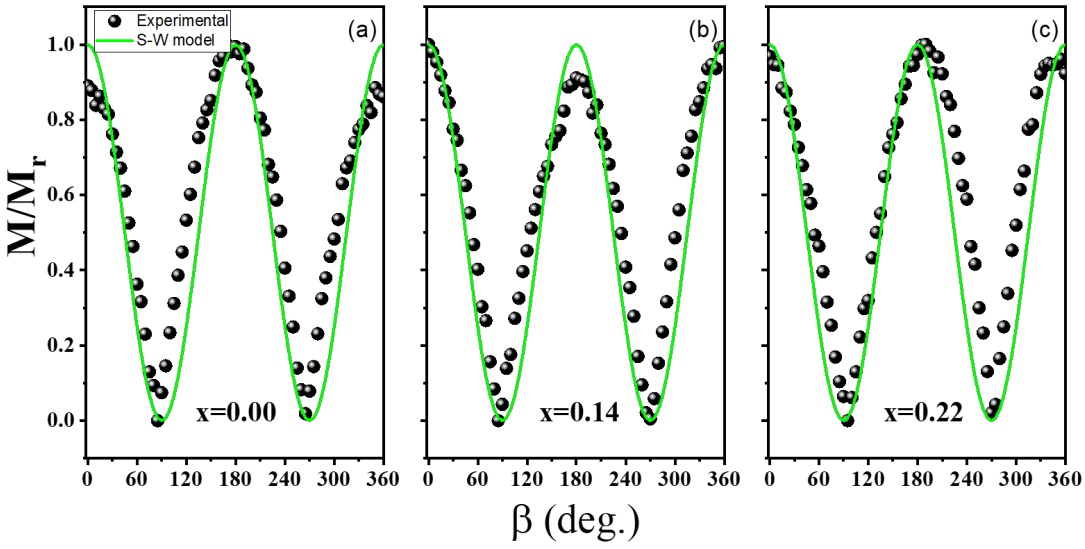

Figure 4.8: Experimental exploration of the in-plane anisotropy for three different thin film samples (a) $x = 0.00$, (b) $x = 0.14$ and (c) $x = 0.22$. The remanent magnetization (black dots) was measured at an angle β with respect to the pick-up coils in the VSM equipment, where $\beta = 0$ was aligned with the EA while for $\beta = 90°$we have the HA. The samples shown nearly a textbook-like Stoner-Wolfhart behavior as indicated by the green solid line.

applied along the hard magnetization axis (HA). Our results agree with the analytical predictions of the Stoner Wohlfarth model (see section 2.4.2) for a uniformly magnetized particle with uniaxial anisotropy, as represented by the green solid line [57, 159]. For all the other samples, the VSM data (not shown here) look virtually identical. Consequently, they all exhibit a uniaxial in-plane anisotropy.

Additionally, the evolution of the saturation magnetization (M_s) against temperature, was monitored using the SQUID-VSM equipment in a range from 5 K to 350 K. This was done to determine the evolution of the Curie temperature in terms of the Ru doping. The measurements were taken applying a small bias field ($\mathbf{H}$ = 100 Oe) along the sample's easy magnetization axis.

As the Curie temperature has values above the measurement range, an extrapolation of T_c was determined by using the analytical expression proposed by Kuz'min for the behavior of the M(T) curve [160]. Then,

$$M(T) = M_s(0)\left[1 - s\left(\frac{T}{T_c}\right)^{\frac{3}{2}} - (1-s)\left(\frac{T}{T_c}\right)^{p}\right]^{\frac{1}{3}} \tag{4.8}$$

where $M_s(0)$ is the spontaneous magnetization, while s and p are fitting parameters. s defines the overall shape of the curve and has values $s > 0$, while $p = \frac{5}{2}$ for ferromagnetic systems as in our case. An example of the M(T) least square fit for the $Co_{0.88}Ru_{0.22}$ thin film is shown in Fig. 4.9(a), where the experimental data is represented by the black

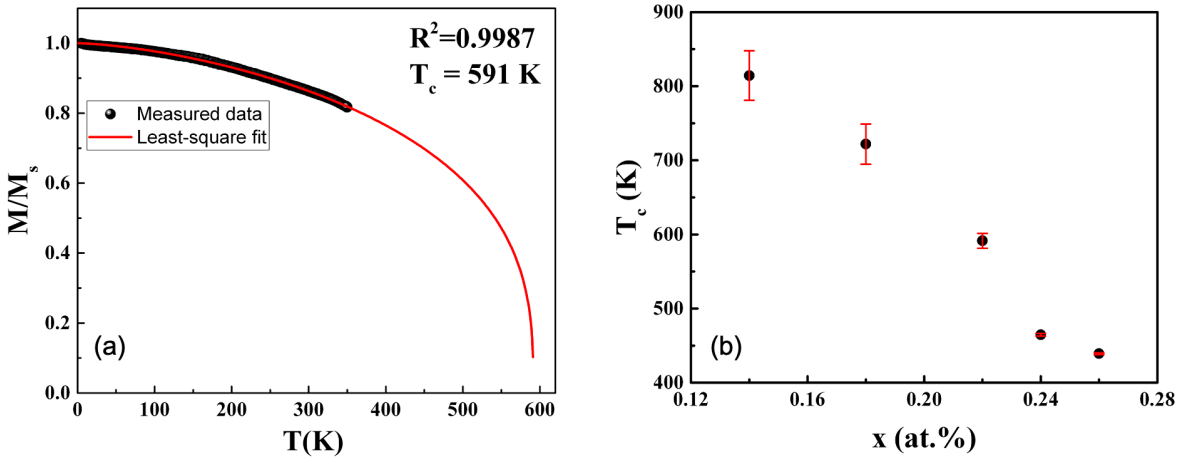

Figure 4.9: (a) Magnetization against temperature (black dots) for a $Co_{0.88}Ru_{0.22}$ thin film. The red solid line represents the least-square fit using Eq. 4.8. (b) Extrapolated T_c (black dots) values for the $Co_{1-x}Ru_x$ $(10\bar{1}0)$thin film set as function of Ru concentration.

circles while the fitted function by the red line. A high match of the fitting function with the measured data can be seen, with a $R^2 = 0.9987$. A detailed description of the model used to fit M(T) and their corresponding fitting parameters for each sample are presented in appendix B.

Furthermore, Fig. 4.9(b) presents the extrapolated T_c values for the whole $Co_{1-x}Ru_x$ sample set. As can be observed from our data, there is a clear decrease in T_c as the Ru content increases. This T_c reduction is similar to those reported in bulk and thin films for $Co_{1-x}Ru_x$ alloys, since Ru reduces the effective exchange coupling in our alloys [39, 40, 161]. The changing size of the error bars in Fig. 4.9(b) is attributed to the fact that for low Ru content we are extrapolating to temperatures far larger than our measured temperature interval (5 K – 350 K), while for high Ru content we measure closer to the Curie temperature.

Thus, our $Co_{1-x}Ru_x$ alloyed thin films are highly oriented, FM at RT and have an in-plane uniaxial magnetic behavior. Furthermore, they exhibit varying T_c by means of Ru doping. Therefore, we have a set of suitable test samples that will allow studying the dynamic behavior in the vicinity of DPT, for the different reduced temperature (T/T_c) values shown in Fig. 4.9(b)., while keeping the experimental measurement temperature constant at room temperature.

Chapter 5

Dynamical phase transitions for different Curie temperatures

The experimental detection of dynamic phase transition in materials with different Curie temperatures is discussed in this chapter. In the first part, we present the DPT detection scheme that uses mainly an ultransensitive T-MOKE. Combined with the T-MOKE we used an iterative field routine which enable a high quality and low deviation in the time dependent field amplitude and bias field, a condition that must be met in order to study the dynamic properties of the system near DPT. Our set-up allow us to study the dynamic phase space by two different means. Thus, in section 5.2 we have the traditional $\langle Q \rangle(P, H_b)$ measurements, while in section 5.3 we have a propose a new approach $\langle Q \rangle(H_0, H_b)$ that permits to extend the study of DPT in a wider phase space. In the last part of the chapter, the metamagnetic fluctuations are studied as function of the T/T_c ratio for all our samples.

5.1 Dynamic phase transition experimental set-up

The corresponding phase space measurements in the vicinity of DPT, for the $Co_{1-x}Ru_x$ $(10\bar{1}0)$ thin films with different intrinsic T_c and thus varying T/T_c ratios, were carried out using an ultrasensitive transversal magneto-optical Kerr effect (T-MOKE) set-up. The basis of this approach were discussed previously in section 3.4.1. Our set-up is show in Fig. 5.1 with their respective components.

The beam path for our measurements is presented in Fig. 5.2(a). The system uses an

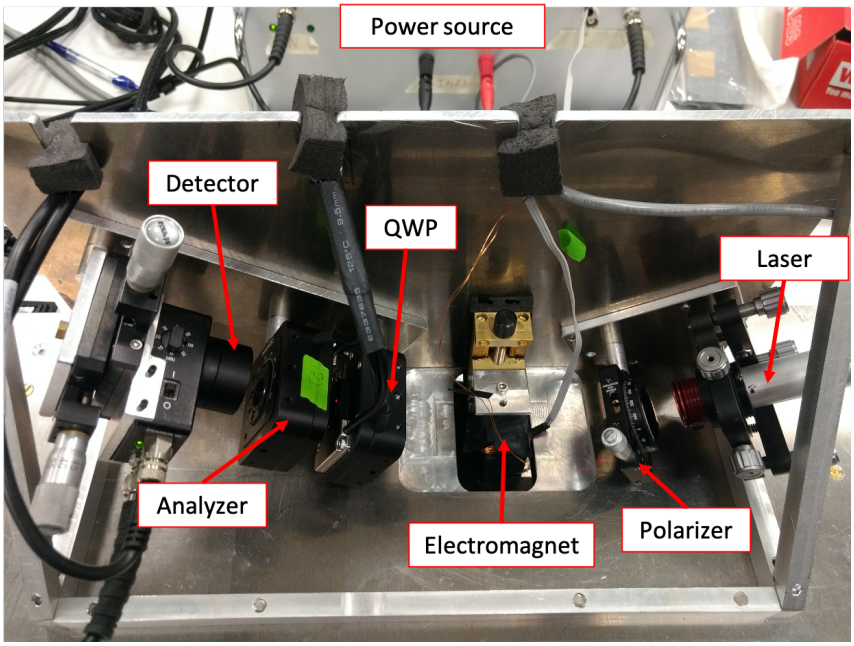

Figure 5.1: Ultransensitive T-MOKE set-up at CIC nanoGUNE. The components are shown in the picture.

ultra-low-noise laser with λ= 635 nm and 5 mW power output during the measurements. This incident electromagnetic wave coming from the laser, passes through a fixed first polarizer and then is reflected by the sample, which is positioned inside the gap of the electromagnet (see Fig. 5.2(b)). The external field H(t) is produced by an AC power supply source and then is applied transversally with respect to the laser's incident plane. Then, the reflected beam goes through a rotatable quarter-wave plate retarder (QWP) to a second rotatable polarizer (analyzer). Lastly, the transmitted light intensity is col-

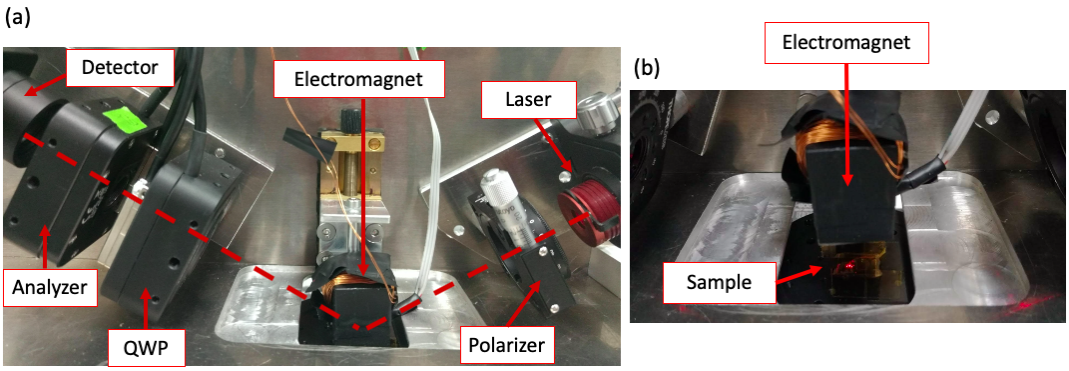

Figure 5.2: (a) Laser beam path (dotted red line) for the ultrasensitive T-MOKE for our detection scheme. The sample which is inside the electromagnet is shown in (b), where the coming beam reflects in the sample's surface.

lected by a photodetector with built-in pre-amplifier. To limit the light level reaching the photodetector, coming from the purely optical reflected light, that does not carry magneto-optical signal information, QWP and the analyzer are rotated iteratively. When the minimum intensity is detected, P2 is rotated 2 degrees away from the extinction position, thus a large relative magneto-optical T-MOKE signal and a sufficient light level can be easily detected with our set-up. Our set-up enables to measure the effective polarization rather than the conventional intensity for T-MOKE measurements, which enhances the sensitivity about 20 times [143, 144].

The whole system is fully automatized using a LabVIEW interface which controls a NI USB-4431 sound and vibration device. This system has 4 differential analog input channels, which collect the incoming data from the photodetector, hall detector (magnetic field amplitude) and power supply. Furthermore, it has one output channel which enables to produce an AC sinusoidal signal to induce the time-dependent magnetic field in the electromagnet. The device has a maximum sample rate of 102.4 kS/s with a built-in high pass filter cutoff frequency of 0.8 Hz [162]. Thus, due to the high sensibility of our T-MOKE set-up combined with its instrumental capabilities, time-resolved full hysteresis loops can be recorded down to P = 3.3 ms with excellent signal-to-noise ratio.

5.1.1 Field stability calibration

As already described, H_b or the bias field is the conjugated field associated with Q the dynamic order parameter, as seen on Fig. 2.6(b). Correspondingly, small bias field amplitude, i.e., below $\pm$ 2 Oe, can induce large changes in the dynamic parameter response [20, 34]. Therefore, it is crucial that for the entire DPTs measurement, high field stability in terms of time-dependent field amplitude and bias field must be ensured; likewise it is important to avoid any signal frequency drifts.

Hence, we have implemented an iterative routine to minimize field fluctuations for H_0 and H_b for the applied periods. After establishing the current stability of our power source, we applied a time-dependent field at a known amplitude and high period for around 250 full-cycles, where no bias field was used. Afterwards, the period was decreased towards the minimum values reachable for our set-up. The voltage and current output coming from the power supply was collected in each measurement, and then using a Matlab script which consisted of an iterative seventh degree polynomial $I(V)$, we adjusted the

data to the desired field amplitudes $I \propto H$. Figs. 5.3(a) and 5.3(b) show the results after the iterative calibration for an applied field of $H_0 = 428$ Oe, for $P = 3.3$ ms and $P = 33.3$ ms respectively. The mean field value and its deviation values are shown in each graphic. A similar approach was done to correct the bias field amplitude. Figs. 5.3(c) and 5.3(d) present the corresponding bias field ($H_b = 4$) values measured at a constant field amplitude, $H_0 = 428$ Oe at $P = 3.3$ ms and $P = 33.3$ ms for 250 full-cycles correspondingly. From the data, we extract field deviations of maximum 250 mOe.

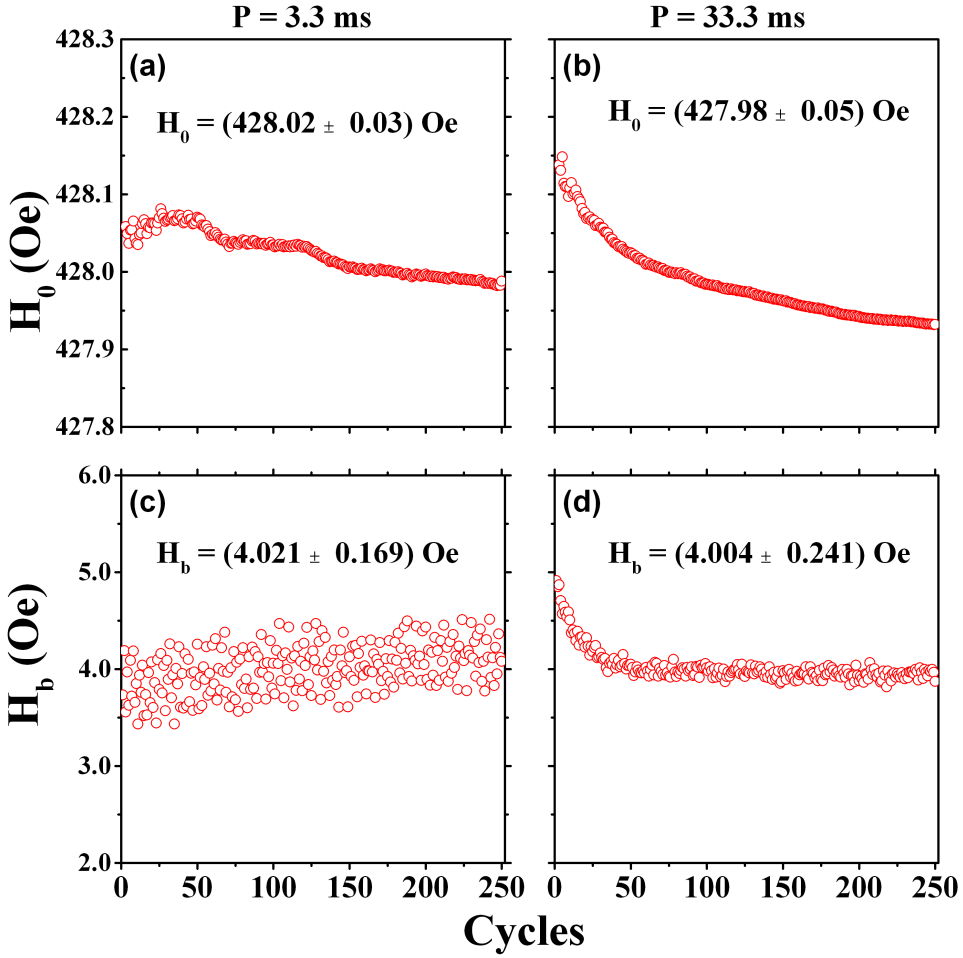

Figure 5.3: Field stability experimental results after implementing an iterative polynomial routine. (a) and (b) show the results for a fixed $H_0 = 428$ Oe with zero bias and $P = 3.3$ ms and $P = 33.3$ ms, respectively. (c) and (d) correspond to $H_b = 4$ Oe at fixed period values. The measurements were taken averaging over 250 different full-cycles.

Fig. 5.4 shows the time-dependent field amplitudes as function of the applied period ($3.3 \leq P \leq 33.3$) for $H_0 = 428$ Oe and zero bias field. It is noticeable that for higher period (lower frequencies) the system has a high stability with lower deviation values at

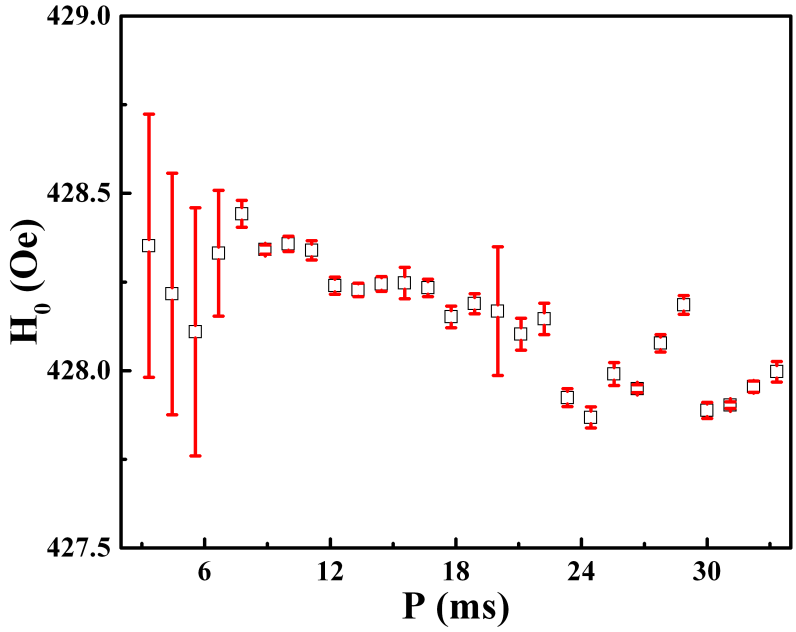

Figure 5.4: Field deviations for $H_0 = 428$ Oe as function of the measurement period range ($3.3 \leq P \leq 33.3$ ms). For larger periods we have small variations whereas for smaller values there is an increase, which does not affect the dynamic phase measurements as they are not larger than $\pm$ 1 Oe.

nearly constant field values. Although, in the lower period (higher frequency) regime, we have larger deviation values as the error bars show. Despite of this, it does not affect our DPT's detection scheme, as for these particular values our samples are in general in the ordered dynamic phase (FM) and the dynamic order parameter can only take two possible values $Q = \pm 1$ independent of the bias field.

A broader phase map for $H_0(P, H_b)$ is displayed in Fig. 5.5. This graphic, allows to examine the overall behavior of H_0 as function of H_b and P. H_0 was set to 428 Oe. Light blue and dark blue zones which correspond to most of the phase space shown in the graph, correspond to small deviation ($\leq \pm$ 0.6 Oe) values for our fixed H_0. Whereas red colored zones are related to larger variations ($\pm$1 Oe). As we already discussed, this behavior does not affect are dynamic phase transition detection.

Thus, in all our experiments, for $H(t)$ periods in the region of 3.3 ms up to 33.3 ms we have achieved field amplitudes deviation of less than $\pm$ 1 Oe for H_0 amplitudes up to 600 Oe and bias field variations that are less than $\pm$ 400 mOe for all values of H_0 and H_b that we utilized in this study. Therefore, our field stability routine ensure high field fidelity throughout our dynamic phase transition measurements. Both, dynamic and

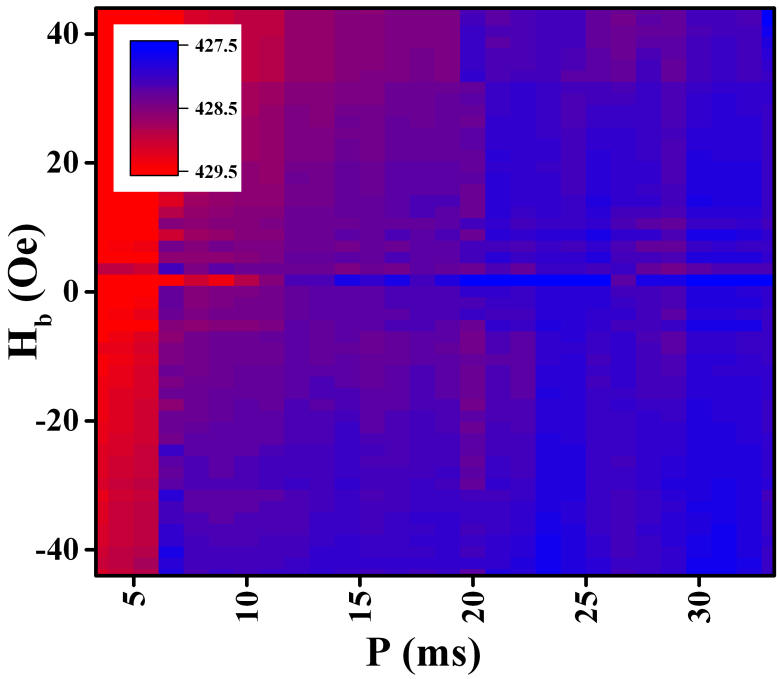

Figure 5.5: $H_0(P, H_b)$ map for a fixed $H_0 = 428$ Oe amplitude in a period range of 3.3 ms up to 33.3 ms. Light blue and dark blue zones correspond to variations in a range of $\leq \pm$ 0.6 Oe. The red colored zones have approximately variations of ± 1 Oe. In general, our field stability is more than enough to detect dynamic phase transitions.

static magnetic fields were applied using an electromagnet with minimal coercive field and low latency.

5.1.2 DPT's measurement routine

To detect full magnetization reversal once the field amplitude is strong enough to induce it in the sample, $H(t)$ is applied in such a way that is aligned along with the sample's EA. The orientation of the sample's EA axis, was previously determined using the VSM measurements shown in section 4.3.

An example of the sinusoidal field $H(t)$ signal used for our measurements is shown in Fig. 5.6(a). The overall period was set to $P = 3.3$ ms, $H_0 = 430$ Oe without an applied bias field ($H_b = 0$). Since we detect light intensity variations coming from the T-MOKE set-up, an appropriate correspondence between this light intensity I and its equivalent magnetization degree was found. For that purpose, a reference field H_{ref} was used, which is larger in amplitude in comparison to H_0 to ensure that the sample is fully saturated, and thus we induce a full reversal response in the system. Correspondingly,

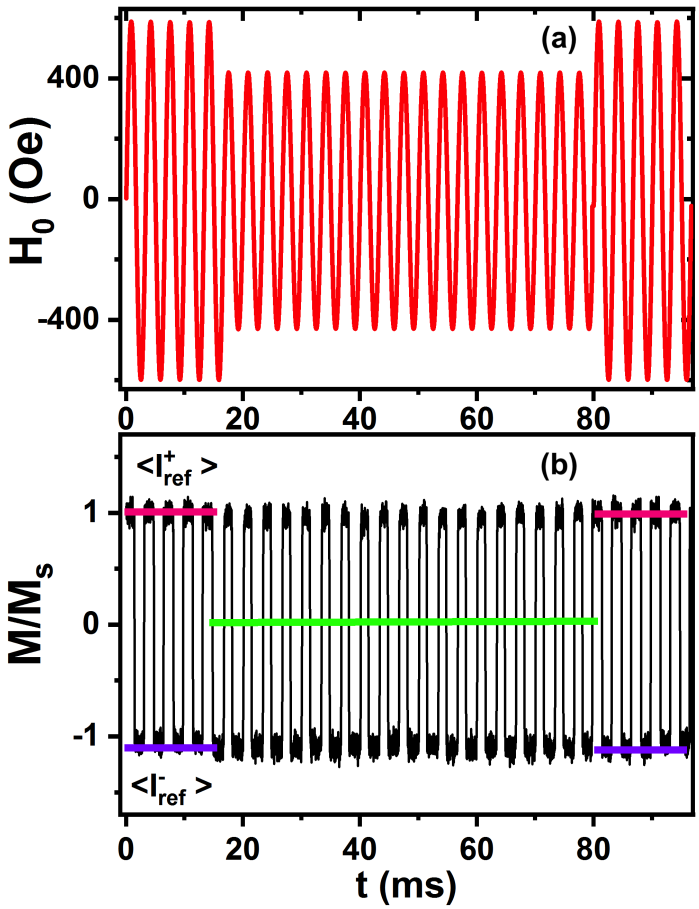

Figure 5.6: (a) External time-dependent field signal measurement for H_0 = 430 Oe, H_b = 0 and P = 3.3 ms. The first and last five cycles were applied at H_{ref} = 580 Oe which are used as reference to achieve full magnetization reversal in the samples. (b) T-MOKE signal trace for the $Co_{0.76}Ru_{0.24}$ which shows the full magnetization reversal character where the time-averaged magnetization value $\langle Q \rangle$ = 0 (green solid line).

the values of intensity measured at these points allow us to define the quantities $\langle I^+_{ref} \rangle$ for the maximum positive (salmon lines) and $\langle I^-_{ref} \rangle$ minimum negative (violet lines) that correspond to the negatively and positively saturated magnetization states, respectively (see Fig. 5.6(b)). Therefore, we can correlate $\pm M_s$ to a maximum (or minimum) Kerr intensity value, as $\Delta I/I$ is proportional to the effective polarization changes upon the inversion of the magnetization (see Eq. 3.12). As a result, we can calibrate accordingly the intensity values to the magnetization ones (see Fig. 5.6(b)).

Another important function of H_{ref} is associated to monitoring the stability of our experimental the set-up [20]. So, this reference field is applied at the beginning and the end of each full dynamic measurement run (first and last five cycles shown in Fig. 5.6(a)).

If any small drifts in field arise during the measurement as function of the signal time-evolution, a proper compensation routine can be implemented to correct such effects. A final consideration related to H_{ref}, its that for the reference measurement cycles, the bias field is kept constant at $H_b = 0$, this is done to ensure that the order parameter is always near or equal to zero and both saturated states $\pm M_s$, and thus can be quantified with equal precision.

Fig. 5.6(b), exhibits the corresponding magneto-optical time traces measured by using our ultrasensitive T-MOKE set-up when $H(t)$ is applied. The Kerr intensity data normalized to M/M_s displays an almost square-like behavior, evidencing a full reversal character directly related to the high magnetization reversal of our samples due to their anisotropic behavior. Furthermore, when a field amplitude of $H_0 = 430$ Oe is applied, the magnetization state switches back and forth from positive to negative saturation, just as in the case of the intended reference data at $H_{ref} = 580$ Oe. Thus, even at H_0, we have a full reversal of the magnetization, hence the cycle averaged magnetization vanishes, i.e. $Q = 0$ (solid green line), and the system is in the dynamically disordered state. This data also show that the signal-to-noise ratio is very good and the order parameter can be very precisely determined, even for a single measurement cycle, which is especially relevant for higher-order observables, such as fluctuations.

Fig. 5.7 illustrates the bias field effect on the normalized time-dependent magnetization response, for the $Co0.76Ru_{0.24}$ thin film, which has a relatively high T/T_c ratio (≈ 0.65) and a large magneto-optical signal. From Fig. 5.7(a) we can see that when $H_b = 0$, for a constant set of parameters (H_0, H_b, and P) the average order parameter $\langle Q \rangle$ is equal to zero, displayed as a solid green line. The red solid line is related to $\langle Q \rangle$ for the reference field, which must be always equal or close to zero to ensure that the measurement starts and finish from a known dynamical ordered state.

Furthermore, when a small positive bias field ($H_b = +5$ Oe) is applied while keeping H_0 and P constant, the signal average becomes $\langle Q \rangle \approx 1$ (solid green line in Fig. 5.7(b)). Likewise, a small negative bias field ($H_b = -5$ Oe) causes a significant suppression of the time-magnetization response and leads to $\langle Q \rangle \approx -1$ (solid green line in Fig. 5.7(c)). Thus, the system is in the so-called paramagnetic dynamic regime in the dynamic phase space.

A close inspection of Fig. 5.7(b) and Fig. 5.7(c) shows that there is a difference in

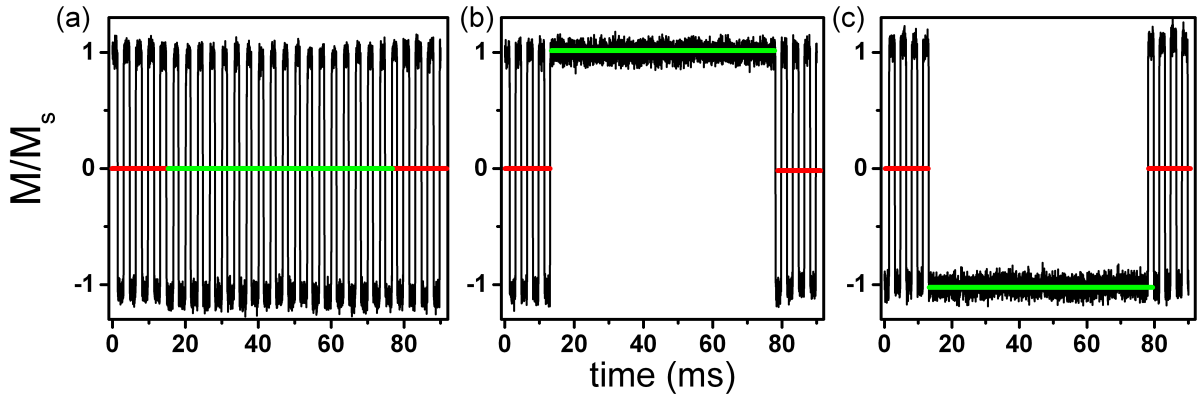

Figure 5.7: T-MOKE signal normalized to M/M_s as function of the external sinusoidal field $H(t)$ with $P = 3.3$ ms, $H_0 = 430$ Oe and $H_{ref} = 580$ Oe for (a) $H_b = 0$, (b) $H_b = +5$ Oe and (c) $H_b = -5$ Oe. The red solid line represents the time-averaged magnetization ($\langle Q \rangle$) for the reference field, i.e. $\langle Q \rangle = 0$. The green solid line shows $\langle Q \rangle$ as function of H_b while applying H_0 at fixed amplitude, thus we have $\langle Q \rangle = 0$, $\langle Q \rangle = +1$ and $\langle Q \rangle = -1$, respectively.

phase for both field sequences. For positive bias fields, $H(t)$ is applied with a phase $\phi = 0$ in terms of the harmonic sine function ($\sin(\omega t + \phi)$), whereas for negative bias fields we have a π phase shift. This is done in all our DPT's measurements, to synchronize the bias field with the last reference field pulse, so any transient behavior can be avoided [20]. So, for positive values of H_b we start from a known positive ordered state while for negative values of H_b, the corresponding negative ordered state is considered. Furthermore, this prevents the occurrence of any hysteretic behavior related to a first-order phase transition as a function of H_b in the dynamically ordered regime. This synchronization in between the bias field and starting magnetic state is being done to minimize the transient time that is needed to achieve a stable dynamic sequence. For $H_b \leq 0$, only one of the two possible dynamic states and associated $M(t)$ sequences shown in Fig. 2.7(c) is dynamically stable, while the other one is metastable, generally leading to transient dynamic behavior, including a time-dependent Q vs. H_b hysteresis [20]. Thus, by synchronizing magnetic bias field and magnetic starting state, we preselect a starting point that is close to the stable dynamic state and avoid the metastable dynamic state, which reduces transient dynamics and makes our measurements more efficient[1].

Finally, to generate the corresponding $\langle Q \rangle(P, H_b)$ (or $\langle Q \rangle(H_0, H_b)$) phase space maps

[1]The ultrasensitive T-MOKE used in all of our measurements has a signal to noise ratio (SNR) of 100:1 in relation to conventional T-MOKE. This SNR was reached even for signals of the order of several 10^{-6}, from which the estimated sensitivity levels are around 10^{-8}

to study the dynamic phase transition phenomena for samples with different Curie temperatures, we have recorded the type of experimental plots shown in Fig. 5.7. Thus, for a fixed field period (or field amplitude, H_0) and constant bias field amplitude, a set of $N(H_{ref}) = 5$ reference field cycles were applied at the beginning of each run. Afterwards, $H(t)$ is applied for a set of $N = 250$ field cycles. From those cycles, the first 150 are removed, keeping the last 100 field cycles. This is done to avoid that either any transient state shows up in the data analysis, or larger field fluctuations caused by the large length of time which used to record the data. At last, $N(H_{ref}) = 5$ reference field cycles are employed at the end of the run.

This prior routine is repeated five different times in a continuous fashion, therefore we record around 500 cycles at H_0 which translate in 500 different dynamic order parameter values. By doing so, we improve the $\langle Q \rangle$ correlated statistics and improve the stability of the system in terms of the running time. Afterwards, $+H_b$ is decreases from a high positive bias field towards a small negative bias while keeping P or H_0 invariable. Likewise, $-H_b$ is set to a high negative value and then decreased to a small positive bias field. This is done to avoid transient behavior in our data set. Then, either P or H_0 is changed and the measurement starts all over. The starting values for either P or H_0 in their corresponding experimental phase spaces, is set in a way that we always start from the disordered state (PM) towards a dynamically ordered one. Hence, we start from larger P or H_0 value and decrease it, until surpassing the dynamic phase transition critical point, to account for the whole dynamic phase space.

5.2 Dynamic phase transitions in the $\langle Q \rangle(P, H_b)$ phase space

Figs. 5.8(a) - (e) shows the experimental mean dynamic parameter $\langle Q \rangle$ data measured as a function of P and H_b as color-coded maps for different fixed field amplitudes from $H_0 = 424$ Oe to $H_0 = 432$ Oe varying at a rate of 2 Oe steps, respectively. These specific field amplitudes were used here to measure the $\langle Q \rangle(P, H_b)$ order parameter behavior in the $P - H_b$ phase space for the $Co_{0.76}Ru_{0.24}$ thin film. For all the measurements the reference field was set to 580 Oe and 28 different period values were monitored from 33.3 ms to 3.3 ms. The color scale bar that is applicable for $\langle Q \rangle$ is shown as an inset on the

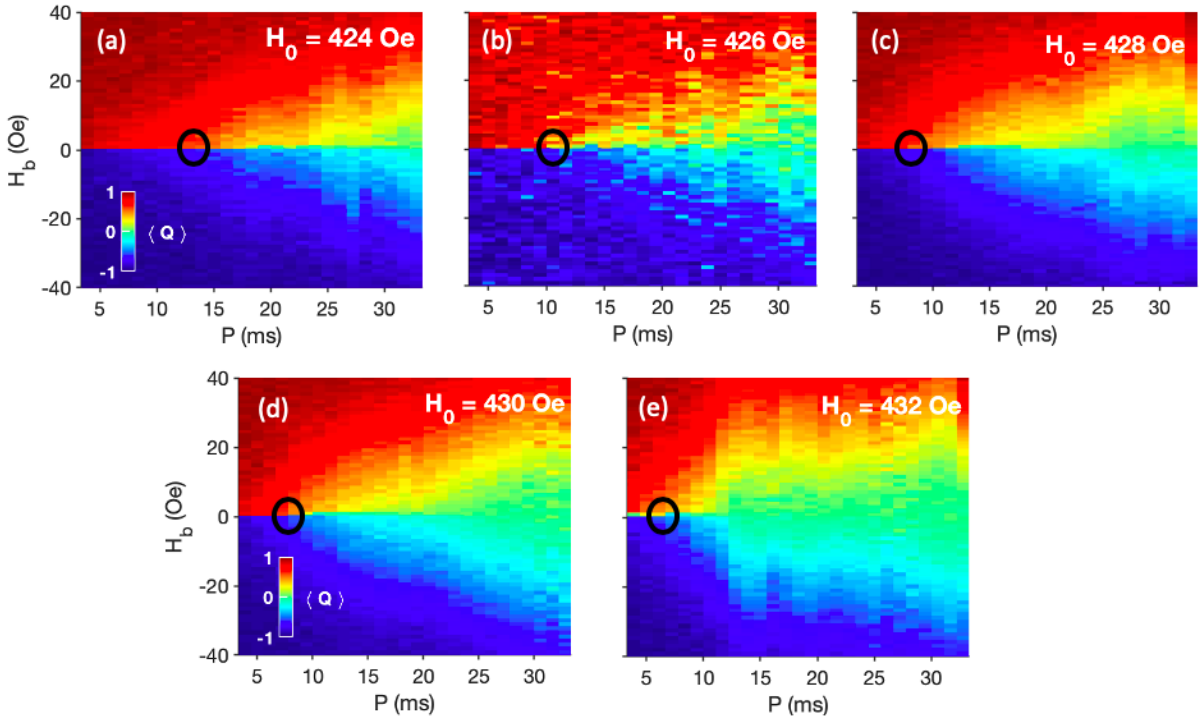

Figure 5.8: Experimental $\langle Q\rangle(P, H_b)$-data maps for (a) $H_0 = 424$ Oe, (b) $H_0 = 426$ Oe, (c) $H_0 = 428$ Oe, (d) $H_0 = 430$ Oe and (e) $H_0 = 432$ Oe, measured for a $Co_{0.76}Ru_{0.24}$ thin film. For all the measurements $H_{ref} = 580$ Oe and $3.3 \leq P \leq 33.3$ ms. P_c is represented by the solid line. The color scale bar applicable for $\langle Q\rangle$ is shown as an inset on the left-hand side of each graph.

left-hand side of each graph.

The corresponding area at which the critical period P_c for the DPT takes place, is highlighted by the solid line circle[2]. For all the H_0 amplitudes studied, we notice that there is a phase line for $H_b = 0$ below P_c, at which the values or color of $\langle Q\rangle$ abruptly changes from red ($\langle Q\rangle = +1$) to blue ($\langle Q\rangle = -1$), whereas for $P > P_c$ this phase line is absent due to the nature of the paramagnetic dynamic phase. In this disordered state, there is a gradual change from $\langle Q\rangle = 0$, shown in green, towards $\langle Q\rangle \neq 0$ as $|H_b|$ increases, which is not associated with a dynamic phase transition [7, 20, 89] but a first order transition as depicted in Fig. 2.7(b). Therefore, these experimental measurements evidence that we can successfully detect dynamic phase transitions in our samples and map out the order parameter $\langle Q\rangle(P, H_b)$ throughout the relevant phase space.

[2] P_c was not determined from this measurements because we were merely interested in testing the capability of our set-up to detect conventional $\langle Q\rangle(P, H_b)$ phase maps

Another important experimental observation from Figs. 5.8(a) - (e) is that upon applying higher oscillation field amplitudes H_0, the ferromagnetic dynamic state shift towards lower P values [7, 20]. This behavior was expected as figure 2.8 already shown. Therefore, as the field amplitude H_0 increases an appreciable shift of the critical point P_c towards lower absolute P values occurs. In fact, the H_0 dependence on P_c is rather strong, whereas the P dependence of the dynamic behavior is comparatively weaker. Whilst we are changing P by one order of magnitude (3.3 ms to 33.3 ms) to explore the phase space that is visible in both figures, the very small change in the field amplitude H_0 of less than 0.5% modifies the dynamic response in its absolute position quite substantially. Hence, a P dependent study is very suitable to explore fine details of the phase space near P_c, as demonstrated by Fig. 5.8.

However, if one would like to explore a larger portion of the dynamic phase space, P dependent measurements are not particularly suitable, because P would have to change over many orders of magnitude, while keeping all other conditions exactly constant, which is excessively problematic in any experiment. Consequently, it is much more practical from an experimental point of view, to study the order parameter as a function of H_0 and H_b for fixed frequencies. Such an approach will enable a wide range phase space exploration, and correspondingly enable us to investigate the T/T_c dependence of dynamic magnetization behavior in such a wider phase space surrounding the critical point, which is our main goal. Therefore, in the following section we measured the $\langle Q \rangle(H_0, H_b)$ order parameter maps as a function of the amplitudes of H_0 and H_b while keeping the period of $H(t)$ constant for all our $Co_{1-x}Ru_x$ $(10\bar{1}0)$ - alloy thin films.

5.3 Dynamic phase transitions in the $\langle Q \rangle(H_0, H_b)$ phase space

Fig. 5.9(a) and Fig. 5.9(b) show the $\langle Q \rangle(H_0, H_b)$ phase space data for two periods of $P = 33.3$ ms and $P = 3.3$ ms, respectively, using once again the $Co_{0.76}Ru_{0.24}$ sample. In both phase diagrams, we observe a well-defined phase line at $H_b = 0$ that is associated with a first-order phase transition for H_0-values below a critical threshold H_{crit} (encircled by the solid line), where $\langle Q \rangle$ changes abruptly from red to blue, and which is qualitatively identical to the behavior that is present in the $\langle Q \rangle(P, H_b)$ phase space. Hence, for $H_0 >$

H_{crit} the system is in the dynamic paramagnetic state while for $H_0 < H_{crit}$ the system exhibits a dynamic ferromagnetic state. As P decreases (Fig.5.9(b)) H_{crit} moves to higher values of H_0 as expected and consistent with the behavior seen in Fig. 2.8 and Figs. 5.8 for the fast dynamic behavior. Furthermore, Figs. 5.9(a) and 5.9(b) demonstrate that the relevant phase space can still be accessed in a $H_0 - H_b$-type measurement, even if P changes by an order of magnitude, demonstration the experimental accessibility and robustness of this approach. Thus, given the advantages of exploring the $H_0 - H_b$- phase space, we now exploit this type of measurement to investigate the T/T_c dependence of the DPT and the surrounding phase space.

Nevertheless, we need to address the fact that in order to change T/T_c, we are actually changing samples in our approach, which could lead to unintended consequences, as the DPT point is not fully identical in different samples. However, it would also not be iden-

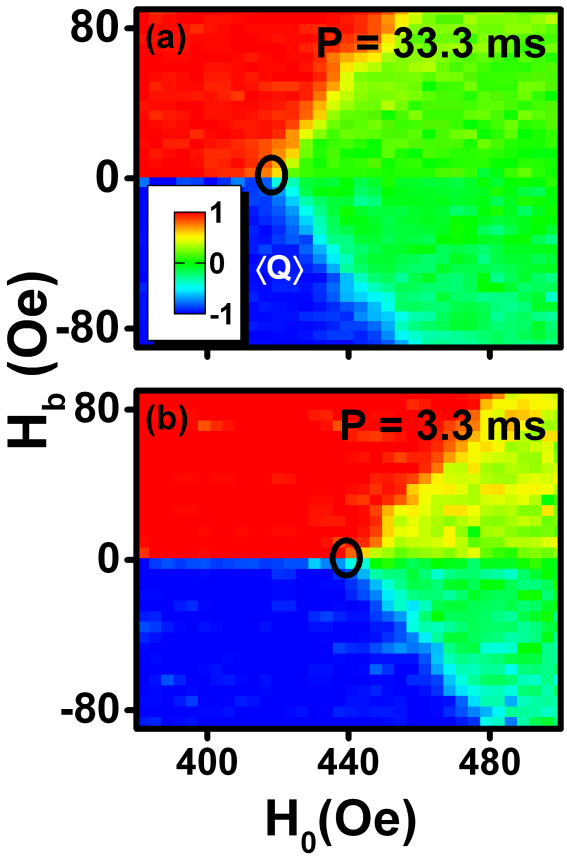

Figure 5.9: Experimental $\langle Q \rangle(H_0, H_b)$-data maps for (a) $P = 33.3$ ms Oe and (b) $P = 3.3$ ms, measured for the $Co_{0.76}Ru_{0.24}$ thin film. For all the measurements $H_{ref} = 580$ Oe and $380 \leq H_0 \leq 500$ ms. H_{crit} is represented by the black circle. The color scale bar applicable for $\langle Q \rangle$ is shown as an inset on the left-hand side of (a).

tical, if one were to use the same sample and vary T for the purpose of exploring the T/T_c dependence of DPT behavior. Usually, if one raises the temperature T of a magnetic system, its coercive field H_c reduces rather substantially, which is associated with the fact that in addition to larger thermal activation for higher T, the temperature induced decrease in M (supporting a magnetization reversal via the Zeeman energy term) is less than the temperature induced reduction in anisotropy energy (resisting a magnetization reversal) [60-62]. This means that if one were to conduct actual T dependent measurements of the dynamic magnetic behavior and the DPT, one would have to compensate a very significant H_c vs. T shift in the data analysis. In our sample series, H_c is fairly constant as x and thus T/T_c are changed, because with increased x also the low temperature saturation magnetization becomes much smaller, given the change in electronic structure associated with the changing compounds. Thus, magnetization and anisotropy changes with x nearly balance each other out, leading to an only weak H_c vs. x variations in our samples, which will aid our data analysis and reliability.

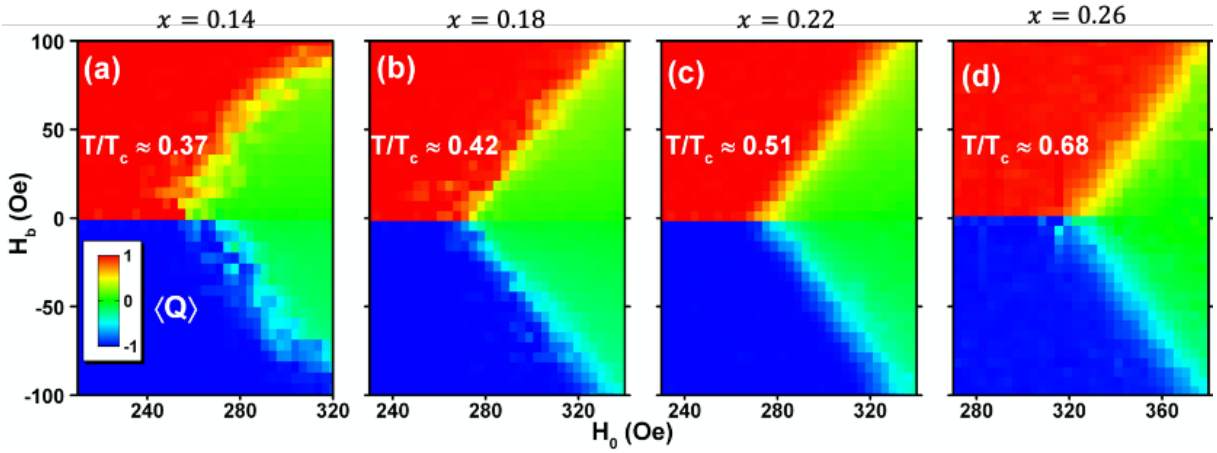

Figure 5.10: (a) – (d) Experimental phase space maps measured at $P = 3.3$ ms dynamic order parameter $\langle Q \rangle(H_0, H_b)$ for different $Co_{1-x}Ru_x$ thin films with $x = 0.14$, 0.18, 0.22 and 0.26, correspondingly representing different T/T_c ratios. Color scale bar for $\langle Q \rangle$ is located as inset on the left-hand side of (a).

Fig. 5.10 display $\langle Q \rangle(H_0, H_b)$ maps measured at a fixed $P = 3.3$ ms and different CoRu-alloy films representing 4 different T/T_c-ratios presented in each graphic. The corresponding color scale bar for all maps is located on the left-hand side of (a). H_{ref} was kept constant at 580 Oe in all measurements and a suitable H_0 – range was utilized to compensate the rather modest H_c increase associated with varying x. All of our

samples exhibit a saturation type behavior of the $M(t)$-oscillation amplitude for H_0 field amplitudes that are sufficiently larger than H_{crit}, reflecting the fact that above a saturation value for H_0 the sample magnetization reaches saturation in each and every half cycle of the applied field. Thus, a further increase of H_0 does not change the M vs. t trajectory in any meaningful way anymore and the $M(t)$-oscillation amplitude remains constant. In our experiments, we have chosen a H_{ref} value larger than the H_0 saturation value of all samples, so that the observed dynamic behavior becomes completely independent from H_{ref}.

Those figures show that independent from the T/T_c ratio, all samples show fundamentally a very similar behavior. Specifically, we find that below a certain critical value ($H_0 < H_{crit}$) there is a phase line at $H_b = 0$, which delimits two possible stable stables, either $\langle Q \rangle \approx +1$ (red) or $\langle Q \rangle \approx -1$ (blue) depending on the sign of H_b. Above H_{crit} this phase line is absent, and $\langle Q \rangle$ takes values that are close or equal to zero (green region). Thus, a dynamic phase transition takes place at H_{crit}, and this critical point delimits the ordered ($H_0 < H_{crit}$) from the disordered ($H_0 > H_{crit}$) state.

Additionally, in all the paramagnetic phases ($H_0 > H_{crit}$) that are visible in Fig. 5.10, there is a strong onset behavior in $\langle Q \rangle$ vs. H_b that would indicate a strong metamagnetic character of the PM phase occurring for all samples. This metamagnetic character specifically appears in sideband-like segments of the phase space, where there is a sudden change in $\langle Q \rangle$ with H_b. These changes are not abrupt and not hysteretic either. Thus, we observed a meta-magnetic like susceptibility increase without going through an actual phase transition. This behavior occurs only in the disordered regime. Hence, these results are analogous to those previously reported experimentally and theoretically for the $P - H_b$ phase space in the vicinity of the DPT [30, 31, 37].

A further examination of these metamagnetic tendencies was done by analyzing the fluctuation behavior of the order parameter, $\langle \sigma \rangle_Q = \sqrt{\langle Q^2 \rangle - \langle Q \rangle^2}$. Fig. 5.11 present color code maps for $\langle \sigma \rangle_Q$. Here, dark blue regions correspond to no or minimal fluctuations values, while the red-colored areas denote larger fluctuations of the order parameter Q. Thus, as expected in the FM state the order parameter is extremely stable and fluctuations are basically non-existent. Nevertheless, in the dynamic PM phase space areas, where the $\langle Q \rangle (H_0, H_b)$-data indicated a metamagnetic character, substantial fluctuation values appear, exhibiting a symmetric geometry with respect to the $H_b = 0$ line. Thus, the

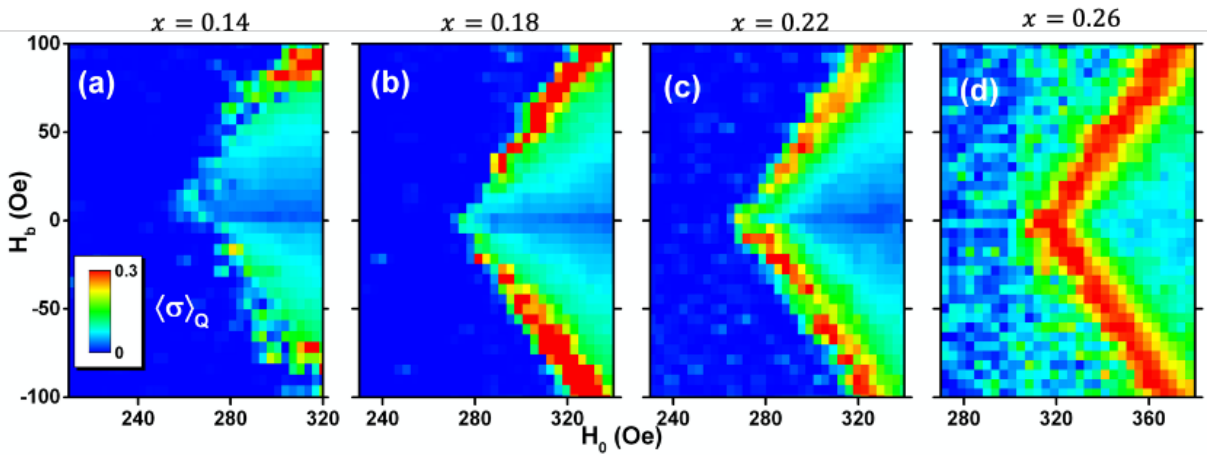

Figure 5.11: (a) – (d) Experimental fluctuations of the order parameter $\langle \sigma \rangle_Q (H_0, H_b)$ for different $Co_{1-x}Ru_x$ thin films with $x = 0.14$, 0.18, 0.22 and 0.26, correspondingly representing different T/T_c ratios. Color scale bar for $\langle \sigma \rangle_Q$ is located as inset on the left-hand side of (a).

metamagnetic fluctuations reported previously for Co-films can be regarded as a general phenomenon of the paramagnetic phase, independent from the T/T_c ratio. Furthermore, we observe that as the T/T_c ratio increases an enhancement of the these metamagnetic fluctuations occurs as shown by Figs. 5.11(a) – (d). In fact, high fluctuation values occur even closer to the critical point, for higher T/T_c ratios. So, for the highest T/T_c sample, the critical fluctuations at H_{crit}(and $H_b = 0$) and the metamagnetic fluctuations in the PM state actually coalesce, which they do not do for the other samples. This result is not surprising, as fluctuations, in general, should increase as one brings a magnetic system closer to its critical temperature.

It should also be mentioned that at the highest T/T_c ratio (≈ 0.68) traces of $\langle \sigma \rangle_Q \neq 0$ can be detected even in the FM region (Fig. 5.11(d)). However, this is related to the fact that the magneto-optical response of the samples decreases considerably as we reach higher T/T_c ratios. This leads to a lower magneto-optical signal amplitude ($\Delta I/I$), which makes the data noisier and hence more susceptible to exhibiting small fluctuation values within our current phase space, a fact that are not driven by the magnetization dynamics itself.

A quantitative analysis of the metamagnetic fluctuations shown in Fig. 5.11, was done by analyzing the probability density associated with $\langle \sigma \rangle_Q$ values in a specified normalized window between the ranges H_0/H_{crit} (0.85 to 1.15) and H_b/H_{crit} (-0.35 to 0.35). Hence, histogram plots were used to visualize the relative significance of sufficiently large fluctu-

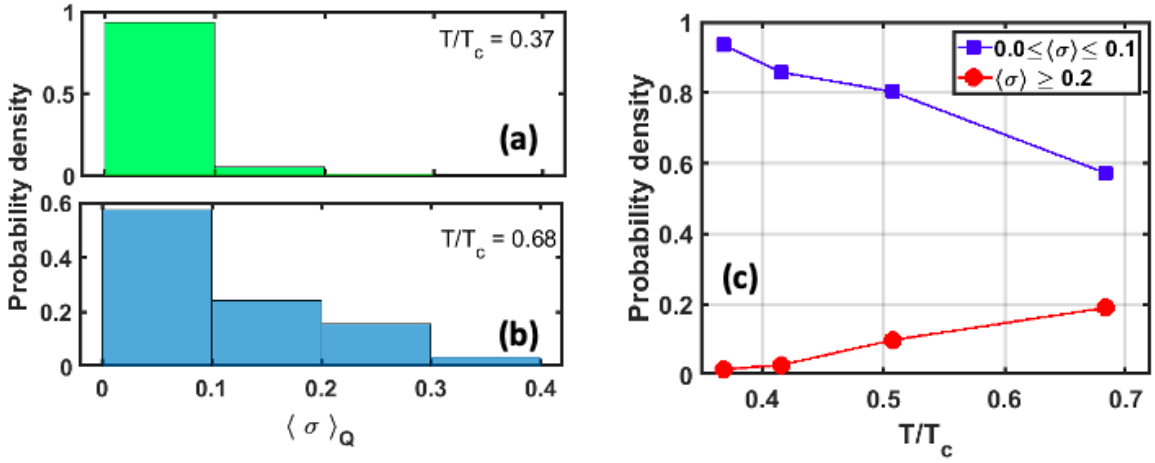

Figure 5.12: Probability density histogram for the fluctuations (a) at $T/T_c = 0.37$ ($x \approx 0.14$) and (b) $T/T_c \approx 0.68$ ($x = 0.26$); (c) probability density values vs. T/T_c for $0.0 \leq \langle\sigma\rangle_Q \leq 0.1$ (blue squares) and $\langle\sigma\rangle_Q \geq 0.2$ (red circles). The lines are guide for the eyes.

ations in the selected phase-space. The probability density representing our lowest T/T_c ratio (≈ 0.37) sample is shown in Fig. 5.12(a) in comparison to the data for the highest T/T_c ratio (≈ 0.68). It is noticeable that almost all existing fluctuations are rather weak ($0.0 \leq \langle\sigma\rangle_Q \leq 0.1$) for the lowest T/T_c ratio. Thus, the probability for $0.0 \leq \langle\sigma\rangle_Q \leq 0.1$ is almost equal to 1 and only very few larger fluctuations ($\langle\sigma\rangle_Q > 0.1$) are recorded throughout the phase space. This is in agreement with previous results obtained for pure Co thin films, which represent an even lower T/T_c value than reported here. As the measurement temperature gets closer to T_c, a broader distribution of probability arises, as seen in Fig. 5.12(b). This fact is not related to the detection noise, previously mentioned in conjunction with Fig. 5.11(h) because this noise actually leads to small fluctuations values only. Instead, the broadened distribution in Fig. 5.12(b) denotes a real dynamic state effect occurring for higher T/T_c values, namely that there is a larger portion of the phase space, in which large fluctuations are present. Hence, the metamagnetic tendencies in the dynamic paramagnetic state are enhanced as the systems get closer to T_c.

This fact is even more noticeable in Fig. 5.12(c), where we compared the probability to be either in a low fluctuation state $0.0 \leq \langle\sigma\rangle_Q \leq 0.1$ or a high fluctuation ($\langle\sigma\rangle_Q \geq 0.2$) state. Here, we observe that when the T/T_c ratio is low, the corresponding probability to have lower fluctuation values is high (blue squares) in contrast to higher fluctuation state (red dots).

As T/T_c increases, the dynamic states in the system are characterized by larger fluc-

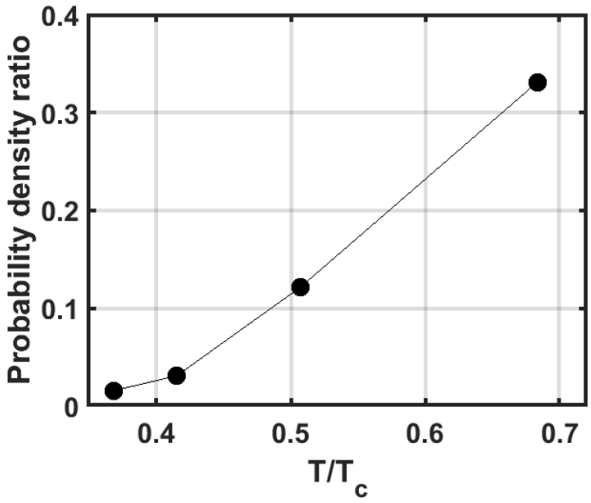

Figure 5.13: Probability density ratio $P_{high}(\langle\sigma\rangle_Q \geq 0.2)/P_{low}(0.0 \leq \langle\sigma\rangle_Q \leq 0.1)$ *evolution vs.* T/T_c *for the* $Co_{1-x}Ru_x$ *thin film samples. The black line is a guide for the eyes.*

tuation, that are specifically associated with the metamagnetic character of the dynamic paramagnetic state. To visualize this fact very clearly, Fig. 5.13 shows the probability ratio $P_{high}(\langle\sigma\rangle_Q \geq 0.2)/P_{low}(0.0 \leq \langle\sigma\rangle_Q \leq 0.1)$, which shows a strong monotonous increase with T/T_c that represents an enhancement of large metamagnetic fluctuations by a factor of almost 22 as the T/T_c ratio doubles its value. Therefore, our experiments demonstrate that the occurrence and extent of metamagnetic fluctuations is massively enhanced by increasing T/T_c of the dynamic magnetic system.

Chapter 6

Dynamic phase transitions using a mean field approach

This chapter discusses some basic aspects about the mean field approach for magnetic systems and its application to study dynamic phase transitions. Using this approach, we have solved numerically the DPT's master equation to treat the dynamic order parameter evolution in terms of the reduced temperature (T/T_c), the field amplitude H_0 and period P, as well as, the applied bias field H_b. Therefore, in section 6.4 we present some color coded based maps representing the numerical solutions for $Q(H_0, H_b)$ and its corresponding dynamic susceptibility, $\chi_Q(H_0, H_b)$.

6.1 Mean field theory

Let us introduce the Ising Hamiltonian which was briefly presented previously in chapter 2,

$$\mathcal{H} = -\frac{\mathcal{J}}{N}\sum_{[i,j]}^{N} S_i S_j + H\sum_{i}^{N} S_i \ . \tag{6.1}$$

The first term represents the exchange energy of the spin system with $\mathcal{J} > 0$ being the ferromagnetic exchange coupling constant and S_i the Ising spin at location i, which can take only two possible values ± 1. The sum $\sum_{[i,j]}$ runs over all exchange coupled sites (N). The second term corresponds to the Zeeman energy associated with an external magnetic field that is spatially uniform for all spins sites i.

Even though, this model has exact solutions for 1-dim and 2-dim lattices, approximation based methods can help us to understand some of the most basic and underlying

physics behind the spin interactions without making any high performance calculations. Likewise, these approximation can be regarded as a first approach in trying to construct a theory.

One of the most common approximations used to solve the Ising Hamiltonian corresponds to that of the *Weiss molecular field* or *mean field* theory. Essentially, the mean field approximation (MFA) neglect spin fluctuations around the mean, thus the system's thermal fluctuations are relatively small and can therefore be neglected to a certain extent. Therefore, a single spin at position i will "feel" an *effective field* h_{eff} from its neighbor spins $z = 2d$, where z is the number of nearest neighbors and d corresponds to the lattice's dimension.

Now, we need to identify our magnetic order parameter which distinguishes the ordered (magnetic) from the disordered (nonmagnetic) phase, which is no other than the system's local magnetization m. The ferromagnetic phase (ordered) has an $m \neq 0$ while the paramagnetic phase (disordered) is characterized by $m \approx 0$. Hence,

$$m = \langle S_i \rangle \ . \tag{6.2}$$

We have already indicated that under the MFA fluctuations are rather small $\delta S_i = S_i - \langle S_i \rangle$, thus we can approximately determine $S_i S_j$,

$$\begin{aligned} S_i S_j &= \langle S_i \rangle \langle S_j \rangle + \langle S_j \rangle \delta S_i + \langle S_i \rangle \delta S_j \\ &= \langle S_i \rangle S_j + \langle S_j \rangle S_i + \langle S_i \rangle \langle S_j \rangle \\ &= m(S_i + S_j) - m^2 \ . \end{aligned} \tag{6.3}$$

Therefore, the Ising Hamiltonian (Eq. 6.1) can be written as:

$$\mathcal{H}_{MFA} = -m \frac{\mathcal{J}}{N} \sum_{[i,j]}^{N} (S_i + S_j - m) + H \sum_{i}^{N} S_i \ . \tag{6.4}$$

Now, by neglecting the fluctuations and doing some basic calculations[1], the Mean Field Hamiltonian reads,

$$\mathcal{H}_{MFA} = \frac{1}{2} z \mathcal{J} m^2 - h_{eff} \sum_{i}^{N} S_i \ . \tag{6.5}$$

where h_{eff} is the effective magnetic field experienced by the spins,

$$h_{eff} = H + z\mathcal{J}m \ . \tag{6.6}$$

[1]Further details can be found in references [41, 163]

Our "new" Hamiltonian implies that our spins will no longer interact with each other, but rather interact via an effective field which corresponds to the external field H coupled with the in-situ mean field induced by the neighboring spins ($z\mathcal{J}m$).

Finally, let us find the total magnetization of the system by using the mean field partition function,

$$\mathcal{Z}_{MFA} = Tr(e^{-\beta\mathcal{H}_{MFA}}) \tag{6.7}$$

where $\beta = 1/k_BT$. Recalling that the total magnetization of the system is given by,

$$m = \frac{1}{N}\sum_{i}^{N}\langle S_i\rangle \tag{6.8}$$

we reach the self-consistency equation,

$$\begin{aligned} m &= \tanh\left[\beta h_{eff}\right] \\ &= \tanh\left[\beta(H + z\mathcal{J}m)\right] \ , \end{aligned} \tag{6.9}$$

which is a transcendental equation. From Eq. 6.9 we can determine the critical temperature T_c at which the system becomes spontaneously magnetized without any external magnetic fields. Thus, by setting $H = 0$ we have that T_c is given by,

$$T_c = \frac{z\mathcal{J}}{k_B} \tag{6.10}$$

Therefore for $d = 2$ ($z = 4$) we have that $k_BT_c = 4\mathcal{J}$. However, an exact solution for the 2-d system leads to $k_BT_c = \dfrac{2}{ln(1+\sqrt{2})}\mathcal{J}$ [11].

6.1.1 Mean field theory applied to dynamic phase transitions

In our last section we derive an equation for the behavior of the magnetization under the action of a static external field H. Nevertheless, dynamic phase transitions involve the presences of a time-dependent field $H(t)$. Following the seminal work by Tomé and Oliveira [23] where they derived a time series equation for the kinetic Ising Hamiltonian (Eq. 2.22), we have that the master equation for a dynamic system evolving according to the Glauber stochastic process reads [80],

$$\tau\frac{d}{dt}\langle S_i\rangle = -\langle S_i\rangle + \tanh\left\{\beta\left[z\mathcal{J}\langle S_i\rangle + H(t)\right]\right\} \ . \tag{6.11}$$

In the thermodynamic limit $N \to \infty$, $\langle S_i\rangle \to m$, so

$$\tau\frac{dm}{dt} = -m + \tanh\left\{\beta\left[z\mathcal{J}m + H(t)\right]\right\} \ . \tag{6.12}$$

Within DPT the external magnetic can be regarded as the sum of a time t-dependent periodic field and a constant bias field H_b,

$$H(t) = H_0 \cos \omega t + H_b \ , \tag{6.13}$$

Thus, the equation of motion for the average magnetization m normalized to the saturation magnetization is given by [26],

$$\tau \frac{dm}{dt} = -m + \tanh \left\{ \frac{1}{T} \left[m + \frac{H_b}{\mathcal{J}} + \frac{H_0}{\mathcal{J}} \cos(\omega t) \right] \right\} \ . \tag{6.14}$$

where T is the temperature normalized to $k_B T_C$.

6.2 Numerical solution for DPT within MFA

Therefore, to obtained the steady state solution for our dynamic phase transition problem, we have solved numerically Eq. 6.14 for different H_0, H_b, $\omega(P)$ and T, in a two dimensional lattice, i.e. $z = 4$. For our purposes we have used the **odeint** (ordinary differential equation integration) library [164]. Then, our numerical model was developed using *python* and its **scipy.integrate.odeint** package [165].

The number of applied field values per oscillation cycle, was set to 1000, which was probed to be more than enough to ensure that the critical exponents are always identical independent of this step size. The initial condition for $m_0(t)$ was equal to,

$$m_0(t = 0) = \pm 0.15 + 0.4 \cos(\omega t) \ , \tag{6.15}$$

where $\omega = 2\pi/P$ was set to be in phase with $H(t)$ and a constant term either positive or negative depending on the applied bias field sign [25, 26]. After this first full-cycle iteration ($n = 0$), the next one ($n = 1$) takes as the initial condition the last known value for $m_0(t)$ ($m_0(t = 1000)$). To determine if whether the system has reached a steady state solution or not after n full-cycle iterations ($n \times t$) we have chosen a cut-off parameter, namely $L(m)$,

$$L(m) = |m_{n+1}(t) - m_n(t)| < 10^{-10} \ , \tag{6.16}$$

meaning that the maximum error allowed for two consecutive cycles should be lower than 10^{-10} so that the solution can be accepted for the initial parameters.

Lastly, our known observables are the dynamic order parameter Q, which remains as the mean value for $m(t)$ after each full-cycle iteration. Thus,

$$Q = \frac{1}{n}\sum_{t=1}^{n} m(t)\ . \tag{6.17}$$

Likewise, as the MFA does not take into account fluctuations we have determined the dynamic susceptibility as well, namely,

$$\chi_Q = \frac{dQ}{dH_b}\ . \tag{6.18}$$

6.3 Dynamic order parameter evolution

Fig. 6.1 shows the numerical results from our MFA approach to determine the evolution of a ferromagnetic system under the influence of a time-dependent field (blue dotted line)

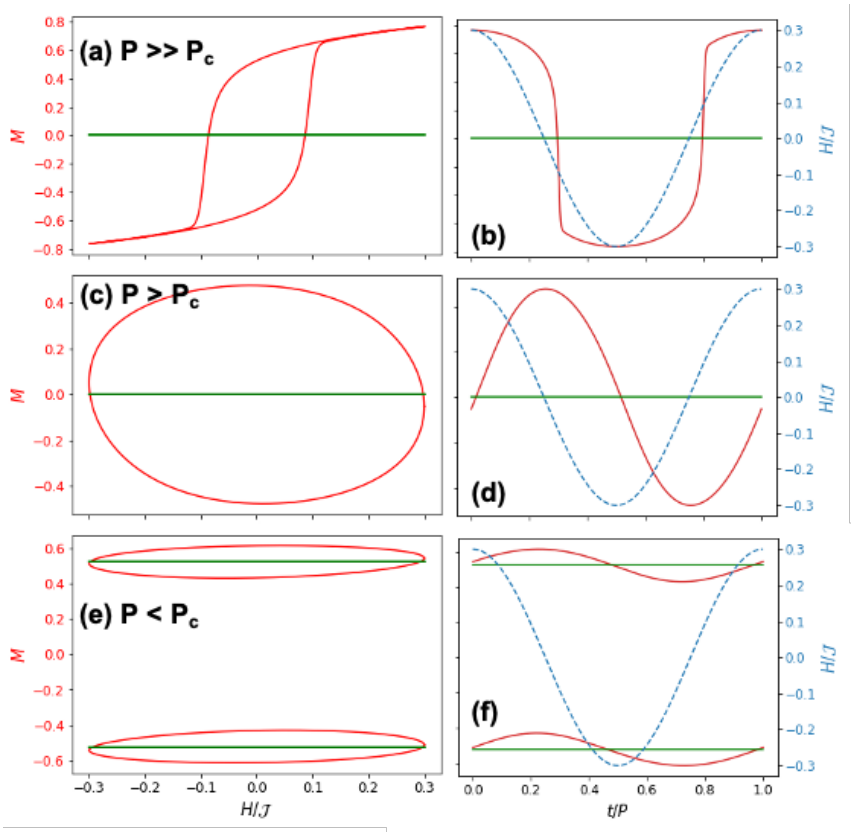

Figure 6.1: Left column: (a), (c), (e): M vs. H hysteresis loops for different values for different periods. The red line corresponds to the numerical magnetization values. Right column: (b), (d), (f): corresponding M vs. t curves in red lines (left axis) and H vs. t curves in dashed dotted blue lines (right axis). The horizontal green line indicates the dynamic order parameter Q

as its period is changed. The red lines corresponds to the magnetization values retrieved using a fixed temperature $T/T_c = 0.8$, constant field amplitude $H_0/\mathcal{J} = 0.3$ and no bias field $H_b/\mathcal{J} = 0$. For $P \gg P_c$ (Fig. 6.1(b)) we have that M vs H has a hysteresis-like behavior, where the magnetization nearly follows the external magnetic field with a rather small delay (Fig. 6.1(b)) oscillating around the zero Q value, as expected for larger P. As the external's field period reduces the magnetization keeps on lagging behind the field, as seen on Fig. 6.1(d). Thus, M vs H curve gets distorted but Q remains equal to zero. Nevertheless, when $P < P_c$ there is a symmetry breaking leading to that the center of the M vs. H hysteresis loop is vertically shifted away from an $M = 0$ center [29, 37, 39]. Thus, the system collapses changing the dynamic order parameter to values different from zero 6.1(f). This results are somehow expected and were previously discussed, yet by performing these calculations we were able to determine the validation of our model.

Using the mean field approach we have determined the behavior of the bulk's critical period P_c as function of the external field's amplitude, H_0. Fig. 6.2(a) shows the evolution of the dynamic order parameter Q for a fixed H_0 amplitude and changing field period at a constant temperature ($T = 0.8T_c$). We can observe that the dynamic order parameter

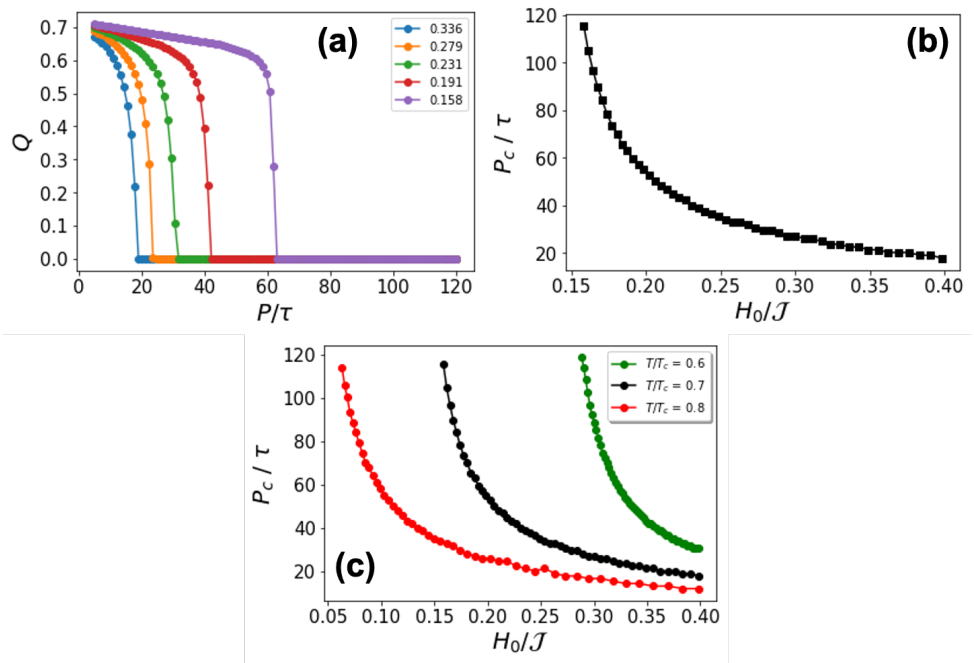

Figure 6.2: (a) Dynamic order parameter evolution as function P for different field amplitudes, H_0. The region where the Q changes from zero to non-zero values is the so-called critical period, P_c (b) P_c vs H_0 characteristic behavior. Both (a) and (b) were determined for a fixed temperature ratio $T/T_c = 0.7$. (c) P_c vs H_0 curves for different T/T_c ratios.

changes continuously from from $Q = 0$ to $Q \neq 0$ at P_c, where P_c increases as H_0 decreases. Fig. 6.2(b) presents the evolution of P_c with H_0, we can conclude that low H_0 values yield high values of P_c, namely, slow critical dynamics. On the contrary, large H_0 values lead to fast critical dynamics [37]. As we are more interested in the dynamic behavior in terms of different reduced temperature T/T_c values, we have determined the behavior of P_c as function of T/T_c. From Fig. 6.2(c) it is evident that as T/T_c decreases the field values interval at which we have a dynamical phase transition have to increase. This is because, as the system's magnetization becomes larger as we are far from the critical temperature, we need to add more Zeeman energy to the system to induce our dynamic phase transition. Therefore, we have that the dynamic phase transition is characterized as well by a critical field value H_{crit} which highly depends on the temperature at which the system is subjected to.

To give further illustration about the effects of the time-dependent amplitude H_0 in the dynamic phase space, we have performed the numerical simulations presented in Fig. 6.3. The dynamic order parameter evolution in terms of the field amplitude is shown in Fig. 6.3(a) for different T/T_c ratios. The region where the Q changes from zero to

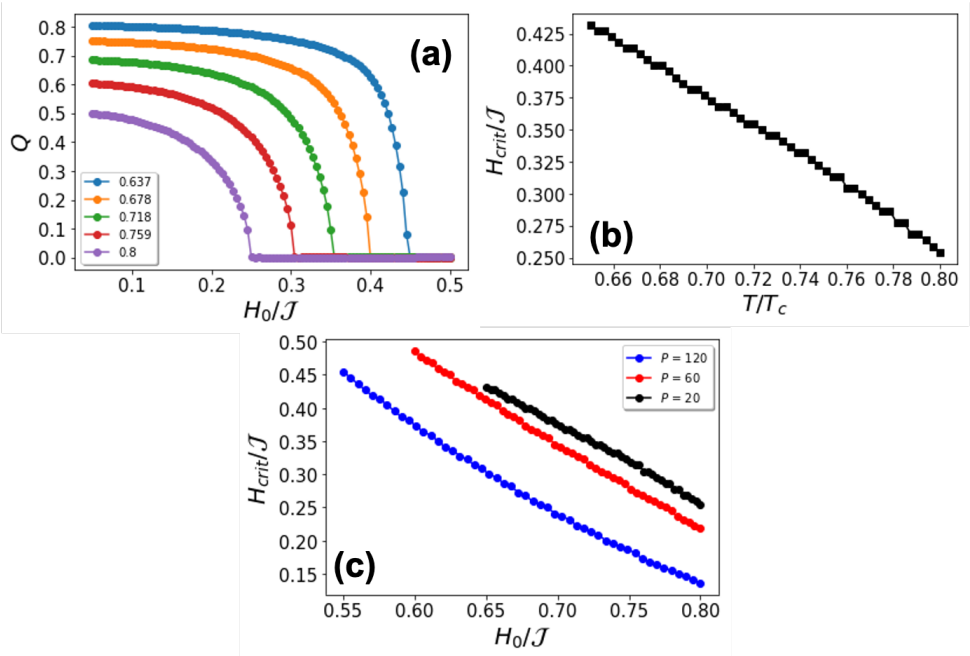

Figure 6.3: (a) Dynamic order parameter evolution as function of H_0 period for different temperature ratios, T/T_c. The region where the Q changes from zero to non-zero values is critical field, namely H_{crit}. (b) T/T_c vs H_{crit} characteristic behavior. Both (a) and (b) were determined at a fixed period $P = 20$. (c) H_{crit} vs H_0 curves for different P.

non-zero values is the so-called critical field, H_{crit}. It is evident that at H_{crit} the system undergoes a second order phase transition as Q changes in a continuous fashion, this behavior resembles the one for P vs Q. It is evident that as the temperature of the system decreases the critical field values increases in almost a linear trend. This fact is clearly depicted in Fig. 6.3(b), where for a fixed period ($P = 20$), we have that H_{crit} increases inversely with T/T_c. When the period at which the time dependent field is applied to the system changes, we have that the overall behavior for H_{crit} vs H_0 remains nearly the same. Nevertheless, we have a significant difference in between the slow (low P values) and fast regime (high P values), for $P = 120$ we have lower H_{crit} values in comparison to the ones for $P = 20$ or $P = 60$, which are almost equivalent with only small deviations. This results are rather similar to the ones already exhibited for our experimental measurements (Fig. 5.9) in the $\langle Q \rangle(H_0, H_b)$ phase space.

Following this numerical analysis in companion with our early experimental results one can conclude undoubtedly that the dynamic phase space can be explored using two different approaches. For fine details near P_c it is more straightforward to use the classical $\langle Q \rangle(P, H_b)$ phase maps. However, for a wider inspection of the dynamic phase space it is better to use the $\langle Q \rangle(H_0, H_b)$ phase maps when changing T/T_c, as even small changes in H_0 imply variations in the critical field; whereas to reach the same variations in terms of the period one has to change several decades which is fairly difficult experimentally.

6.4 Numerical $Q(H_0, H_b)$ and $\chi_Q(H_0, H_b)$ phase maps for different T/T_c ratios

To analyze the behavior of the dynamic order parameter and the dynamic susceptibility for different T/T_c ratios we have performed numerical simulations using the MFA in the dynamic phase space associated with H_0 vs H_b. Fig. 6.4(a)-(b) shows the corresponding $Q(H_0, H_b)$ phase map at a fixed temperature ($T/T_c = 0.7$) and different field periods, $P = 20$ and $P = 120$ correspondingly. The color-coded bar related to Q is shown at the left of each graph. The yellow area corresponds to values of $Q \approx +1$, whereas the blue area is associated with $Q \approx -1$. The light red area is then linked to $Q \approx 0$ which is the so-called paramagnetic disordered phase. As expected H_{crit} becomes smaller when the period increases. Furthermore, independent of P we identify that the system exhibit

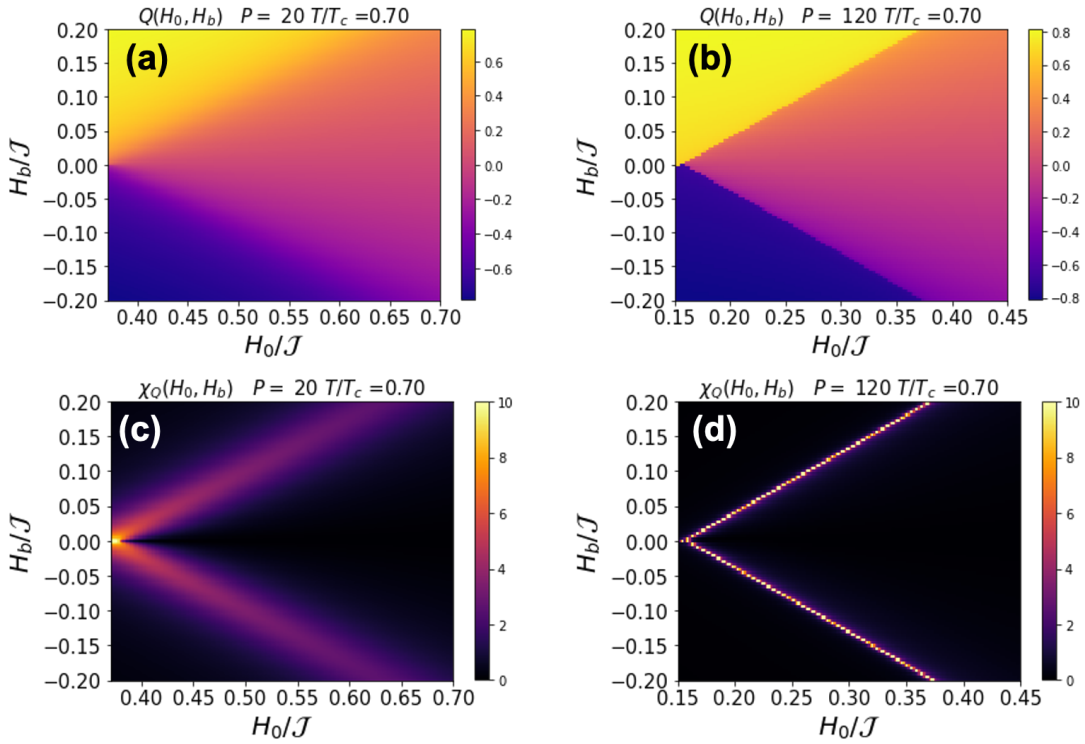

Figure 6.4: Color-coded maps representing the numerical data in the H_0 vs H_b phase space at a fixed $T/T_c = 0.7$. (a) and (b) show Q for $P = 20$ and $P = 120$ respectively, while (c) and (d) presents their related dynamic susceptibility χ_Q. The color-coded bars for each observable are shown at the right of each figure.

sideband behavior. However as the period increases the metamagnetic behavior becomes even sharper, with a transition in between low Q values to larger $|Q|$ values in a small window of bias fields. To examine this behavior, the dynamic susceptibility $\chi_Q(H_0, H_b)$ was determined and plotted in Fig. 6.4(c)-(d). The darker area corresponds to none or low fluctuations of the dynamic order parameter, while the violet-to-yellow lines correspond to the transition limits between χ_Q values different from zero up to the maximum fluctuation values $\chi_Q = 10$ (yellow). The region where the sidebands coalesce is H_{crit}, which has the larger fluctuation values and determines the limit in between the ordered to the disordered dynamic phase. These phase maps are in agreement with the ones obtained experimentally, thus we clearly verify that there is a clear metamagnetic-like behavior under our simulated conditions that resemble the experimental conditions. Likewise, as evidenced previously in the $Q(H_0, H_b)$ phase maps, the anomalous fluctuations are sharper for larger period values. Thus, we have that for the slow dynamic regime the metamagnetic behavior of the system is enhanced (Fig. 6.4(d)) whereas for fast dynamics

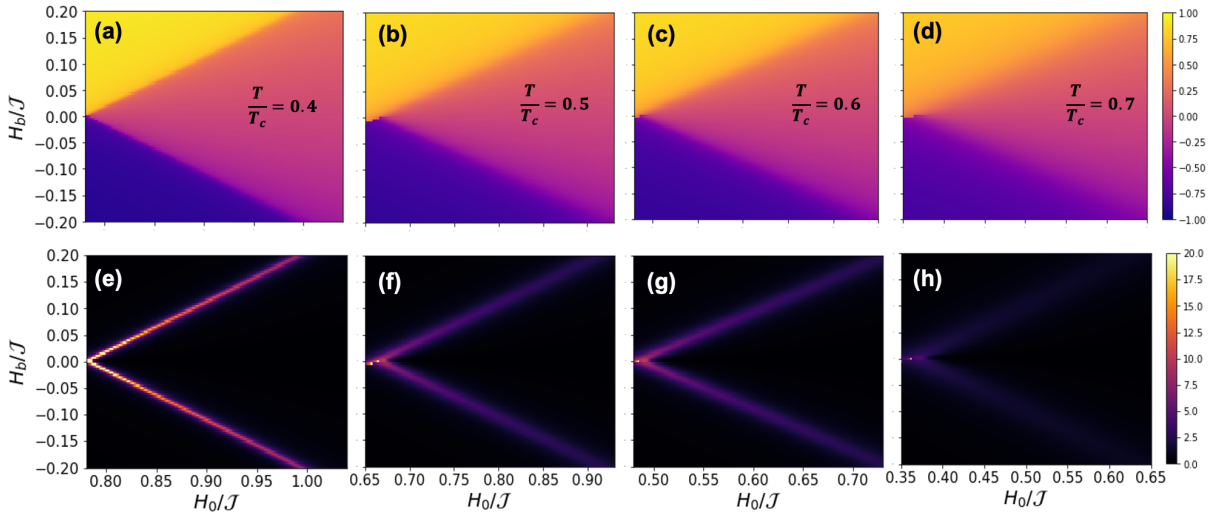

Figure 6.5: Color-coded maps representing the MFA numerical data at a fixed $P = 20$. (a) - (d) $Q(H_0, H_b)$ phase space maps for $T/T_c = 0.4, 0.5, 0.6$ and 0.7 as indicated in the figures. Their corresponding dynamic susceptibility $\chi_Q(H_0, H_b)$ is depicted in (e)-(h). The color-coded bars for $Q(H_0, H_b)$ and $\chi_Q(H_0, H_b)$ are shown on the right of (d) and (h), respectively, and apply for all color maps within each row.

it is a more gradual one, as the sidebands cover a larger area in the phase space, Fig. 6.4(c).

Finally, to explore the role of the reduced temperature T/T_c in the dynamic $Q(H_0, H_b)$ phase space we have performed further calculations using the MFA. Figs. 6.5(a)-(d) shows the $Q(H_0, H_b)$ phase maps at $P = 20$ (fast dynamics regime) for $T/T_c = 0.4, 0.5, 0.6$ and 0.7 respectively. These temperatures where chosen in order to resemble the ones from our experimental thin films. In accordance to our prior experimental results, we can determine that independent of the critical temperature of the system the phase maps exhibit the same features, with a clear distinction between the paramagnetic region $Q \approx 0$ and the dynamic ferromagnetic phase $Q \approx \pm 1$ at the H_{crit}. Likewise, as shown in Fig. 6.3(a) we have that H_{crit} increases as we move on to a lower temperature regime, which is expected as the system needs a higher Zeeman energy to invert the sign of the magnetization. Furthermore, we have calculated the corresponding dynamical susceptibility phase maps $\chi_Q(H_0, H_b)$ as can be seen on Figs. 6.5(e)-(h). It is important to notice that the anomalous fluctuations which are an important feature of dynamics phase transitions are still present for all the temperatures considered in our calculations and they coalesce in a single critical point. Nevertheless, as the system's temperature approaches T_c, i.e.,

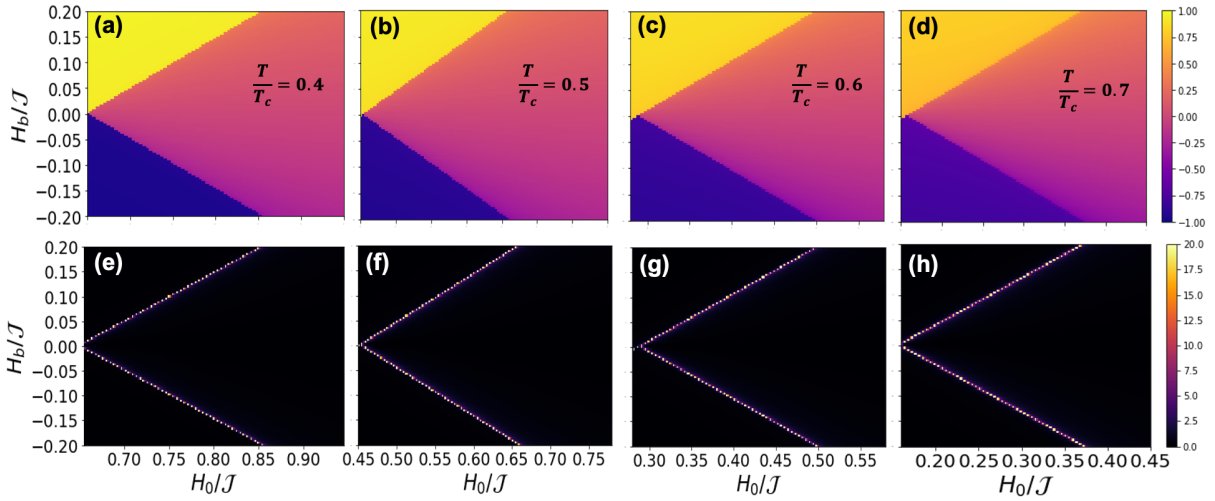

Figure 6.6: Color-coded maps representing the MFA numerical data at a fixed $P = 120$. (a) - (d) $Q(H_0, H_b)$ phase space maps for $T/T_c = 0.4, 0.5, 0.6$ and 0.7 as indicated in the figures. Their corresponding dynamic susceptibility $\chi_Q(H_0, H_b)$ is depicted in (e)-(h). The color-coded bars for $Q(H_0, H_b)$ and $\chi_Q(H_0, H_b)$ are shown on the right of (d) and (h), respectively, and apply for all color maps within each row.

$T/T_c = 1$ the sidebands gradually fade away diminishing their intensity. These last results are somehow quite different to the ones reached by experimental means, where the fluctuations where enhanced by increasing T/T_c. However, it is important to recall that within the MFA we do not take into account the spin's fluctuations and also the reduced magneto-optical signal related to the diminution of the magnetization in the thin films.

Our experimental setup only had access to information in the slow dynamic regime. Therefore, we have performed further calculation in this regime. Fig. 6.6(a)-(d) shows the color coded dynamic phase maps for $Q(H_0, H_b)$ using a $P = 120$ for different temperature ratios (described in each graph). These $Q(H_0, H_b)$ resemble those obtained in the fast dynamic regime, with a clear distinction between the ordered ($Q \sim 1$) and disordered phase ($Q \sim 0$). However, an inspection of their corresponding dynamic susceptibility $\chi_Q(H_0, H_b)$ phase maps (6.6(e)-(h)), shows that while the metamagnetic fluctuations are present independent of the temperature ratio, their intensity is not affected as the system gets closer to T_c, contrary to the results reached in the fast dynamic regime. This is expected as the metamagnetic anomalies are enhanced by the inverse logarithm of the field oscillation period [30].

Overall our MFA calculations demonstrate that independent of the temperature the

$Q(H_0, H_b)$ and $\chi_Q(H_0, H_b)$ dynamic phase maps can be used to study DPT in the proximity of T_c. Certainly, additional studies must be performed using Monte Carlo (MC) simulations which include thermal fluctuations and/or effective-field theory to broaden the discussion around DPT's for different T/T_c.

Chapter 7

Conclusions and outlook

In this work, we have conducted a comprehensive experimental study of dynamic magnetic states in the phase space surrounding the DPT as a function of the T/T_c ratio. For that purpose, we have fabricated a suitable set o thin film samples that exhibit different T_c, so that the T/T_c ratio could be varied in our experimental study while keeping the measurement temperature T constant at room temperature, allowing us to take full advantage of our ultrasensitive T-MOKE tool.

Therefore, we have fabricated $Co_{1-x}Ru_x$ $(10\bar{1}0)$ $(0.0 \leq x \leq 0.26)$ thin film samples using co-sputter deposition at room temperature in a pure Ar as a sputter gas. The overall growth sequence was as follows: an HF-etched Si(110) substrate/ 37.5nm Ag (110)/ 10nm Cr (220)/ 20nm $Co_{1-x}Ru_x$ $(10\bar{1}0)$ and on top of it a 10 nm SiO_2 overcoat, which was deposited to avoid oxidation and contamination.

Sample's crystallographic analysis showed that independent of the Ru doping concentration, all of our films have similar crystal quality and are epitaxial with a high orientation behavior that has the *c*-axis of the *hcp* crystal structure in the plane of the surface. Furthermore, static magnetization measurements revealed that all the samples are ferromagnetic at room temperature, exhibit uniaxial anisotropy, and show a sharp magnetization reversal at the coercive field ($\pm H_c$) if the magnetic field is applied along the easy magnetization axis. Likewise, for most of the samples H_c is equal to the switching field, H_{sw}. Additionally, the samples have a T_c that depends on the Ru concentration and not on the structural properties of the system. Thus, our thin films are suitable to experimentally explore DPT and the existence of metamagnetic fluctuations in the proximity of DPT for materials with different T/T_c ratios.

The experimental detection of the dynamic order parameter Q was done in two different phase spaces, $P-H_b$ and H_0-H_b; using an ultrasensitive T-MOKE setup. In addition to the T-MOKE, to minimize field fluctuations for H_0 and H_b, an iterative routine was implemented. This guarantees that $H(t)$ is stable throughout the entire measurement process. Thus in all our experiments, for $H(t)$ periods in the region of 3.3 ms up to 33.3 ms, we have achieved field amplitude deviations of less than ± 1 Oe for H_0 amplitudes up to 600 Oe and bias field variations less than ± 0.4 Oe, for all the values of H_0 and H_b that we utilized in this study.

Therefore, we measured the corresponding $\langle Q \rangle (P, H_b)$ maps. These maps show metamagnetic like behavior for all T/T_c ratios, just like previously reported for Co thin films. Hence, as the amplitude of H_0 changes so does the critical period P_c. This H_0 sensitivity of P_c is rather strong, while the P dependence of the dynamic behavior is comparatively weaker. Thus, P dependent measurements are primarily suitable to investigate fine details near the DPT.

However, our primary goal was to study larger portions of the dynamic phase space, so that instead of P-dependent measurements, we pursued our phase space exploration of the dynamic magnetic behavior as function of H_0 and H_b. Consequently, $\langle Q \rangle (H_0, H_b)$ maps were measured in a wider phase space region and as function of T/T_c for all of our $Co_{1-x}Ru_x$ $(10\bar{1}0)$ $(0.0 \leq x \leq 0.26)$ thin film samples.

Then, independent of T/T_c, all of our $\langle Q \rangle (H_0, H_b)$ phase maps exhibit the same main qualitative features of the dynamic phase transition, where likewise to P_c at a unique critical field H_{crit}, a DPT takes place, which then separates the ordered FM dynamic regime from the disordered PM one. Furthermore, the metamagnetic fluctuations reported previously for magnetic thin films near the DPT are observed to be a general phenomenon, which occurs in the paramagnetic dynamic phase. A close inspection of the metamagnetic tendencies in the disordered PM regime, done by analyzing the fluctuation behavior of the order parameter $\langle \sigma \rangle_Q$, shows that significantly larger fluctuation values tend to appear as T/T_c increases, as seen in Figs. 5.11(a) – (d). Thus, high fluctuation values occur even closer to the critical point for sufficiently high T/T_c ratios, as the metamagnetic fluctuation regime merges with the critical point, while this does not happen for low T/T_c values. A further analysis of the phase space probability density for $\langle \sigma \rangle_Q$ shows that the occurrence of large fluctuation is becoming ever more likely with increasing T/T_c.

The numerical simulations using the mean field approach showed that as revealed from the experimental data, the metamagnetic fluctuations are still present in the dynamic phase space independent of the temperature. Nevertheless, as the MFA does not take into account the spin fluctuations leads to that the dynamic susceptibility sidebands present in the PM phase tend to gradually fade away diminishing their intensity as T/T_c increases in the fast dynamic regime, which is contrary to the experimental results. However, in the slow dynamic regime there is not any relevant changes in the intensity of the dynamic susceptibility. Though, additional studies must be performed using Monte Carlo (MC) simulations which include thermal fluctuations and/or effective-field theory to broaden the discussion around DPT's in the new $Q(H_0, H_b)$ phase space.

We hope that our work stimulates further experimental and theoretical studies of DPTs and their surrounding phase spaces by using the $\langle Q \rangle (H_0, H_b))$ phase maps, which facilitate a wider inspection of the dynamic phase space behavior. Likewise, it would be interesting to develop an in-depth understanding of the importance of T/T_c ratios in general and specifically with respect to metamagnetic fluctuations, their size, their distribution and their possible coalesce with the critical point.

Finally, it would be more than interesting to experimentally and theoretically examine the vector nature of magnetization and thus the potential relevance of the dynamic order parameter Q being a vector quantity, which has been ignored so far for DPTs. Experimentally, this is more than plausible with the help of our experimental approach to detect DPTs using the ultrasensitive T-MOKE with high field fidelity and stability.

List of publications

Work related to this thesis:

- **J.M. Marín Ramírez**, E. Oblak, P. Riego, G.E. Campillo, J. Osorio, O. Arnache and A. Berger. *Experimental exploration of dynamic phase transitions and associated metamagnetic fluctuations for materials with different Curie temperatures.* Phys. Rev. E **102**, 022804 (2020).

- M. Quintana, E. Oblak, **J.M. Marín Ramírez** and A. Berger. *Experimental exploration of the vector nature of the dynamic order parameter near dynamic magnetic phase transitions.* Phys. Rev. B **102**, 94436 (2020).

- M.A. Arroyave, **J.M. Marín Ramírez**, G.E. Campillo, J.H. López, O. Arnache and J. Osorio. *A Kerr magnetometer setup in the kHz regime based on open-hardware architecture.* J. Phys.: Conf. Ser. **1247** 012047.

Other publications:

- D. R. Ratkovski, **J. M. Marín Ramírez**, E. L. T. França, Adolfo Franco Jr, F .L. A. Machado. *On the Correlation of the Magnetic Properties with the Structural Parameters in Fe-doped Europium Chromite.* Accepted for publication AIP Magnetism and Magnetic Materials (02-12-2020).

- D. R. Ratkovski, **J. M. Marín Ramírez**, P. R. T. Ribeiro, H. V. S. Pessoni, A. Franco, and F. L. A. Machado. *Magnetic irreversibility and spin dynamics in nanoparticles of iron-doped europium chromite.* J. Alloys Compd. **724**, (2017).

- G.E. Campillo, A.I. Figueroa, O. Arnache, J. Osorio, **J.M. Marín Ramírez** and L,

Fallarino. *A brief discussion of the magnetocaloric effect in thin films of manganite doped with chromium.* J. Phys.: Conf. Ser. **1247** 012013.

- J.D. López, J.P. Cuenca, **J.M. Marín Ramírez**, O. Arnache and H. Riascos. *Graphite Thin Films Production by Laser Ablation.* Scientia et Technica Año XXIII, Vol. 23, No. 04, diciembre de 2018.

- **J.M. Marín Ramírez**, L.A. Cáceres Díaz, Y.Rojas Martínez, J.A. Osorio, M. H. Medina Barreto and B. Cruz Muñoz. *Diseño y construcción de un contador proporcional de flujo de gas con aplicación en espectroscopia Mössbauer.* Scientia et Technica Año XXIII, Vol. 23, No. 03, septiembre de 2018.

Acknowledgments

"If you remember me, then I don't care if everyone else forgets..."

Haruki Murakami

It is hard to put into words and to account for all the people that made possible this thesis or the ones who I have share with a coffee that made my day lighter, but I'll try my best.

First, I would like to thank professor Oscar Arnache who gave me the opportunity to work at the Solid State group at the Universidad de Antioquia, whom has been always ready to offer me his guidance not only academical but more importantly personal. Likewise, my co-advisor Gloria Campillo, and the non-official one Jaime Osorio, for their time and input into all the aspects that involved my time at the Ph.D. program.

This work would not be possible without my time at the nanomagnetism group at the CIC nanoGUNE (San Sebastian, Spain). Even though, this period of time was a challenging one, I will always appreciate all the **Physics** and work ethic learned from Dr. Andreas Berger, who encourage me and pushed me to become a better researcher. Similarly, I would like to thank Patricia, Eva, César, Mikel and Paolo Vavasori, top notch researchers and above all really nice people.

To the reviewers' Gloria Buendia, Juan Gabriel Ramírez and Germán Pérez Alcázar, for taking their time to read and comment thoroughly this thesis. Their suggestions did in fact improve the scientific quality of our final work.

I never though that my Ph.D. process would allow me to know so much about myself, but above all to find new people who I am glad to call my friends: Manuel, Wilmer and Alba, Diego, Tatiana, Alexa, Mario, Robinson and Nacho; so thank you for the coffees, beers, walks, trips and the nice words when things seem more complicated or even dull.

To my best friends the soon to be (or already) doctors Jey, Anderson, John, Felipe and Eduard. Even though, we all have to move away to do some science and follow our different paths, there is nothing like a good chat, some music, laughs and beer with them.

To my mom **Ruby** and my uncle/father **Nacho**, because without their teachings, efforts and sacrifices, I would not be the person that I am today. My sisters *Mary* and *Luisa* for their support and company, and my nephews Sebas and Samuel for the laughs. My cousins in Spain, Ana, Asier, Rosa and Octavio, for making me feel always at home.

Only one person can understand the highs and lows of the last four years, I am sorry to be such a burden sometimes but I am really glad to have you by my side, I love you *Joha*. Thanks for our Friday nights but above all our Monday mornings, and for having always believe in me more than I do; let's hope that plenty of new and exciting things may come in our way!

Lastly, this work would not be possible without the financial support from Colciencias, Universidad de Antioquia, Grupo de Estado Sólido and CIC nanoGUNE. Likewise, a big thank you to everyone at the Physics institute, with their respective technicians, secretaries and general staff for their assistance throughout this work.

¡Eskerrik asko!

Appendix A

An open hardware and software based Magneto-optical Kerr effect set-up

Even though MOKE instrumentation for the characterization of low dimensional magnetic systems has been widely used [166–168]. In this appendix, we developed a singular approach to build a L-MOKE[1], based on the use of modular architecture, i.e. open hardware instrumentation and open software data acquisition. Our low cost L-MOKE, have built-in capabilities to be implemented in two different detection schemes, differential [169] and single detection. Thus, leading to a significant increase in the acquisition time and resolution, without compromising the quality of the measurements and the overall cost of the system.

A.1 Experimental set-up

A linearly polarized, low noise (0.1% rms) and monochromatic (λ = 632.8 nm) He–Ne laser was used in the measurements. To improve the polarization state and stability of the incident beam, a Thorlabs LPVIS050 polarizer (**P1**) with $1:10^5$ extinction rate was placed between the laser and sample, thus defining the polarization axis $\vec{s}$ or $\vec{p}$. After the light source is carefully aligned in either $\vec{s}$ or $\vec{p}$ polarization through (**P1**), the beam is reflected by the sample which is placed in the center of a pair of Helmholtz coils. An analyzer (**A**) (equal to (**P1**)) is placed in the way of the reflected beam and its rotated until the so-called extinction. Then **A** is moved at a small angle away from it. The best signal-to-noise ratio was reached for 2° to 6° degrees. Behind the analyzer, magneto-optical signal is acquired by a FDS100 photodide (**Ph1**) from Thorlabs in photoresistive mode

[1] Longitudinal magneto-optical Kerr effect set-up

and converted in an op-amp OPA380 transimpedance amplifier. The signal acquisition is done by means of Waveshare High-Precision AD/DA (24 bits) Expansion Board for a **Raspberry Pi**, which controls the power input to the Helmholtz Coils through an L298N H-Bridge commutator and a voltage source system through a PWM signal, as depicted in Fig.A.1a. The control of the system was implemented using *C* for performance reasons and runs in the Raspberry Pi. The raw data is accessible via *ssh* using the Raspberry Pi as server. Finally the data is analyzed in python and plotted in *gnuplot*.

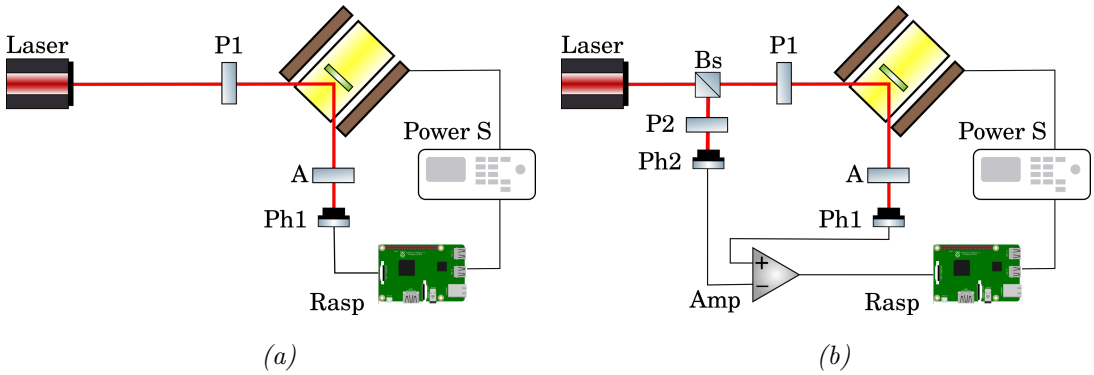

Figure A.1: (a) Kerr assemblies in conventional mode and (b) differential mode.

A small modification from the original setup was also put to test as seen in Fig.A.1b by modifying the detection scheme. Hence, between the laser source and **P1**, a beam splitter (**Bs**) was used to intersect and redirect the beam through a second polarizer (**P2**) with a similar photodetection arrange. This was done to get a reference signal which was subtracted with the one coming from **A** in a pre-amplified stage. Such scheme, enable a reduction in the electrical and source noise, which allowed an amplification gain of 25:1.

The magnetic response in $Fe_{1-x}C_x$ thin films was measured by taking single hysteresis loops in both configurations. Comparison between different acquisition time of the Kerr signal, are assessed by the fractional intensity change upon magnetization reversal $\Delta I/I$, and the signal to noise ratio (SNR). $\Delta I/I = 1/30$ was reached in the single mode L-MOKE setup, regardless of the different sampling rate. A comparison between data acquired using both L-MOKE detection schemes, conventional and differential is shown in Fig.A.2(a) and Fig.A.2(b) respectively.

Furthermore, signal to noise ratio exhibits a valuable difference when using both methods. Thus, when increasing the sampling rate from 100 SPS to 2.5 kSPS, SNR raises.

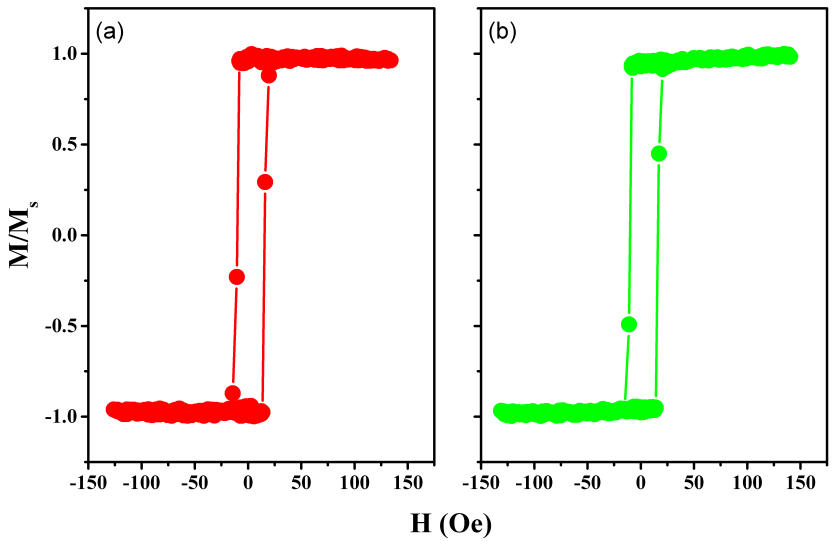

Figure A.2: Hysteresis cycles for a $Fe_{1-x}C_x$ thin film with $x = 0$ using two different detection schemes, (a) conventional and (b) differential. The cycles were averaged for 100 different loops taken at 2 seconds

Thereby, while the slow acquisition measurement has a signal fluctuation around 40%, fast resolved measurements are able to cut in half such variations; with a full range Kerr signal ΔI close to 200 mV. Additionally, the differential arrangement enhances the signal quality by eliminating the shot noise, and electric noise during the pre-amplification stage, yielding to a $\Delta I \approx 400$ mV. Nevertheless, the differential arrangement does not allow a Kerr angle computation, because the main signal reference has been subtracted, while in the single mode is easily obtained by approximations as seen in Fig. A.3(a).

Averaged coercive fields for the $Fe_{1-x}C_x$ thin films were obtained. In effect, H_c values reached by means of our L-MOKE are comparable to those coming from VSM characterization, as shown in Fig. A.3(b). The differences are explained because MOKE technique require smaller fields to magnetize the surface area where the spot is located, while the VSM measurements require a larger field to magnetize the entire volume of the sample.

In conclusion we were able to ensemble a low cost and high performance L-MOKE with two different detection schemes. Time-resolved amplification is crucial for the quality of the Kerr signal, enhancing the signal to noise ratio in comparison to longer measures. To achieve time-resolved magnetometry, a fast photoamplification is mandatory, and therefore, small, low capacitance photodiodes. Big photodiodes have big relaxation times and can leave to misleading coercive values. The use of open source enhances the velocity of

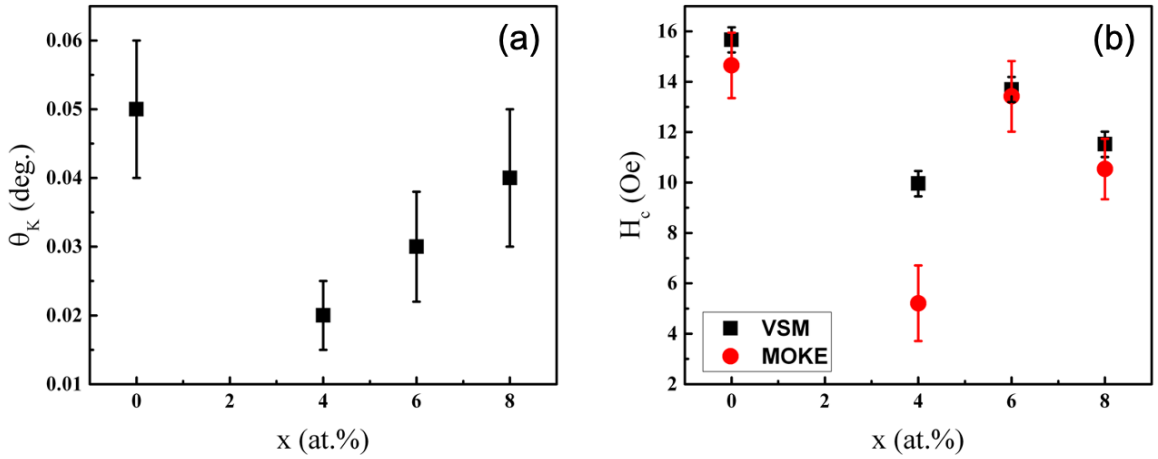

Figure A.3: (a) Kerr angle calculation for the different $Fe_{1-x}C_x$ ($0 \leq x \leq 0.08$) thin film samples and (b) coercive field values comparison for MOKE (black squares) and VSM (red circles).

the assembly and the research itself, allowing versatile instrumentation, and furthermore makes a better cost effective tool. More details of this work are presented in reference [170].

Appendix B

$Co_{1-x}Ru_x$ thin films Curie temperature analytical determination

Curie temperature (T_c) is the critical temperature at which a magnetic systems undergoes a thermodynamic phase transition. Therefore the magnetization (order parameter) changes from a ferromagnetic ($M > 0$) to a paramagnetic phase ($M \approx 0$).

$Co_{1-x}Ru_x$ thin films from $0 \leq 0.30$ are ferromagnetic at room temperature and are characterized by high T_c values (above 350 K). Experimentally, there are a few limitations to reach high temperature values to determine accurately T_c. This is because, when changing T the thin films could go through an actual structural phase transition, leading to wrongful data determination.

Therefore, as the Curie temperature in our thin film samples has values above our measurement range (350 K), analytical determination of T_c comes in handy to get approximate values for T/Tc to understand the effects of temperature on dynamic phase transitions.

Equation B.1 shows the analytical expression proposed by Kuz'min for the behavior of the $M(T)$ curve [160]. This model was proposed to determine the shape of $M(T)$ rather than the scale of temperature dependence of spontaneous magnetization.

$$M(T) = M_s(0)\left[1 - s\left(\frac{T}{T_c}\right)^{\frac{3}{2}} - (1-s)\left(\frac{T}{T_c}\right)^{p}\right]^{\frac{1}{3}} \tag{B.1}$$

From B.1, we have that $M_s(0)$ is the spontaneous magnetization, while s and p are fitting parameters. s defines the overall shape of the curve and has values $s > 0$, while $p = \frac{5}{2}$ for ferromagnetic systems as in our case. Furthermore, we have that this equation obeys Bloch's 3/2 power law at low temperatures, where $M(T)/M_s(0) \approx 1 - \frac{1}{3}s\frac{T}{T_c}^{1/3}$ as

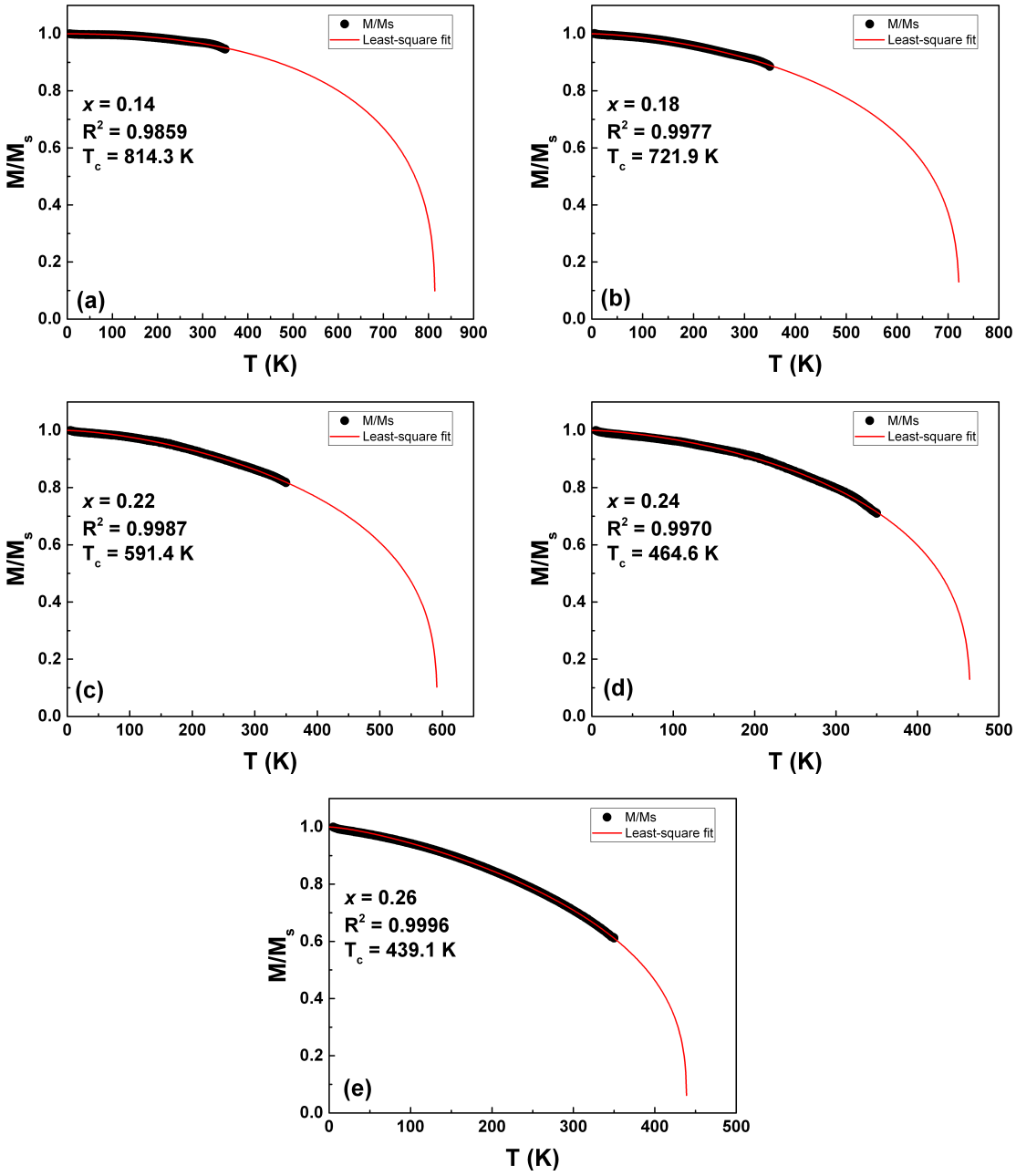

Figure B.1: Reduced magnetization ($M/M_s(0)$) as function of temperature for the $Co_{1-x}Ru_x$ ferromagnetic thin films with (a) $x = 0.14$, (b) $x = 0.18$, (c) $x = 0.22$, (d) $x = 0.24$ and (e) $x = 0.26$. The measured data (black dots) was fitted using the Kuz'min model for $M(T)$ (red line). The extrapolated T_c values are shown in each graphic with their corresponding R^2.

$\frac{T}{T_c} \to 0$, whereas in the critical region, $\frac{T}{T_c} \to 1$, $M(T)/M_s(0)$ is proportional to $(1 - \frac{T}{T_c})^{1/3}$, as prompted by the critical behavior of the Heisenberg model.

As a consequence we have used the model proposed by Kuz'min to determine analytically the T_c values for $Co_{1-x}Ru_x$ thin films with $x = 0.14, 0.18, 0.22, 0.24$ and 0.26. Fig. B.1 shows the corresponding least-square fits (red line) as function of the measured data

(black squares). In general, R^2 is above 0.97 which denotes a good relation between our data and the model.

Furthermore, the fitting parameters with their corresponding deviation values are shown in Table B.1. As expected when our limited data (up to 350 K) is far from T_c the error has greater values, but as the critical temperature gets closer to the measurement regime there is a noticeable diminution and the analytical function gets more accurate as inferred from the R^2 values. p was kept fixed to 5/2 as suggested in reference [160] and s is within the expected values for the model for the shape parameter.

x/**parameters**	T_c	ΔT	s	Δs	p	R^2
0.14	814.3	33.7	0.1240	0.0540	2.5	0.9859
0.18	721.9	21.1	0.7604	0.0197	2.5	0.9977
0.22	591.4	10.1	0.9768	0.0232	2.5	0.9986
0.24	464.6	1.7	0.8818	0.0162	2.5	0.9970
0.26	439.1	1.2	1.756	0.055	2.5	0.9996

Table B.1: Fitting parameters from the least square fit using Eq. B.1 for $M(T)$

Bibliography

[1] M. Keskin and M. Ertaş, Physica A: Statistical Mechanics and its Applications **496**, 79 (2018).

[2] J. O. Dabiri, Phys. Rev. Fluids **4**, 110501 (2019).

[3] R. Shojaei, P. Manshour, and A. Montakhab, Phys. Rev. E **100**, 022303 (2019).

[4] B. Slavko, K. Glavatskiy, and M. Prokopenko, Phys. Rev. E **99**, 042143 (2019).

[5] Y. Benhouria, I. Bouziani, I. Essaoudi, A. Ainane, and R. Ahuja, Journal of Magnetism and Magnetic Materials **460**, 223 (2018).

[6] P. Jurcevic, H. Shen, P. Hauke, C. Maier, T. Brydges, C. Hempel, B. P. Lanyon, M. Heyl, R. Blatt, and C. F. Roos, Phys. Rev. Lett. **119**, 080501 (2017).

[7] P. Riego, P. Vavassori, and A. Berger, Physica B: Condensed Matter **549**, 13 (2018).

[8] J. M. Yeomans, *Statistical mechanics of phase transitions* (Clarendon Press, 1992).

[9] E. Ising, Zeitschrift für Physik **31**, 253 (1925).

[10] C. N. Yang, Physical Review **85**, 808 (1952).

[11] L. Onsager, Phys. Re **1931**, 38 (1931).

[12] S. G. Brush, Reviews of Modern Physics **39**, 883 (1967).

[13] M. E. Fisher and M. N. Barber, Physical Review Letters **28**, 1516 (1972).

[14] M. E. Fisher, American Journal of Physics **32**, 343 (1964).

[15] G. Joyce, Physical Review **155**, 478 (1967).

[16] S. Katsura, Physical Review **127**, 1508 (1962).

[17] H. M. Babujian, Nuclear Physics B **215**, 317 (1983).

[18] S. H. Shenker and J. Tobochnik, Physical Review B **22**, 4462 (1980).

[19] R. J. Glauber, J. Math. Phys. **4**, 294 (1963).

[20] A. Berger, O. Idigoras, and P. Vavassori, Physical Review Letters **111**, 1 (2013).

[21] H. Yahata and M. Suzuki, Journal of the Physical Society of Japan **27**, 1421 (1969).

[22] K. Binder and H. Müller-Krumbhaar, Phys. Rev. B **9**, 2328 (1974).

[23] T. Tomé and M. J. De Oliveira, Physical Review A **41**, 4251 (1990).

[24] R. A. Gallardo, O. Idigoras, P. Landeros, and A. Berger, Phys. Rev. E - Stat. Nonlinear, Soft Matter Phys. **86**, 1 (2012).

[25] P. Riego and A. Berger, Physical Review E **91**, 062141 (2015).

[26] O. Idigoras, P. Vavassori, and A. Berger, Physica B: Condensed Matter **407**, 1377 (2012).

[27] Y. Yüksel, Physical Review E **91**, 032149 (2015).

[28] B. Aktaş, E. Vatansever, and H. Polat, Physica A: Statistical Mechanics and its Applications **447**, 379 (2016), arXiv:1501.06442v1 .

[29] G. M. Buendía and P. A. Rikvold, Physical Review E **78**, 051108 (2008).

[30] G. M. Buendía and P. A. Rikvold, Physical Review B **96**, 134306 (2017).

[31] X. Shi and P. Liu, Physica A: Statistical Mechanics and its Applications **536**, 120998 (2019).

[32] B. O. Aktaş, Ü. Akıncı, and H. Polat, Thin Solid Films **562**, 680 (2014).

[33] Q. Jiang, H.-N. Yang, and G.-C. Wang, Physical Review B **52**, 14911 (1995).

[34] D. T. Robb, Y. H. Xu, O. Hellwig, J. McCord, A. Berger, M. A. Novotny, and P. A. Rikvold, Physical Review B **78**, 134422 (2008).

[35] M. Straub, R. Vollmer, and J. Kirschner, Physical Review Letters **77**, 743 (1996).

[36] Z. Qiu and S. Bader, Journal of Magnetism and Magnetic Materials **200**, 664 (1999).

[37] P. Riego, P. Vavassori, and A. Berger, Physical Review Letters **118**, 117202 (2017).

[38] O. Idigoras, A. K. Suszka, P. Vavassori, P. Landeros, J. M. Porro, and A. Berger, Physical Review B - Condensed Matter and Materials Physics **84**, 2 (2011).

[39] O. Idigoras, U. Palomares, A. K. Suszka, L. Fallarino, and A. Berger, Applied Physics Letters **103**, 102410 (2013).

[40] J. Crangle and D. Parsons, Proceedings of the Royal Society of London. Series A. Mathematical and Physical Sciences **255**, 509 (1960).

[41] J. M. Coey, *Magnetism and magnetic materials* (Cambridge university press, 2010).

[42] B. D. Cullity and C. D. Graham, *Introduction to magnetic materials* (John Wiley & Sons, 2011).

[43] J. D. Jackson, *Classical electrodynamics* (American Association of Physics Teachers, 1999).

[44] D. J. Griffiths, *Introduction to electrodynamics* (American Association of Physics Teachers, 2005).

[45] S. Blundell, *Magnetism in condensed matter* (American Association of Physics Teachers, 2003).

[46] A. P. Guimarães and A. P. Guimaraes, *Principles of nanomagnetism*, Vol. 7 (Springer, 2009).

[47] C. Kittel, P. McEuen, and P. McEuen, *Introduction to solid state physics*, Vol. 8 (Wiley New York, 1996).

[48] R. M. White, R. M. White, and B. Bayne, *Quantum theory of magnetism*, Vol. 1 (Springer, 1983).

[49] A. P. Guimarães, *Magnetism and magnetic resonance in solids* (Wiley, 1998).

[50] W. D. Callister Jr and D. G. Rethwisch, *Fundamentals of materials science and engineering: an integrated approach* (John Wiley & Sons, 2012).

[51] P. Hofmann, *Solid state physics: an introduction* (John Wiley & Sons, 2015).

[52] S. M. Rezende, *Materiais e dispositivos eletrônicos* (Editora Livraria da Física, 2004).

[53] A. Aharoni *et al.*, *Introduction to the Theory of Ferromagnetism*, Vol. 109 (Clarendon Press, 2000).

[54] H. E. Stanley and V. K. Wong, American Journal of Physics **40**, 927 (1972).

[55] S. Chikazumi and C. D. Graham, *Physics of Ferromagnetism 2e*, 94 (Oxford University Press on Demand, 2009).

[56] T. Kaneyoshi, Journal of magnetism and magnetic materials **321**, 3430 (2009).

[57] E. C. Stoner and E. P. Wohlfarth, Philosophical Transactions of the Royal Society of London. Series A, Mathematical and Physical Sciences **240**, 599 (1948).

[58] W. K. Tse and A. H. MacDonald, Physical Review Letters **105**, 1 (2010).

[59] P. N. Argyres, Physical Review **97**, 334 (1955).

[60] T. Haider, International Journal of Electromagnetics and Applications **7**, 17 (2017).

[61] K. Shinagawa, Magneto-Optics , 137 (2000).

[62] P. Lissberger and M. Parker, Journal of Applied Physics **42**, 1708 (1971).

[63] B. Esmaeilzadeh, M. Moradi, and F. Jahantigh, Journal of Magnetism and Magnetic Materials **460**, 207 (2018).

[64] G. Guo and H. Ebert, Physical Review B **50**, 10377 (1994).

[65] A. Arora, S. Ghosh, and V. Sugunakar, Review of Scientific Instruments **82**, 10.1063/1.3669782 (2011).

[66] E. D. Palik and B. W. Henvis, Appl. Opt. **6**, 603 (1967).

[67] E. Moog and S. Bader, Superlattices and microstructures **1**, 543 (1985).

[68] E. Beaurepaire, J.-C. Merle, A. Daunois, and J.-Y. Bigot, Physical review letters **76**, 4250 (1996).

[69] K. D. Lee, J.-W. Kim, J.-W. Jeong, D.-H. Kim, S.-C. Shin, K.-H. Hong, Y.-S. Lee, C. H. Nam, M. H. Son, and S. W. Hwang, Journal of the Korean Physical Society **49**, 2402 (2006).

[70] V. Belotelov, D. Bykov, L. Doskolovich, A. Kalish, and A. Zvezdin, JOSA B **26**, 1594 (2009).

[71] A. López-Ortega, M. Zapata-Herrera, N. Maccaferri, M. Pancaldi, M. Garcia, A. Chuvilin, and P. Vavassori, Light: Science & Applications **9**, 1 (2020).

[72] H. Yu, J. Xiao, and P. Pirro, Journal of Magnetism and Magnetic Materials **450**, 1 (2018).

[73] A. López-Ortega, M. Z. Herrera, N. Maccaferri, M. Pancaldi, M. Garcia, A. Chuvilin, and P. Vavassori, arXiv preprint arXiv:1903.08392 (2019).

[74] P. Riego, S. Tomita, K. Murakami, T. Kodama, N. Hosoito, H. Yanagi, and A. Berger, Journal of Physics D: Applied Physics **50**, 19LT01 (2017).

[75] F. Wang, Z. Xiong, D. Wu, J. Shi, and Z. V. Vardeny, Synthetic Metals **155**, 172 (2005).

[76] T. Wolfram, R. Dewames, W. F. Hall, and P. Palmberg, Surface Science **28**, 45 (1971).

[77] S. Sides, P. Rikvold, and M. Novotny, Physical Review E **59**, 2710 (1999).

[78] T. Yasui, H. Tutu, M. Yamamoto, and H. Fujisaka, Physical Review E **66**, 036123 (2002).

[79] K. Tauscher and M. Pleimling, Physical Review E **89**, 022121 (2014).

[80] M. Suzuki and R. Kubo, Dynamics of the Ising model near the critical point. I (1968).

[81] E. Stoll, K. Binder, and T. Schneider, Physical Review B **8**, 3266 (1973).

[82] H. Jang, M. J. Grimson, and T. B. Woolf, Physical Review E **70**, 047101 (2004).

[83] M. F. Zimmer, Physical Review E **47**, 3950 (1993).

[84] G. Korniss, C. J. White, P. A. Rikvold, and M. A. Novotny, Physical Review E - Statistical, Nonlinear, and Soft Matter Physics **63**, 1 (2001), 0008155 [cond-mat] .

[85] B. K. Chakrabarti and M. Acharyya, Reviews of Modern Physics **71**, 847 (1999), 9811086 [cond-mat] .

[86] Y.-L. He and G.-C. Wang, Physical Review Letters **70**, 2336 (1993).

[87] H. Jang and M. J. Grimson, Physical Review E - Statistical, Nonlinear, and Soft Matter Physics **63**, 1 (2001).

[88] M. Pleimling, Journal of Physics A: Mathematical and General **37**, R79 (2004), 0402574 [arXiv:cond-mat] .

[89] D. T. Robb, P. A. Rikvold, A. Berger, and M. A. Novotny, Physical Review E - Statistical, Nonlinear, and Soft Matter Physics **76**, 1 (2007).

[90] T. Yasui, H. Tutu, M. Yamamoto, and H. Fujisaka, Physical Review E **66**, 036123 (2002).

[91] H. Park and M. Pleimling, Physical Review Letters **109**, 175703 (2012).

[92] H. Fujisaka, H. Tutu, and P. A. Rikvold, Physical Review E - Statistical, Nonlinear and Soft Matter Physics **63**, 036109 (2000), 0009284 [cond-mat] .

[93] S. W. Sides, P. A. Rikvold, and M. A. Novotny, Phys. Rev. E **57**, 6512 (1998).

[94] M. Quintana, E. Oblak, J. M. Marín Ramírez, and A. Berger, Phys. Rev. B **102**, 94436 (2020).

[95] J. A. Arregi, J. B. Gonzalez-Diaz, E. Bergaretxe, O. Idigoras, T. Unsal, and A. Berger, J. Appl. Phys. **111**, 10.1063/1.4720471 (2012).

[96] A. Berger and M. R. Pufall, J. Appl. Phys. **85**, 4583 (1999).

[97] M. R. Pufall, C. L. Platt, and A. Berger, J. Appl. Phys. **85**, 4818 (1999).

[98] K. Wasa, M. Kitabatake, and H. Adachi, *Thin Film Materials Technology* (William Andrew Publishing, Norwich, NY, 2004).

[99] M. A. Green, Journal of Materials Science: Materials in Electronics **18**, 15 (2007).

[100] Y. Fu, H. Du, W. Huang, S. Zhang, and M. Hu, Sensors and Actuators A: Physical **112**, 395 (2004).

[101] L. W. Martin and A. M. Rappe, Nature Reviews Materials **2**, 1 (2016).

[102] T. Leydecker, M. Herder, E. Pavlica, G. Bratina, S. Hecht, E. Orgiu, and P. Samorì, Nature nanotechnology **11**, 769 (2016).

[103] F. Huang, M. T. Kief, G. J. Mankey, and R. F. Willis, Physical Review B **49**, 3962 (1994).

[104] N. Kaiser, Applied optics **41**, 3053 (2002).

[105] M. Ohring, *Materials science of thin films* (Elsevier, 2001).

[106] N. A. Spaldin, *Magnetic Materials: Fundamentals and Applications*, 2nd ed., edited by C. U. Press (2010) p. 290.

[107] C. Moreau-Luchaire, C. Moutafis, N. Reyren, J. Sampaio, C. Vaz, N. Van Horne, K. Bouzehouane, K. Garcia, C. Deranlot, P. Warnicke, *et al.*, Nature nanotechnology **11**, 444 (2016).

[108] M. Johnson, P. Bloemen, F. Den Broeder, and J. De Vries, Reports on Progress in Physics **59**, 1409 (1996).

[109] B. Dieny, V. S. Speriosu, S. S. Parkin, B. A. Gurney, D. R. Wilhoit, and D. Mauri, Physical Review B **43**, 1297 (1991).

[110] J. C. Slonczewski *et al.*, Journal of Magnetism and Magnetic Materials **159**, L1 (1996).

[111] M. N. Baibich, J. M. Broto, A. Fert, F. N. Van Dau, F. Petroff, P. Etienne, G. Creuzet, A. Friederich, and J. Chazelas, Phys. Rev. Lett. **61**, 2472 (1988).

[112] M.-D. Cubells-Beltrán, C. Reig, J. Madrenas, A. De Marcellis, J. Santos, S. Cardoso, and P. P. Freitas, Sensors **16**, 939 (2016).

[113] G. Bräuer, B. Szyszka, M. Vergöhl, and R. Bandorf, Vacuum **84**, 1354 (2010).

[114] W. Westwood, MRS Bulletin **13**, 46 (1988).

[115] P. Kelly and R. Arnell, Vacuum **56**, 159 (2000).

[116] H. Oechsner, Applied physics **8**, 185 (1975).

[117] A. Anders, Surface and Coatings Technology **257**, 308 (2014).

[118] S. Swann, Physics in technology **19**, 67 (1988).

[119] I. Safi, Surface and Coatings Technology **127**, 203 (2000).

[120] L. V. Azároff, R. Kaplow, N. Kato, R. J. Weiss, A. Wilson, and R. Young, *X-ray Diffraction*, Vol. 3 (McGraw-Hill New York, 1974).

[121] B. D. Cullity, *Elements of X-ray Diffraction* (Addison-Wesley Publishing, 1956).

[122] M. Eckert, Acta Crystallographica Section A: Foundations of Crystallography **68**, 30 (2012).

[123] D. Ingerle, M. Schiebl, C. Streli, and P. Wobrauschek, Review of Scientific Instruments **85**, 083110 (2014).

[124] K. N. Stoev and K. Sakurai, Spectrochimica Acta Part B: Atomic Spectroscopy **54**, 41 (1999).

[125] M. Birkholz, *Thin film analysis by X-ray scattering* (John Wiley & Sons, 2006).

[126] M. Buchner, K. Höfler, B. Henne, V. Ney, and A. Ney, Journal of Applied Physics **124**, 161101 (2018).

[127] S. Foner, IEEE Transactions on Magnetics **17**, 3358 (1981).

[128] S. Foner, The review of scientific instruments **30**, 548 (1959).

[129] A. Zieba and S. Foner, Review of Scientific Instruments **53**, 1344 (1982).

[130] W. Burgei, M. Pechan, and H. Jaeger, Am. J. Phys. **71**, 825 (2003).

[131] S. Hoon, European Journal of Physics **4**, 61 (1983).

[132] T. El-Alaily, M. El-Nimr, S. Saafan, M. Kamel, T. Meaz, and S. Assar, Journal of Magnetism and Magnetic Materials **386**, 25 (2015).

[133] L. D. Landau, J. Bell, M. Kearsley, L. Pitaevskii, E. Lifshitz, and J. Sykes, *Electrodynamics of continuous media*, Vol. 8 (elsevier, 2013).

[134] A. K. Zvezdin and V. A. Kotov, *Modern magnetooptics and magnetooptical materials* (CRC Press, 1997).

[135] A. Berger and M. Pufall, Applied physics letters **71**, 965 (1997).

[136] E. Hecht, *Optics, 5e* (Pearson Education International, 2002).

[137] G. R. Fowles, *Introduction to modern optics* (Courier Corporation, 1989).

[138] J. A. Arregi, P. Riego, and A. Berger, Journal of Physics D: Applied Physics **50**, 03LT01 (2016).

[139] P. Vavassori, Applied Physics Letters **77**, 1605 (2000).

[140] V. Belotelov and A. Zvezdin, Physical Review B **86**, 155133 (2012).

[141] Y. Souche, A. P. B. Tufaile, C. Santi, V. Novosad, and A. Santos, Journal of magnetism and magnetic materials **226**, 1686 (2001).

[142] J.-W. Lee, J.-R. Jeong, D.-H. Kim, J. Ahn, J. Kim, and S.-C. Shin, Review of Scientific Instruments **71**, 3801 (2000).

[143] E. Oblak, P. Riego, L. Fallarino, A. Martínez-de Guerenu, F. Arizti, and A. Berger, Journal of Physics D: Applied Physics **50**, 23LT01 (2017).

[144] E. Oblak, P. Riego, A. Garcia-Manso, A. M. de Guereñu, F. Arizti, I. Artetxe, and A. Berger, Journal of Physics D: Applied Physics (2020).

[145] M. Acharyya, Physical Review E **59**, 218 (1999).

[146] S. Akkaya Deviren and E. Albayrak, Physical Review E **82**, 022104 (2010).

[147] B. Deviren, E. Kantar, and M. Keskin, Journal of Magnetism and Magnetic Materials **324**, 2163 (2012).

[148] R. Masrour, A. Jabar, A. Benyoussef, and M. Hamedoun, Journal of Magnetism and Magnetic Materials **403**, 167 (2016).

[149] J. Brandenburg, R. Hühne, L. Schultz, and V. Neu, Physical Review B **79**, 054429 (2009).

[150] C. Chang and M. H. Kryder, Journal of Applied Physics **75**, 6864 (1994).

[151] O. Thomas, Q. Shen, P. Schieffer, N. Tournerie, and B. Lépine, Physical Review Letters **90**, 017205 (2003).

[152] O. Idigoras, A. K. Suszka, P. Vavassori, B. Obry, B. Hillebrands, P. Landeros, and A. Berger, Journal of Applied Physics **115**, 10.1063/1.4867001 (2014).

[153] V. Shukla, C. Mukherjee, R. Chari, S. Rai, K. Bindra, and A. Banerjee, Journal of Magnetism and Magnetic Materials **370**, 100 (2014).

[154] R. M. Thantirige, J. John, N. R. Pradhan, K. R. Carter, and M. T. Tuominen, Journal of Magnetism and Magnetic Materials **407**, 273 (2016).

[155] P. Riego, Magneto-optical characterization of magnetic thin films and interface structures.

[156] L. Fallarino, Fabrication and characterization of magnetic thin films and multilayers.

[157] O. Idigoras, A. Suszka, P. Vavassori, B. Obry, B. Hillebrands, P. Landeros, and A. Berger, Journal of Applied Physics **115**, 083912 (2014).

[158] W. Yang, D. N. Lambeth, and D. E. Laughlin, Journal of Applied Physics **87**, 6884 (2000).

[159] C. Tannous and J. Gieraltowski, European journal of physics **29**, 475 (2008).

[160] M. D. Kuz'min, Physical Review Letters **94**, 107204 (2005).

[161] C. Eyrich, A. Zamani, W. Huttema, M. Arora, D. Harrison, F. Rashidi, D. Broun, B. Heinrich, O. Mryasov, M. Ahlberg, O. Karis, P. E. Jönsson, M. From, X. Zhu, and E. Girt, Physical Review B **90**, 235408 (2014).

[162] NI USB 4431 https://www.ni.com/sv-se/shop/select/sound-and-vibration-device?modelId=124858.

[163] S. H. Simon, *The Oxford solid state basics* (OUP Oxford, 2013).

[164] K. Ahnert and M. Mulansky, in *AIP Conference Proceedings*, Vol. 1389 (American Institute of Physics, 2011) pp. 1586–1589.

[165] Scipy https://docs.scipy.org/doc/scipy/reference/tutorial/integrate.html.

[166] V. Calle, C. Calle, O. Marín, E. Salazar, A. Cortés, W. Lopera, D. Arias, O. Guzmán, P. Prieto, A. Berger, *et al.*, Revista Colombiana de Fisica **38** (2006).

[167] J. I. Torres and B. Cruz, Tecnura **10** (2007).

[168] J. I. O. Gómez and A. M. C. Soto, Revista Politécnica **9**, 19 (2013).

[169] B. de Lima Bernardo, Applied Physics B **117**, 1099 (2014).

[170] M. Arroyave, J. M. Ramírez, G. Campillo, J. López, O. Arnache, and J. Osorio, Journal of Physics: Conference Series **1247**, 012047 (2019).